LUKAS GERSTER

TOWARDS SCALABILITY OF QUANTUM PROCESSORS

TOWARDS SCALABILITY OF QUANTUM PROCESSORS

LUKAS GERSTER

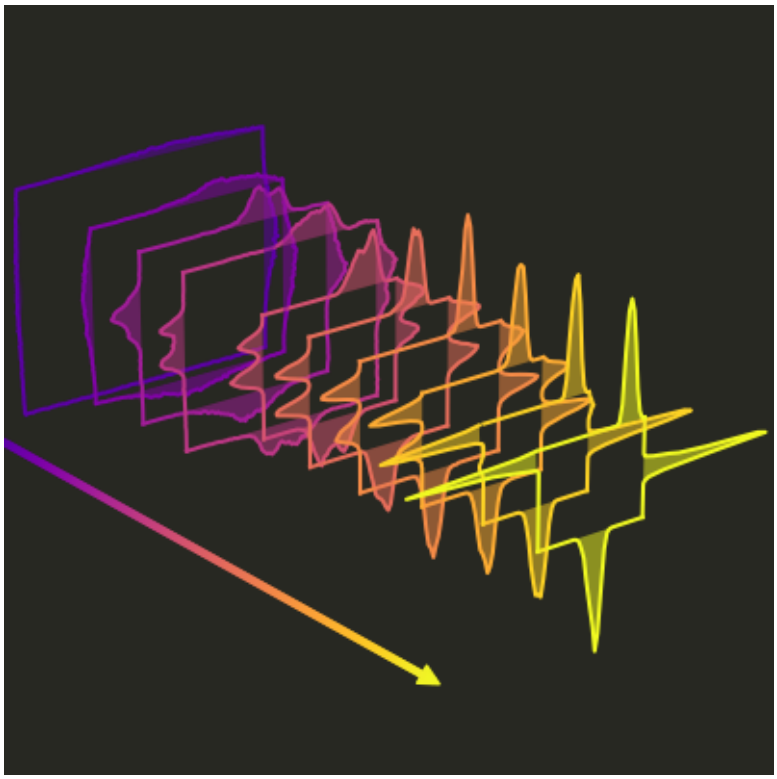

Thesis submitted to the

Fakultät für Mathematik, Informatik und Physik
of the
LEOPOLD-FRANZENS-UNIVERSITÄT INNSBRUCK

in partial fulfillment of the requirements for the degree of

DOCTOR OF PHILOSOPHY
(Physics)

Carried out under supervision of
o. Univ.-Prof. Dr. Rainer Blatt

in the Quantum Optics and Spectroscopy Group
at the Institut für Experimentalphysik
July 2024

Lukas Gerster
Towards Scalability of Quantum Processors,
© July 2024
LOCATION:
Innsbruck

ABSTRACT

Quantum information processing offers a more general concept to computing, which promises to be more efficient than classical computers. By encoding information in entangled quantum states, certain algorithms such as the factorization of integers promise an exponential speedup compared to the best known classical variants.

Trapped ions are one of the leading technologies in the highly active field of quantum information processing. They allow proof-of-principle demonstrations, but are still limited to operations on tens of qubits. Scaling these systems to a size where their computing power exceeds the capabilities of classical computers remains a very challenging task.

In the scope of this thesis a cryogenic ion trapping apparatus was modified and characterized with the goal of demonstrating building blocks of scalable quantum computing. This thesis presents three connected projects.

The first project concerns the experimental setup itself which houses a segmented surface trap capable of trapping $^{40}Ca^{+}$and $^{88}Sr^{+}$ions. We describe the apparatus and the modifications that were implemented along with the characterization measurements performed to evaluate its performance.

The setup was then used to develop and evaluate a novel calibration algorithm for entangling gates. The performance of quantum gate operations is experimentally determined by how accurately operational parameters can be determined and set, and how stable these parameters can be maintained. The developed calibration protocol can automatically estimate and adjust the experimental parameters of the widely used two-qubit Mølmer-Sørensen entangling gate operation in a trapped-ion quantum information processor. The protocol using Bayesian parameter estimation completes in less than one minute, with a residual median gate infidelity due to miscalibration that is smaller than the infidelity given by sources of decoherence.

Lastly, a novel gate scheme was used to demonstrate mixed-species entanglement, which can enable in-sequence readout without perturbing the entire register, a crucial ingredient for error correction. The same gate scheme can also be used for generating entanglement between qudits, a generalization of qubits. By using more levels of each ion more information can be encoded in the same number of particles, allowing to increase the size of the quantum computational Hilbert space.

ZUSAMMENFASSUNG

Der Quantencomputer verallgemeinert das Konzept der Informationsverarbeitung und verspricht dabei, effizienter als klassische Rechner zu sein. Hierbei wird Information in Quantenzuständen kodiert, was für gewisse Algorithmen wie die Primzahlfaktorisierung eine exponentielle Verbesserung der Laufzeit verspricht.

Eine der führende Technologien in diesem sehr aktiven Forschungsfeld der Quanteninformationsverarbeitung sind gespeicherte Ionen. Diese erlauben bereits die Demonstration aller notwendiger Bausteine eines Quantencomputers, aber solche Systeme sind immer noch limitiert auf Operationen mit einigen zehn Qubits. Eine zentrale Herausforderung bleibt der Bau von Quantencomputern mit einer ausreichenden Grösse, sodass ihre Rechnungsleistung die Fähigkeiten klassischer Maschinen übersteigt.

Im Rahmen dieser Dissertation wurde ein kryogener Ionenfallenaufbau modifiziert und charakterisiert mit dem Ziel, grundlegende Elemente für skalierbare Quanteninformationsverarbeitung zu demonstrieren. In dieser Arbeit werden drei verbundene Projekte präsentiert.

Das erste Projekt beschäftigt sich mit der Versuchsapparatur selbst, die eine segmentierte Oberflächenfalle beinhaltet die sowohl $^{40}Ca^{+}$wie auch $^{88}Sr^{+}$Ionen fangen kann. Diese Ionenfalle ist in einer Vakuumapparatur gekühlt von einem Kryostaten untergebracht. Wir dokumentieren den Apparat und die zugehörigen Laser und Kontrollsysteme mit den implementierten Modifikationen und präsentieren die Charakterisierungsmessungen die zur Evaluierung durchgeführt wurden.

Die Güte von Gatteroperationen ist abhängig davon wie genau die Betriebsparameter der Operation bestimmt werden können, und wie stabil diese gehalten werden können. Fehler in den Betriebsparametern können zu Gatterfehler führen. Deshalb wurde im Rahmen dieser Arbeit ein neuartiger Kalibrationsalgorithmus für verschränkende Gatter wurde entwickelt und evaluiert. Das Kalibrationsprotokoll kann automatisch die experimentellen Parameter des verschränkenden Mølmer-Sørensen Gatters bestimmen. Die Durchführung des Protokolls basierend auf Bayesscher Optimierung benötigt unter einer Minute, und resultiert mit einem kleineren medianen Gatterfehler durch Miskalibration als die Gatterfehler gegeben durch Dekoheränzquellen.

Im letzten Projekt dieser Dissertation wurde ein neuartiges Gatterschema verwendet um Verschränkung zwischen zwei verschiedenen Ionenspezies zu demonstrieren, was Zustandsdetektion während einer Sequenz ermöglichen kann, eine essenzielles Element für die Quan-

tenfehlerkorrektur. Das gleiche Schema kann verwendet werden um Quditverschränkung zu erzeugen. Die Verwendung mehrerer atomarer Energieniveaus pro Ion ermöglicht es mehr Information mit der gleichen Anzahl an Partikeln zu kodieren, was die verfügbare Grösse des Hilbertraums zur Speicherung von Information erhöht.

ACKNOWLEDGMENTS

Creating ions may work well in a vacuum, but writing a thesis does not. I had help from many sides during my PhD, and for that I would like to give my thanks.

Foremost I would like to thank Rainer Blatt for the opportunity to do my PhD in the marvelous Quantum Optics and Spectroscopy group. His passion for physics shaped the group, created a great working environment and I enjoyed being a part of this endeavor.

My experiment was part of the larger quantum information processing effort supervised by Philipp Schindler, Thomas Monz and Martin Ringbauer. Philipp taught me a great deal about physics and offered many insightful explanations and helpful comments to carry out my work. Tomi's hard work ensured that everyone stayed paid (including me), and also kept on pushing me to get my dissertation finished. Martin helped me with patient explanations and fruitful discussions.

I did my work in the "SQIP" lab, a name that stayed even though the homonymous grant ended by the time I joined the experiment. Here I had the pleasure of Martin van Mourik's company as partner-in-crime in the lab. It was a pleasure to work together, both during the frustration-inducing moments and our successes. Pavel Hrmo and Benjamin Wilhelm were also instrumental in the successes of our lab. Pavel, Ben, thank you for the time together, we made for a great team both in the lab and outside of it.

I would also like to thank Matthias Brandl who welcomed me way back at the beginning of my PhD and helped me to get started with understanding the lab and the experimental apparatus.

The two lunch groups I was part of, the Gurkengruppe and the sometimes competing salad group deserve a mention. It was always nice to indulge in culinary experiments of creative salad and Jause making and socialize together over the lunch breaks.

I would like to also give a thanks to the Blatt group as a whole. The working climate was always very pleasant, with people both being highly motivated and sharing their knowledge freely. There was always someone willing to help, someone able to take their time to go over and discuss the problem I encountered during the work.

The smooth running of the group owes a lot to the work of Patricia Moser and Renate Rupprechter, and I would like to thank them for their help and support with various administrative tasks and challenges.

On the technical side I could also rely on the support of Wolfgang Kuen and Kilian Prokop from the electronics workshop for repairs,

assistance and advice. I also want to offer many thanks to Armin Sailer, Christoph Wegscheider and Anton Schönherr from the mechanical workshop for their help, with a good part of the internal components of our vacuum system being manufactured by them.

Finally, I would like to thank my parents for their love, patience and support during the entirety of my studies. You have supported my interest of science for a long time now, and for that I am very grateful.

Thank you all very much.

CONTENTS

LIST OF FIGURES

LIST OF TABLES

LIST OF ALGORITHMS

LIST OF ABBREVIATIONS

AC	alternating current
AOM	acousto-optic modulator
COM	center-of-mass
DAC	digital-to-analog converter
DC	direct current
DDS	direct digital synthesis
ECDL	external cavity diode laser
EOM	electro-optic modulator
EMCCD	electron multiplying charge-coupled device
FPGA	field programmable gate array
GLP	Glan-Taylor laser polarizer
GUI	graphic user interface
LHe	liquid helium
LN	liquid nitrogen
NA	numerical aperture
NEG	non-evaporable getter
OOP	out-of-phase
PCB	printed circuit board
PBS	polarizing beam splitter
PD	photo diode
PDH	Pound-Drever-Hall
PEEK	polyether ether ketone
PID	proportional integral derivative
PMT	photo multiplier tube
RF	radio frequency
SPAM	state preparation and measurement
TTL	transistor–transistor logic
TA	tapered amplifier
Ti:Sa	titanium sapphire
TrICS	Trapped Ion Control Software
UHV	ultra-high vacuum
ULE	ultra low expansion glass
ZCT	zero-crossing temperature

1

INTRODUCTION

Many feats of human ingenuity not only rely on the inspiration to ask the right questions, but also require the capability to eventually compute an answer.

The capacity for performing computations has undergone an unprecedented transformation. Historically, the term computer was describing a job, which consisted of performing the required calculations by hand [1]. Mechanical aids were invented to aid with calculations or perform them, ranging from abacuses, slide rules over mechanical integrators [2] to the never-completed programmable Analytical Engine of Charles Babbage [3]. A breakthrough came with the advent of electronic computers, along with the invention of the transistor that heralded the information age [4]. While the first of these computers were large enough to a fill a room [5], as the technology matured the size of the devices drastically decreased. By the 1970s personal computers were possible that fit on a desk while nowadays a computer can be carried around in a pocket. This development was paired with an enormous rise in computing power, where a smartphone is now faster than a CRAY-2 supercomputer from 1985 at performing floating-point operations[1]. This has been an enormous boon for scientific and engineering applications, and made it economical to use computing power for private entertainment, enabling tasks such as the worldwide distribution of cat pictures.

Despite the technological advances for building computers, some problems however elude all these improvements in computational power, and remain intractable as their computational complexity fundamentally scales unfavorably with the size of the problem, requiring exponentially more resources as the size of the problem increases. A computer whose operations are instead described using the laws of quantum mechanics can solve some of these problems efficiently, making new classes of problems accessible to be calculated.

These range from the Deutsch algorithm [7], which first showed the possibility of a speedup over a classical algorithm, to problems of Database search [8], the factorization of integers [9]. These computational problems are joined by problems requiring simulation of quantum mechanics such as nitrogen and carbon dioxide fixation in

1 CRAY-2 1.45 GFlop/s [6], iPhone 13 mini 8.5 GFlop/s measured with Mobile Linpack.

quantum chemistry[10] or high-T_c superconductivity and quantum phase transitions in solid state systems[11].

Several quantum systems have been proposed to implement a quantum computer, among them photons[12, 13], cold atoms [14, 15], quantum dots[16, 17], and donors in solid state systems[18], the currently most mature platforms are provided by superconducting circuits[19, 20] and trapped ion systems[21, 22]. While these state-of-the-art systems have allowed building blocks of quantum computers to be demonstrated[23–25], solving problems of practical interest requires much larger machines than those currently available. However scaling up quantum computing computers remains a very challenging problem.

This thesis addresses some of the challenges for building a large scale quantum architecture based on trapped ions. The content of the thesis is structured in the following way:

CHAPTER 2 presents the core requirements for building a quantum processor and gives an overview of the fundamental building blocks of quantum information processing, two-level quantum systems called qubits, and the operations being performed on these qubits. We also introduce qudits, an extension of qubits where information is encoded in more than two levels per fundamental unit.

CHAPTER 3 illustrates the techniques utilized to implement quantum information processing in hardware. Here the focus lies specifically on a system of atomic $^{40}Ca^{+}$and $^{88}Sr^{+}$ions that are trapped using electromagnetic fields. We show how light can be used to couple to both the electronic and motional degrees of freedom of the system. We then describe how these interactions with laser light can be harnessed to prepare, manipulate and detect information encoded in this system.

CHAPTER 4 describes the experimental setup used during this work, including the vacuum system that houses the ion trap, the cryogenic cooling system being employed, the electronics used to control the apparatus as well as the various laser systems required to trap and manipulate the ions. It highlights the modifications made during the course of this thesis, and characterizations of the system performance are shown.

CHAPTER 5 focuses on the particular problem of calibrating quantum gates in such a trapped-ion system, and we discuss an automated routine we developed for estimating the control parameters of an entangling two-qubit gate based on Bayesian inference. We evaluate the performance of the algorithm, demonstrating that our method can find suitable parameter sets quickly and reliably.

CHAPTER 6 shows how the light shifts induced by a Raman interaction can be used for two different applications, for one to

entangle different atomic species, but also to implement gates in qudit systems with more than two logical levels per ion. We evaluate the states produced by the application of the gate and investigate their entanglement properties.

2

QUANTUM INFORMATION PROCESSING

"Nature isn't classical, dammit, and if you want to make a simulation of nature, you'd better make it quantum mechanical, and by golly it's a wonderful problem, because it doesn't look so easy."

— Richard P. Feynman [26]

This chapter gives an introduction to quantum information processing, where we explain how we can manipulate information that is encoded in a system governed by the laws of quantum mechanics. To this purpose we look at two-level quantum systems called *qubits* as the fundamental building blocks for storing information, and describe how logical operations can be performed on these qubits to perform calculations. Furthermore, we illustrate how the language of qubits can be extended to higher-dimensional systems.

When talking about a quantum computer we are looking for a system that is both programmable and controllable such that a variety of different algorithms can be executed. Analogous to how a classical Turing machine can perform every possible classical algorithm[27], every sufficiently capable quantum machine has in principle the same computational power[28], and is a so called *universal quantum computer*. Building such a universal quantum computer is a significant challenge, and a variety of different physical systems have been proposed as candidates for implementation. While the possible platforms each have unique challenges and advantages, there is a common set of crucial capabilities called the *DiVincenzo criteria* any system must possess to realize an universal quantum computer[29]. These criteria are listed in the following:

1. *A scalable physical system with well characterized qubits:* The qubits are the physical basis in which the information is encoded. They are discussed in the following Sections 2.1 and 3.2, and the challenges to scaling them are elaborated in Section 3.6 but also influence the experimental setup described in Chapter 4.

2. *The ability to initialize the state of the qubits to a simple fiducial state:* The ability to prepare the system in a known initial state is essential and is discussed in Section 3.4.

3. *Long relevant decoherence times, much longer than the gate operation time:* The decoherence time describes the duration until a qubit looses the information encoded in it. This criterion demands that quantum information can be stored for the duration of the computation. The measurement of this quantity is discussed in Sections 3.5.2, 4.3 and 4.4.

4. *A universal set of quantum gates:* The gate operations allow the manipulation of the quantum information stored in the register to implement an algorithm of interest. The requirements on the availability of gates is described in Section 2.2, and their implementation is discussed in Section 3.5

5. *A qubit-specific measurement capability:* Once a computation has been performed, its results need to be read out. Sections 3.4.1 and 4.6 describe how the information can be extracted from a quantum state.

2.1 QUBITS

The qubits are the information carriers in a quantum computer analogous to the classical bits that encode the information in a classical computer. While a single bit can take on either the state of 0 or 1, the most general state of a single qubit is described by a superposition of the two basis states $|0\rangle$ and $|1\rangle$:

$$|\psi\rangle = \alpha\,|0\rangle + \beta\,|1\rangle\,, \tag{2.1}$$

where the two variables $\alpha, \beta \in \mathbb{C}$ are normalized by the condition $|\alpha|^2 + |\beta|^2 = 1$. The squared amplitude of these variables $|\alpha|^2, |\beta|^2$ corresponds to the probability to finding the system in state $|0\rangle$ or $|1\rangle$ respectively.

Alternatively the state can be described by two angles $\theta, \phi \in \mathbb{R}$

$$|\psi\rangle = \cos(\theta)\,|0\rangle + \sin(\theta)e^{i\phi}\,|1\rangle\,, \tag{2.2}$$

which fulfill the normalization condition for all θ, ϕ as $\cos(\theta)^2 + \sin(\theta)^2 = 1$. For a single qubit it is possible to graphically represent its state as a vector on a sphere, called the Bloch sphere where the angles θ, ϕ are interpreted as defining a point on the surface of the sphere. Fig. 2.1 depicts a state $|\psi\rangle$ on the Bloch sphere.

For an N-qubit state, the 2^N possible combinations of $|0\rangle$ and $|1\rangle$ states form a basis of a complex-valued vector space called the *Hilbert space*, and to represent an arbitrary state in this space Eq. (2.1) generalizes to

$$\begin{aligned} |\psi\rangle_N &= \sum_{i=0}^{2^N-1} \beta_i\,|(i)_2\rangle \\ &\text{with} \sum_i |\beta_i|^2 = 1, \end{aligned} \tag{2.3}$$

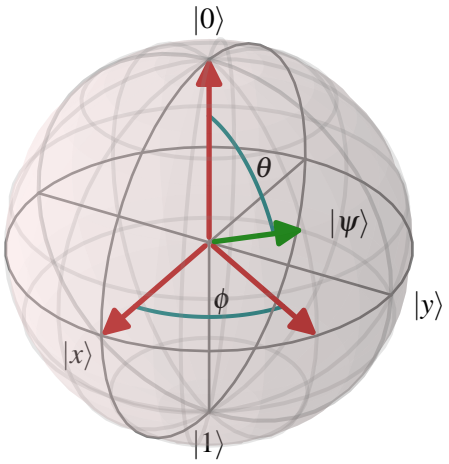

Figure 2.1: STATE OF A SINGLE QUBIT ON THE BLOCH SPHERE. The angles θ and ϕ parameterize the space for a pure state.

where $|(i)_2\rangle$ is the i-th basis state where the 0 and 1 state of the N qubits correspond to i represented as an N-digit binary number. The dimensionality of this space scales exponentially with the number N of qubits involved, and representing an arbitrary state requires an exponential number of factors β_i. This behavior makes it hard to simulate large quantum systems on classical machines, as in a general case an exponential amount of resources are required to store and manipulate these probability amplitudes.

2.1.1 *Entanglement*

For a composite system AB Eq. (2.3) can be rewritten as a product of basis states $\left|e_A^i\right\rangle, \left|e_B^j\right\rangle$ of the two subsystems.

$$|\psi_{AB}\rangle = \sum_{i=0}^{d_A-1} \sum_{j=0}^{d_B-1} A_{i,j} \left|e_A^i\right\rangle \otimes \left|e_B^j\right\rangle, \tag{2.4}$$

where d_A, d_B are the dimensions of the corresponding subsystem. Any state of such a composite system can be decomposed into a sum of orthonormal states $\left|\psi_A^i\right\rangle$ and $\left|\psi_B^i\right\rangle$ of the subsytems A and B respectively [30, 31] such that

$$|\psi_{AB}\rangle = \sum_i \lambda_i \left|\psi_A^i\right\rangle \otimes \left|\psi_B^i\right\rangle, \tag{2.5}$$

where the coefficents λ_i satisfy $\sum_i \lambda_i^2 = 1$. These are called the *Schmidt coefficients*. The minimal number of coefficients required to describe a state is called the *Schmidt number*, which corresponds to the rank of the matrix of coefficients

$$r(\psi) = \operatorname{rank}(A_{i,j}) \leq \min[d_A, d_B]. \tag{2.6}$$

This number is one way to quantify the amount of entanglement between the systems of A and B, with the state $|\psi\rangle$ being separable only if the Schmidt number is equal to 1[30]:

If the number is greater than 1, the subsystems are entangled and can exhibit non-classical correlations, with a famous example being the Bell states such as $|\psi\rangle = \frac{1}{\sqrt{2}}(|00\rangle + |11\rangle)$. This particular state is composed of a sum of two orthogonal states $|00\rangle, |11\rangle$ and thus has a Schmidt number of 2.

2.1.2 *Density Matrix Formalism*

The state description of Eq. (2.3) assumes perfect knowledge of the state; we call these states pure states. A physical system, however, is not always in such a pure state, as we can have imperfect knowledge of our state. This may arise whenever our system is not fully closed. For example noise can cause uncontrolled interactions with the environment that leads to a local loss of information, illustrated in Fig. 2.2 by a state vector slowly spiraling inwards. The state of this system can then still be described as a probabilistic ensemble of different pure states.

Such a probabilistic ensemble of $p_i, |\psi_i\rangle$ where p_i is the probability to be in state $|\psi_i\rangle$ can be formally written as[30]

$$\rho = \sum_i p_i \, |\psi_i\rangle\langle\psi_i| \, . \tag{2.7}$$

The Hermitian trace-1 matrix ρ is called the *density matrix*. For a pure states the density matrix will fulfill the condition of the purity $\mathrm{tr}(\rho^2) = 1$, otherwise for $1/d \leq \mathrm{tr}(\rho^2) < 1$ the state is mixed. For a pure state to become mixed indicates a loss of information, which can be described by the *partial trace*. This is an operator acting on the composite system consisting of subsystems A, B. The system described by the density matrix ρ_{AB} composed of basis states $|a_i\rangle, |b_j\rangle$, giving

$$\begin{aligned} \rho_A = \mathrm{Tr}_B(\rho_{AB}) &= \mathrm{Tr}_B \left(\sum_{i,j} p_{i,j} \, |a_i\rangle\langle a_i| \otimes |b_j\rangle\langle b_j| \right) \\ &= \sum_{i,j} p_{i,j} \, |a_i\rangle\langle a_i| \, \mathrm{Tr}(|b_j\rangle\langle b_j|). \end{aligned} \tag{2.8}$$

Its effect is to produce a density matrix describing only the subsystem of A, retaining no information of the system B.

To analyze a quantum state one would like to compare them to other states. A figure of merit that allows to do so is the fidelity, defined as the following [32]

$$F(\rho, \sigma) = (\mathrm{Tr}[\sqrt{\rho}\sigma\sqrt{\rho}])^2, \tag{2.9}$$

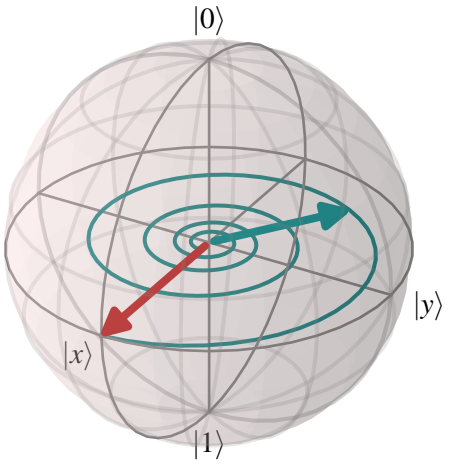

Figure 2.2: Trajectory of a single qubit rotating due to a σ_z interaction while being subjected to dephasing. This causes the state vector to continuously shrink as the state becomes progressively more mixed.

where ρ and σ are the density matrices of the two states being compared[1]. The fidelity is bounded $0 \leq F(\rho, \sigma) \leq 1$, with $F(\rho, \sigma) = 1$ only if $\rho = \sigma$. In the special case that the two density matrices describe pure states $|\psi\rangle, |\phi\rangle$, the fidelity in Eq. (2.9) becomes the transition probability between the two states [32]

$$F(|\psi\rangle\langle\psi|, |\phi\rangle\langle\phi|) = |\langle\phi|\psi\rangle|^2. \tag{2.10}$$

2.2 UNIVERSAL SET OF GATE OPERATIONS

To utilize a register of qubits to implement an algorithm, a sequence of gates is applied that manipulate the state. These can be expressed as operations U acting on the state vector $|\psi\rangle$ by $|\psi'\rangle = U|\psi\rangle$. For the normalization conditions of Eq. (2.3) for arbitrary $|\psi\rangle$ to be fulfilled, the matrix of the operation U has to be unitary, meaning it has to fulfill the condition $U^\dagger U = \mathbb{1}$ [30]. These operations are referred to as gate operations or gates in analogy to classical logic gates.

Directly implementing arbitrary N-qubit unitary operations $U^N \in \mathrm{SU}(2^N)$ is infeasible in practice, as we only have a limited set of interactions available that can be experimentally created and controlled. We thus rely on the decomposition of such an interaction into more elementary building blocks that are then applied to the qubits.

1 This definition by Jozsa [32] is the square of the other commonly used definition given in Nielsen and Chuang [30]. The choice has been made due to the agreement described in Eq. (2.10).

For a single qubit some of the most important gates are given by the Pauli operators

$$X = \begin{pmatrix} 0 & 1 \\ 1 & 0 \end{pmatrix}, Y = \begin{pmatrix} 0 & -i \\ i & 0 \end{pmatrix}, Z = \begin{pmatrix} 1 & 0 \\ 0 & -1 \end{pmatrix}. \tag{2.11}$$

Other commonly used gates to build a single-qubit gate set are the Hadamard, Phase- and the T-gate, described by the following matrices:

$$H = \frac{1}{\sqrt{2}} \begin{pmatrix} 1 & 1 \\ 1 & -1 \end{pmatrix}, P = \begin{pmatrix} 1 & 0 \\ 0 & i \end{pmatrix}, T = \begin{pmatrix} 1 & 0 \\ 0 & e^{i\pi/4} \end{pmatrix} \tag{2.12}$$

To implement an algorithm, additionally controlled two-qubit operations are required. The canonical example for a such a quantum gate is the controlled-NOT (CNOT) gate. It has two inputs, a control and a target qubit. If the control is set to $|0\rangle$ the target qubit is unaffected, but if the control is $|1\rangle$ the state of the target is flipped. Its action in matrix representation is given by

$$\text{CNOT} = \begin{pmatrix} 1 & 0 & 0 & 0 \\ 0 & 1 & 0 & 0 \\ 0 & 0 & 0 & 1 \\ 0 & 0 & 1 & 0 \end{pmatrix} \tag{2.13}$$

The CNOT gate is an entangling gate, which can be seen when applying it to a pair of qubits. Starting in the zero state if we first apply a Hadamard gate to the control qubit, the state becomes $|00\rangle \to (|00\rangle + |10\rangle)/\sqrt{2}$. The CNOT gate then transforms this to the entangled Bell state $(|00\rangle + |11\rangle)/\sqrt{2}$.

It can be shown [30, 33] that an arbitrary N-qubit operation $U^N \in \mathrm{SU}(2^N)$ can already be decomposed into a sequence of gates of single-qubit gates $U^1 \in \mathrm{SU}(2)$ and one type of entangling two-qubit gate $U^2 \in \mathrm{SU}(4)$. This still requires arbitrary $\mathrm{SU}(2)$ rotations, but following the Solovay-Kitaev theorem these can be efficiently approximated using only a finite set of single-qubit gates, requiring only $\mathcal{O} = \log^c(1/\epsilon)$ gates, where c is a constant[34].

Thus, it is sufficient instead of arbitrary unitaries to only implement a limited set of gates given by $\{X, Y, Z, H, P, T, \text{CNOT}\}$, consisting of the Hadamard, Phase-, T- and the CNOT-gate, along with the Pauli operations to perform possible quantum algorithms.

2.3 QUDITS

The physical systems in which one may implement a qubit are typically not true two-level systems. Instead they feature a multitude of states from which two are selected to represent the logical levels of a qubit, with the other states being ignored for the purpose of encoding

quantum information. Using more states per physical information carrier increases the size of the accessible Hilbert space for a computation for a given number of physical information carriers, suggesting a reduction in atoms required for performing an algorithm such as the quantum phase estimation algorithm[35, 36]. Error correcting codes for qudits further promise more favorable thresholds[37], and more efficient methods for magic state distillation[38], a highly resource intensive aspect of error correction. Simulations of spin systems with spins $> 1/2$ promise to be more efficient if directly implemented on a qudit system rather than mapping each simulated spin to a collection of qubits[39], but also qubit circuits may be compiled more efficiently with regards to the number of entangling gates required[40–42].

To perform algorithms on a qudit system, we would like to have a set of gates that can be applied to a register analogous to the qubit case.

While single-qubit operations can be described by SU(2), rotations on a single d-dimensional qudit are described by SU(d). For a qutrit the special unitary group SU(3) is spanned by the Gell-Mann matrices [43]

$$\lambda_1 = \begin{pmatrix} 0 & 1 & 0 \\ 1 & 0 & 0 \\ 0 & 0 & 0 \end{pmatrix} \lambda_2 = \begin{pmatrix} 0 & -i & 0 \\ i & 0 & 0 \\ 0 & 0 & 0 \end{pmatrix} \lambda_3 = \begin{pmatrix} 1 & 0 & 0 \\ 0 & -1 & 0 \\ 0 & 0 & 0 \end{pmatrix} \tag{2.14}$$

$$\lambda_4 = \begin{pmatrix} 0 & 0 & 1 \\ 0 & 0 & 0 \\ 1 & 0 & 0 \end{pmatrix} \lambda_5 = \begin{pmatrix} 0 & 0 & -i \\ 0 & 0 & 0 \\ i & 0 & 0 \end{pmatrix} \lambda_6 = \begin{pmatrix} 0 & 0 & 0 \\ 0 & 0 & 1 \\ 0 & 1 & 0 \end{pmatrix} \tag{2.15}$$

$$\lambda_7 = \begin{pmatrix} 0 & 0 & 0 \\ 0 & 0 & -i \\ 0 & i & 0 \end{pmatrix} \lambda_8 = \frac{1}{\sqrt{3}} \begin{pmatrix} 1 & 0 & 0 \\ 0 & 1 & 0 \\ 0 & 0 & -2 \end{pmatrix} \tag{2.16}$$

These matrices do form three independent SU(2) algebras consisting of $\{\lambda_1, \lambda_2, \lambda_3\}$, $\{\lambda_4, \lambda_5, (\lambda_3 + \sqrt{3}\lambda_8)/2\}$ and $\{\lambda_6, \lambda_7, (-\lambda_3 + \sqrt{3}\lambda_8)/2\}$, each corresponding to single qubit operations on a two-level subspace while leaving the third level unaffected. These subalgebras reflect the fact that single-qudit operations can be constructed by concatenating the two-level interactions used in the qubit case on different pairs of levels.

These operations can be generalized to arbitrary dimensions d, where the $SU(d)$ algebra is described by the $d^2 - 1$ generalized Gell-Mann matrices[44]. These are given by the collections of symmetric

matrices $\lambda^s_{j,k}$, anti-symmetric matrices $\lambda^a_{j,k}$ and diagonal ones λ_l, defined by:

$$\lambda^s_{j,k} = E_{k,j} + E_{j,k} \text{ for } 1 \leq j < k \leq d \tag{2.17}$$

$$\lambda^a_{j,k} = i(E_{k,j} - E_{j,k}) \text{ for } 1 \leq j < k \leq d \tag{2.18}$$

$$\lambda_l = \sqrt{\frac{2}{l(l+1)}} \left(\sum_{j=1}^{l} E_{j,j} - l E_{l+1,l+1} \right) \text{ for } 1 \leq l \leq d-1, \tag{2.19}$$

where $E_{k,j}$ is the matrix with 1 in the k,j-th entry and zero otherwise. Using at most $\mathcal{O}(d^2)$ two-level gates any single-qudit gate can be implemented[45].

2.3.1 *Qudit Entanglement*

As in the case of qubits, an entangling two-qudit gate is required to complete the toolbox for implementing universal qudit circuits. For qubits the choice of gate is of little consequence for compiling circuits, as any two fully entangling gates can be transformed into each other by local rotations. In the case of qudits the situation becomes more complex, with not all entangling operations being equal up to local rotations [46].

As a basic entangling gate we can consider the controlled exchange gate (CEX), which can be formed by embedding the CNOT gate in a higher dimensional space. Its action on a state $|jk\rangle$ is given by

$$CEX_{t_1,t_2} : \begin{cases} |jt_1\rangle \leftrightarrow |jt_2\rangle, & \text{if } j = d-1, k \in \{t_1, t_2\} \\ |jk\rangle \rightarrow |jk\rangle, & \text{if } j \neq d-1 \end{cases} \tag{2.20}$$

It swaps two states $|t_1\rangle, |t_2\rangle$ of the target qudit if and only if the control qudit is in the specific state $|d-1\rangle$.

This gate can be used to construct the controlled increment gate, that increments the state of the target qudit by 1 if and only the control qudit is in the specific state $|d-1\rangle$[45]:

$$CINC : \begin{cases} |jk\rangle \rightarrow |jk\rangle, & \text{if } j \neq d-1 \\ |jk\rangle \rightarrow |j(k \oplus 1)\rangle, & \text{if } j = d-1 \end{cases}, \tag{2.21}$$

where $\oplus$ denotes the addition modulo d. The $CINC$ gate can be composed of d applications of the CEX gate.

The SUM gate[47] in turn changes the state index of the second qudit depending on the state of the first qudit:

$$SUM : |jk\rangle \rightarrow |j(k \oplus j)\rangle \tag{2.22}$$

This gate is a generalization of the $CNOT$ gate, and can in turn be composed of d applications of the $CINC$ gate, which corresponds to a

total of d^2 CEX gates or embedded two-qubit gates. Thus a pattern emerges that while it is possible to decompose any qudit-gate into embedded two-qubit gates, doing so may incur a significant overhead in the number of gates utilized. As a consequence for a qudit-based quantum processor expanding the toolbox of available entangling gates will be beneficial, promising more efficient implementations of circuits by choosing the right type of gate for the specific task given.

3

TRAPPED ION QUANTUM COMPUTER

"It's still magic even if you know how it's done."

— Terry Pratchett, *A Hat Full of Sky*

To build a quantum computer, the desired capabilities specified by the DiVincenzo criteria for initializing, manipulating and reading out a quantum system must be implemented in hardware. Trapped ions are currently one of the most mature technological platforms, offering identical qubits with long coherence times, as well as high-fidelity gates and state detection [48–50]. They also offer the possibility of remote entanglement via photon generation [51, 52], and shared motional modes allow for full connectivity between qubits in the same potential well.

In the following, we will discuss the fundamental techniques to implement quantum operations on this system. First we explore the physics of Paul traps (Section 3.1) and discuss the properties of the atomic species used (Section 3.2). We will then review the techniques used to manipulate the ions (Sections 3.3 to 3.5).

3.1 PAUL TRAPS

Atoms are a perfect choice for implementing qubits, as they are identical quantum systems that can have long lived states in which quantum information can be encoded. However, to practically utilize atoms for storing information they need to be trapped and shielded from the environment. Studying charged atoms compared to neutral ones opens the possibility to use the interaction of their charge with electromagnetic fields to build a trap for the particles that spatially confines them. By placing the trap inside an ultra-high vacuum (UHV) environment collisions with other particles are minimized which can lead to loss of the ions.

The two most prominent trapping schemes used for confining charged particles are the Penning trap [53] and the Paul trap [54], where in this thesis the latter has been used. Its working principle is described in the following section.

3.1.1 *Pseudo-potential Approximation*

To successfully trap a particle, one needs to confine it in all three spatial dimensions. Generally speaking, to create confinement requires a restoring force that counteracts any disturbances a particle may experience. For a charged particle interacting with an electric field the force is the derivative of the electric potential, thus a trapping potential requires a potential minimum to generate such a restoring force. Such a minimum is characterized by a vanishing first derivative and a second derivative > 0. Generating a confining electric potential in free space may seem prohibited by Earnshaw's theorem, which directly follows from Gauss' law, one of the Maxwell equations. The condition of the Laplace equation on the electric potential in free space is given by

$$\nabla^2\Phi = \frac{\partial^2\Phi}{\partial x^2} + \frac{\partial^2\Phi}{\partial y^2} + \frac{\partial^2\Phi}{\partial z^2} = 0. \tag{3.1}$$

This equation directly shows that not all second derivatives of the electric potential Φ can have the same sign, and thus a confining potential in two dimensions will necessarily produce an anti-confining potential in the third direction. It follows that the static electric potential cannot have any minima in free space.

However it is possible to generate an effective potential, also named *pseudo-potential*, that has the desired minimum by the introduction of an oscillating radio frequency (RF) field. We can use a Taylor expansion to write out the lowest orders of the potential of a static and an oscillating field as

$$\begin{aligned} \Phi_{RF}(\vec{r},t) &= \frac{V_{RF}}{2|r_0|^2}\cos(\Omega_{RF}t)\Big(\sum_i \alpha_i r_i^2\Big) \\ \Phi_{DC}(\vec{r}) &= \frac{U_{DC}}{2|z_0|^2}\Big(\sum_i \beta_i r_i^2\Big) \end{aligned} \tag{3.2}$$

where Ω_{RF} is the frequency of the oscillating field, while V_{RF}, U_{DC} correspond to the RF and direct current (DC) voltages applied, and r_0, z_0 are characteristic distances that correspond to the distance from an electrode in a macroscopic bulk trap as depicted on the left in Fig. 3.1. To fulfill the Laplace equation Eq. (3.1) the coefficients α, β obey

$$\sum_i \alpha_i = \sum_i \beta_i = 0. \tag{3.3}$$

A single particle with charge Q subject to the potential $\Phi(\vec{r},t)$ experiences a force given by

$$\vec{F}(\vec{r},t) = -Q\nabla\Phi(\vec{r},t). \tag{3.4}$$

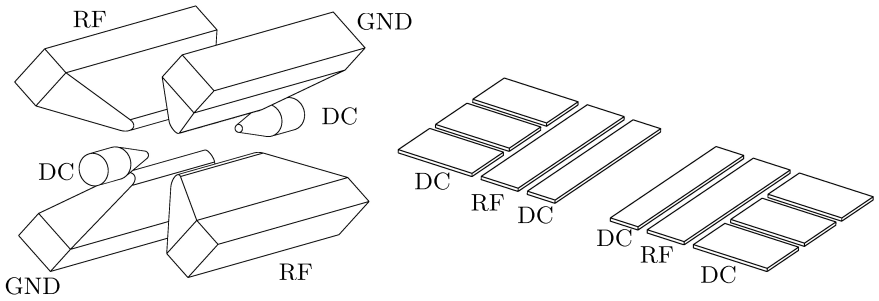

Figure 3.1: Electrode geometries for a bulk trap (left) and a surface trap (right).

We insert the potentials Eq. (3.2) into Eq. (3.4) to find a differential equation for the position of the particle, which we bring into the form of a Mathieu equation [55]

$$0 = \frac{\partial^2 \vec{r}}{\partial \xi^2} + (\vec{a} + 2\vec{q}\cos(2\xi))\vec{r}, \tag{3.5}$$

where we performed the following substitutions for the static and oscillating field:

$$\xi = \frac{\Omega_{RF} t}{2} \tag{3.6}$$

$$\vec{a} = \frac{8QU_{DC}}{mz_0^2\Omega_{RF}^2}\vec{\beta} \tag{3.7}$$

$$\vec{q} = \frac{4QV_{RF}}{mr_0^2\Omega_{RF}^2}\vec{\alpha} \tag{3.8}$$

For an ideal linear Paul trap we choose an RF potential in the x-y plane and no contribution in the z-axis, and a DC potential that is confining in z while being symmetric and anti-confining in x-y. These conditions lead to a choice of coefficients for the potentials (Eq. (3.2)) of

$$\begin{aligned} \alpha_x = -\alpha_y, \alpha_z = 0, \\ -\beta_x = -\beta_y = \frac{1}{2}\beta_z > 0 \end{aligned} \tag{3.9}$$

Stable solutions to the equations of motion (Eq. (3.5)) can be found for the parameter range of $0 < a < q < 1$, for which the motion of the charged particles is described by

$$\vec{r}(t) = \vec{A}\cos(\vec{\omega}t + \phi)(1 + \frac{\vec{q}}{2}\cos(\Omega_{RF}t)), \tag{3.10}$$

This periodic motion consists of two separate terms, the oscillations at the frequencies $\vec{\omega}$ are called the *secular motion*, while the oscillations at the drive frequency Ω_{RF} is called the *micro motion*. The secular motion is given by [55]

$$\vec{\omega} = \Omega_{RF}/2\sqrt{\vec{a} + \vec{q}^2/2}, \tag{3.11}$$

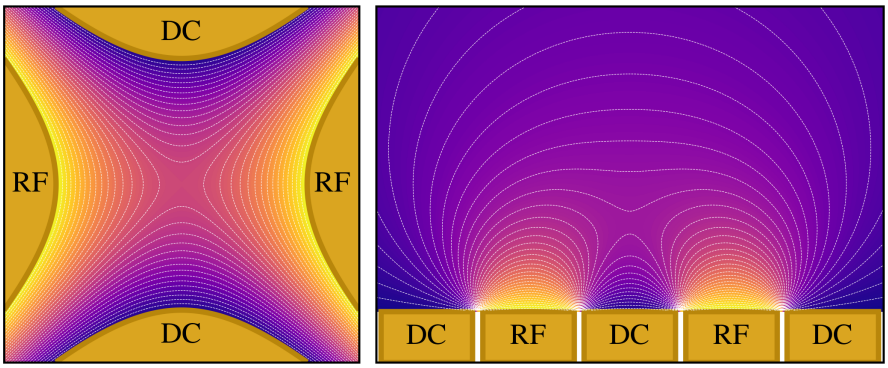

Figure 3.2: EQUIPOTENTIAL LINES OF THE RF FIELD FOR DIFFERENT TRAP GEOMETRIES IN THE XY-PLANE. On the left an ideal quadrupole trap geometry with two RF and two DC electrodes is shown, while on the right a surface trap geometry is depicted where all the electrodes have been moved into a plane.

which for the previous choice of coefficients results in the following frequencies:

$$\omega_z = \sqrt{2\frac{\beta_z Q U_{DC} \beta_z}{m z_0^2}}, \tag{3.12}$$

$$\omega_x = \omega_y = \sqrt{2\left(\frac{Q V_{RF} \alpha_{x,y}}{m r_0^2 \Omega_{RF}}\right)^2 - \frac{2\beta_z Q U_{DC} \beta_z}{2 m z_0^2}}. \tag{3.13}$$

Large micro motion amplitudes are generally an undesirable feature for quantum information processing [56, 57], and we thus try to minimize its effect by overlapping the trapping position with the *RF-null*, the axis along which the amplitude of the RF field is zero.

3.1.2 *Segmented Surface Traps*

The potential landscape described in the previous section can be generated by a set of two RF and two ground electrodes that generate the radial pseudo-potential together with a pair of so called end-cap electrodes that provide confinement along the z-axis. This design is very successful at confining a register of ions to be used as a quantum processor [58, 59], but it is limited by the availability for only a single potential well. As more ions are added to a potential well, the ratio of radial to axial confinement required increases to keep the ions in a linear string as well as the number of the motional modes. As the spacing between modes decreases, it becomes ever more difficult to control the interaction with the motional modes as the closer spacing makes it harder to resolve the individual modes.

One approach to mitigate the challenges of working with long ion strings is to instead pursue a modular approach and consider operating several potential wells that are controlled by micro-structured DC electrodes. In this *quantum charge-coupled device* (QCCD) architecture [60], the individual registers of ions can then be moved, rotated, split and merged to reconfigure the ion crystals as required during a computation. This promises to be able to maintain the high fidelities achievable in a single trapping region while scaling up to a larger system, as the quantum interactions are always limited to a small sub-register.

The electrode configurations generating a trapping pseudo-potential are not unique. A planar electrode configuration shown on the right in Fig. 3.1 can be used instead, with Fig. 3.2 showing the equipotential lines for two examples of the different kinds of electrode configurations. A planar configuration has the advantage of providing good optical access as one side is entirely unobstructed by the trapping electrodes. They are also well-suited to micro-fabrication technologies that can pattern complex electrode structures [61–63], which are necessary to realize a QCCD architecture.

To control the potential for splitting and merging operations, the fields need to be controlled on the length scale of the ion spacing. As the trapping potentials decrease exponentially as a function of the ion-electrode distance, this becomes more challenging with increasing distance. The length scale is also set by the dimension of the electrodes [64], thus control electrode for these operations typically have sizes that are on the same length scale the ion-electrode distance. This imposes a reduction in scale for traps that implement a QCCD architecture: While bulk traps typically have a spacing between ions and electrodes on the order of $\approx$ 1mm, chip traps are often designed smaller with typical ion-electrode distances of $\approx$ 100µm [65].

A smaller scale lowers the voltages required to achieve the same trap frequencies compared to bulk traps, which is advantageous for the technical requirement on the electronics providing necessary dynamic DC control fields.

A significant challenge of miniaturizing ion traps is that as the distance to the surface of the nearest electrode decreases, this leads to an increased sensitivity to the electric field noise present on those electrodes. That in turn can alter the state of motion of the ion crystal, causing motional heating [65].

A further disadvantage of the surface geometry is that the potential barrier perpendicular to the trap surface is low compared to a 3D-trap, which increases the chance of an ion loss after an event like a background gas collision.

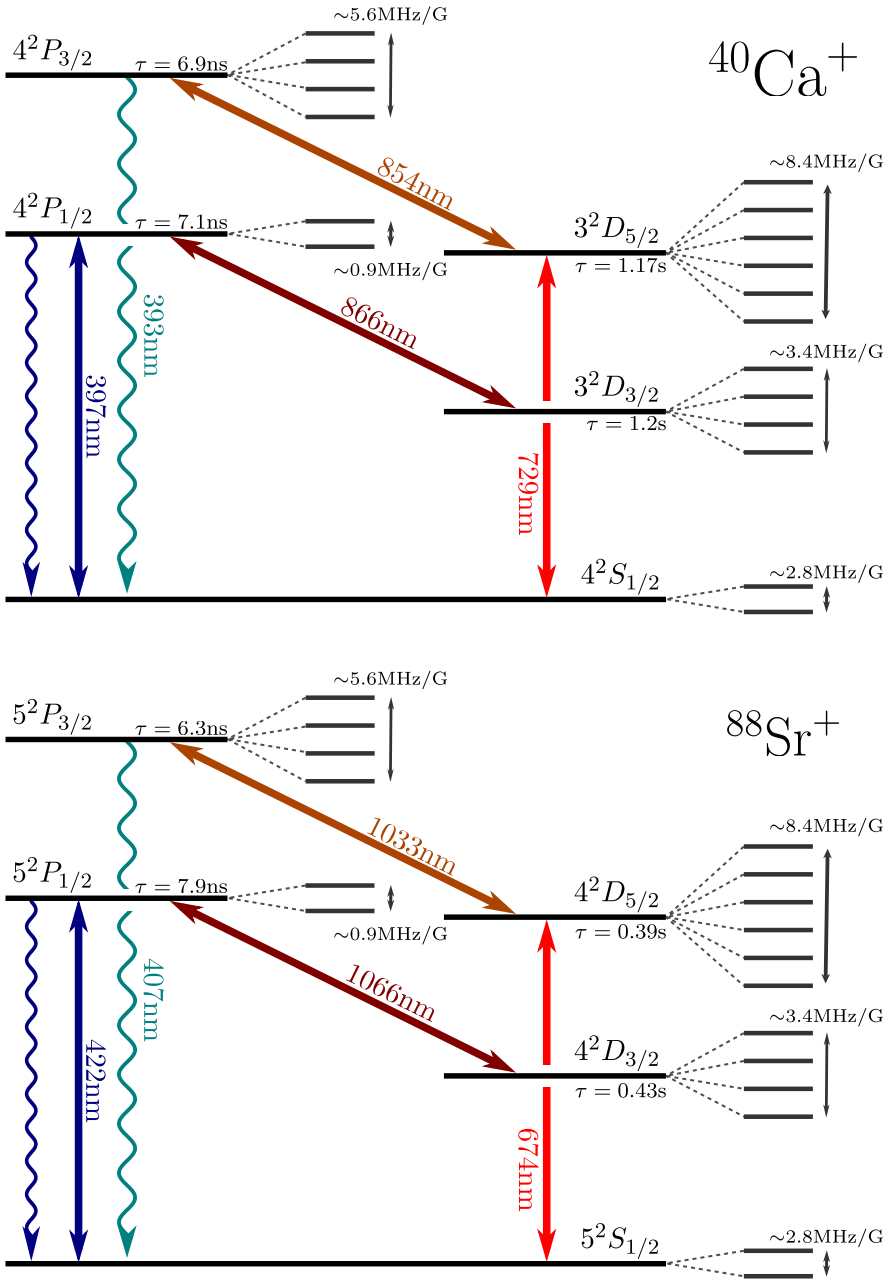

Figure 3.3: Levels for $^{40}Ca^+$ and $^{88}Sr^+$ and the relevant transitions for quantum information operations. The $S_{1/2} \leftrightarrow P_{1/2}$ transition allows for cooling and state detection. The $S_{1/2} \leftrightarrow D_{5/2}$ transition is used for manipulating the encoded information. The $D_{5/2} \leftrightarrow P_{3/2}$ transition is used to reset the state, while the $D_{3/2} \leftrightarrow P_{1/2}$ transition returns population that decayed to the $D_{3/2}$ state. The lifetimes and transition wavelengths are tabulated in Tables E.1 and E.2.

3.2 CALCIUM + STRONTIUM

While ion traps can confine any kind of charged particle, only a few selected species have the properties desirable for implementing quantum operations. For laser-cooling the ions a closed-cycling transition is required (see Section 3.4), where photons are scattered repeatedly while the ions remain in a preferably small number of electronic levels. Long-lived states are necessary to store information, and a state dependent detection method to read out that information. Typically atoms with 2 electrons in the occupied shell with the highest energy are chosen such as Earth alkali metals, which after single ionization leaves the atom with a hydrogen-like level structure. Practical considerations involve the availability of appropriate laser sources and optical components to drive the necessary transitions. For multi-species operation the mass ratio between species becomes relevant, as it determines how similar the trapping parameters for the different species. The larger the difference, the smaller the region of stable parameters for both species becomes. Furthermore the mass difference changes the participation of the species in the normal modes of motion [66].

Both $^{40}Ca^{+}$and $^{88}Sr^{+}$are suitable atomic species for quantum information processing applications, sharing a very similar level structure, which is described in the following subsection.

3.2.1 *Atomic Level Structure*

Figure 3.3 gives an overview of the important atomic levels for quantum information processing applications for both $^{40}Ca^{+}$and $^{88}Sr^{+}$, with their usage described in the following:

The two sub-levels of the $4^2S_{1/2}$ ground state have functionally infinite lifetime, with the coherence only limited by the stability of the magnetic field that determines their energy splitting, making it possible to also encode information between the two levels. Transitions between these two states can be mediated via Raman interactions by laser beams detuned from the $4^2S_{1/2} \leftrightarrow 4^2P_{1/2}$ transition.

In $^{40}Ca^{+}$the $4^2S_{1/2} \leftrightarrow 4^2P_{1/2}$ transition at 397nm allows for a closed cycling transition, with only a single additional laser at 866nm required. This laser returns population that decays into the $3^2D_{3/2}$ level to the cycling transition, which is critical for cooling the ions (Section 3.4).

The $3^2D_{5/2}$ level is long lived ($\approx$ 1.1s) as the decay to $4^2S_{1/2}$ is dipole-forbidden, making it suitable to define a qubit between the $3^2D_{5/2}$ and the $4^2S_{1/2}$ level. The state is also inaccessible from the states involved in the closed cycling transition. It is thus excellently suited to enable state dependent readout, with the only error channel being the spontaneous decay of the $3^2D_{5/2}$ to the ground state.

The transition can be driven via its quadrupole element by a laser at 729nm to manipulate the quantum information, which will be described in more detail in Section 3.5.

A transition at 854nm $3^2D_{5/2} \leftrightarrow 4^2P_{3/2}$ allows resetting the state, returning all population to the $4^2S_{1/2}$ manifold via spontaneous decay.

The techniques just illustrated can be directly mapped to the very similar level scheme of $^{88}Sr^+$shown in Fig. 3.3, where instead the ground state is the $5^2S_{1/2}$ level. The closed-cycle transition $5^2S_{1/2} \leftrightarrow 5^2P_{1/2}$ lies at 422nm, with a laser at 1064nm to return population. The $4^2D_{5/2}$ state has a shorter lifetime of $\approx$ 0.4s than its equivalent in calcium, but can be utilized in the same way.

A technical advantage for choosing $^{40}Ca^+$and $^{88}Sr^+$is the availability of laser systems (See Section 4.4) and optics, avoiding the need for light at deeper UV frequencies of other popular species (313nm for $^9Be^+$, 279nm for $^{25}Mg^+$, 369nm for $^{171}Yb^+$). The values for the relevant transition frequencies, branching rations and lifetimes have been summarized in Appendix E.

3.3 ATOM-LIGHT INTERACTION

As the techniques used in this thesis for manipulating trapped ions rely on lasers, we need to understand the interaction of light with the atom. This topic has been extensively discussed in the literature, [57, 67–69] and will review the theory in the following.

For simplicity we will consider only two electronic levels $|g\rangle$ and $|e\rangle$, and a single motional mode of a harmonic oscillator formed by the atom being confined in the potential of the trap. The Hamiltonian of the non-interacting system is then given by

$$H_0 = H_{\text{motion}} + H_{\text{elec}} = \frac{\hat{p}^2}{2m} + \frac{m\omega_m^2}{2}\hat{x}^2 + \frac{\hbar\omega_{eg}}{2}\sigma_z \tag{3.14}$$

where m is the mass of the atom, ω_{eg} the transition frequency of the 2 levels, ω_m the motional frequency of the harmonic oscillator, $\hat{p}$ and $\hat{x}$ are the momentum and position operators of the oscillator while σ_z is the Pauli-z matrix operator acting on the electronic levels.

With the common substitution of creation and annihilation operator for position and momentum, the motional part of the Hamiltonian H_{motion} can be simplified to

$$H_{\text{motion}} = \hbar\omega_m(a^\dagger a + \frac{1}{2}). \tag{3.15}$$

For a quantum harmonic oscillator, the motional state can be expressed using number or Fock states $|n\rangle$ [57] where $a^\dagger a\,|n\rangle = n\,|n\rangle$.

We model the light as a planar wave with frequency ω_l and a phase ϕ, where we assume for simplicity that its wave vector $\vec{k}$ is aligned

with the motional mode. The interaction Hamiltonian is then given by [57]

$$H_{\text{int}} = \frac{\hbar\Omega}{2}(\sigma_+ + \sigma_-)(e^{i(kx-\omega_l t+\phi)} + e^{-i(kx-\omega_l t+\phi)}) \tag{3.16}$$

where Ω gives the coupling strength of the interaction, The expression can be simplified by introducing the Lamb-Dicke parameter which is defined by

$$\eta = k\sqrt{\frac{\hbar}{2\omega_m m}}. \tag{3.17}$$

Inserting the raising and lowering operators through a substitution of $k\hat{x} = \eta(a^\dagger + a)$ allows rewriting the interaction as

$$H_{\text{int}} = \frac{\hbar\Omega}{2}(\sigma_+ + \sigma_-)\left(e^{i\left(\eta(a^\dagger+a)-\omega_l t+\phi\right)} + e^{-i\left(\eta(a^\dagger+a)-\omega_l t+\phi\right)}\right) \tag{3.18}$$

As the transition frequency between the levels is much higher than those of the motional mode or the frequency difference between laser and transition $\omega_{eg} \ll \omega_m,\ \omega_{eg} - \omega_l$, we can perform a rotating wave approximation, where we change into an interaction picture rotating at frequency ω_{eg} and neglect fast terms that rotate at $2\omega_{eg}$, letting us simplify the interaction Hamiltonian to

$$H_{\text{int}} = \frac{\hbar\Omega}{2}\left(\sigma_+ \exp\left(i\eta(a^\dagger e^{i\omega_m t} + ae^{-i\omega_m t})\right)\exp(i(\phi - \Delta t)) + h.c.\right), \tag{3.19}$$

where $\Delta = \omega_{\text{eg}} - \omega_{\text{light}}$ is the frequency difference between the transition and the light field.

If the oscillation amplitude is small relative to the size of the wavepacket, we enter the Lamb-Dicke regime where $\eta^2(2n+1) \ll 1$, and it is possible to perform the Lamb-Dicke approximation where we expand the Hamiltonian in η to first order, obtaining

$$H_{\text{int}} = \frac{\hbar\Omega}{2}\left(\sigma_+\left(1 + i\eta\left(a^\dagger e^{i\omega_m t} + ae^{-i\omega_m t}\right)\right)e^{i(\phi-\Delta t)} + h.c.\right). \tag{3.20}$$

We are left with three terms in the Hamiltonian corresponding to different frequencies for which we drive dynamics between the electronic states, which we identify as the carrier transition, and the red and blue sideband transition. If we choose a frequency close to the carrier transition ($|\Delta| \lesssim \Omega$), the light will induce a coherent population transfer between the states $|g\rangle$ and $|e\rangle$ called *Rabi oscillations* [30]. Starting from an initial state in $|g\rangle$ the probability for the excited state population is given by [70]

$$P(|e\rangle, t) = \frac{\Omega^2}{\Omega^2 + \Delta^2}\sin^2\left(\frac{\sqrt{\Omega^2 + \Delta^2}t}{2}\right) = \frac{\Omega^2}{\Omega_{\text{eff}}^2}\sin^2\left(\frac{\Omega_{\text{eff}}t}{2}\right) \tag{3.21}$$

where we introduce the effective Rabi frequency $\Omega_{\text{eff}}^2 = \Omega^2 + \Delta^2$. These oscillations leave the motion of the ion unaffected.

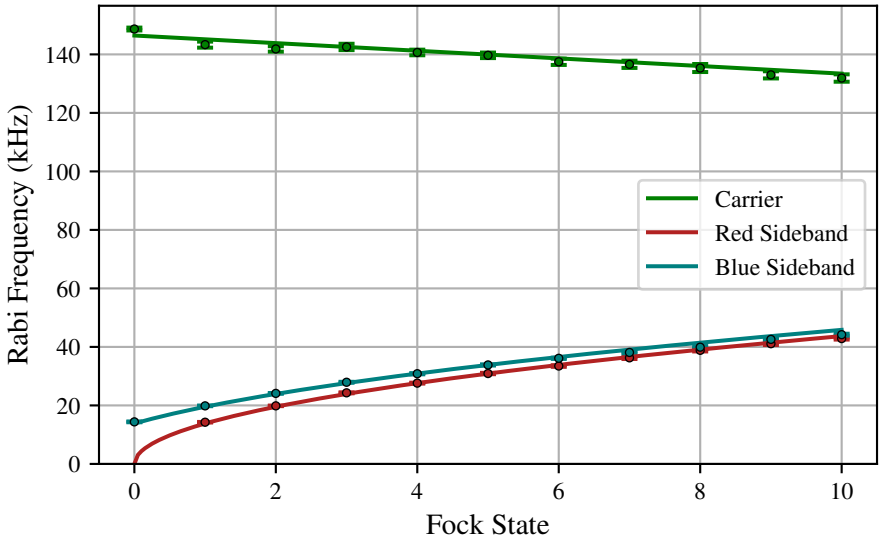

Figure 3.4: Measured Rabi frequency as function of motional state for the carrier and the 1st sideband transitions. The error bars are on the order of the marker size. The solid lines correspond to a single-parameter fit of the Rabi frequency to the theoretical predictions in the Lamb-Dicke regime.

When bringing the frequency detuning Δ of the driving laser field close to the motional frequency either at $-\omega_m$ or ω_m we will drive the same kind of oscillations, but the change in spin state will also be accompanied by a change in the motional state, and the motional state modifies the effective coupling strength. For $\Delta = \omega_m$ a phonon is added to the mode when starting from the state $|g\rangle$, which we identify as *blue sideband*, named as the corresponding wavelength of the driving frequency is shifted towards the blue relative to the carrier. The Rabi frequency is modified compared to Eq. (3.21) given by

$$\Omega_{\text{blue}} = \sqrt{n+1}\eta\Omega, \tag{3.22}$$

and depends on the motional state n of the mode. For $\Delta = -\omega_m$ a phonon is removed from the mode when starting from the state $|g\rangle$, which we identify as *red sideband*. The Rabi frequency on this sideband is then given by

$$\Omega_{\text{red}} = \sqrt{n}\eta\Omega. \tag{3.23}$$

Fig. 3.4 shows the dependency of the Rabi frequencies of the sidebands on the motional state n, with the difference being largest for $n = 0$. The carrier Rabi frequency is also affected by the motional state but only in second order of η, as can be seen in Fig. 3.4. This interaction of the laser with both spin and motion of the ion forms the basis of the manipulation techniques that will be subsequently discussed in Sections 3.4 and 3.5.

3.4 LASER COOLING

The capability for cooling of the ions inside a trap is crucial for experiments for several reasons. First it increases the time ions stay inside the trap, but also once the kinetic energy is sufficiently low, the ions form spatially ordered structures where the individual ions are well localized. Such a structure is known as a Coulomb crystal as the arrangement is controlled by the combination of the mutual repulsive Coulomb interaction between the ions and the external trapping potential. To precisely control coherent interactions even lower temperatures are required, where a high fraction of the population in the motional ground state is wanted.

A variety of cooling techniques can be applied to reduce the kinetic energy of trapped ions. For atomic species that have the appropriate level structure, laser cooling is preferred, but even among them there is a variety of available techniques [57, 68, 71–73]. These cooling techniques have different advantages and disadvantages, trading cooling rate and being effective over a wider range of frequencies for the lowest possible achievable final temperatures. Thus effective cooling relies on a combination of different techniques, two of which are described in the following.

3.4.1 *Doppler Cooling*

The technique of Doppler cooling relies on the Doppler effect, where the apparent frequency of laser light is changed depending on the velocity [68].

The effect can be derived from a particle in free space experiencing a force from the momentum transfer of scattered photons. Each photon carries momentum $\hbar\vec{k}$, and the process occurs at the rate $\Gamma\rho_{ee}$, where Γ is the decay rate of the transition, and ρ_{ee} is the probability of the ion to be in the excited state $|e\rangle$. We can write down the average force acting on the particle as [57]

$$\vec{F}_{\text{avg}} = \langle \frac{d\vec{p}}{dt} \rangle \approx \hbar\vec{k}\Gamma\rho_{ee}. \tag{3.24}$$

The excitation probability ρ_{ee} is given by

$$\rho_{ee} = \frac{s/2}{1 + s + (2\frac{\Delta_{eff}}{\Gamma})^2}, \tag{3.25}$$

where $s = 2\Omega^2/\Gamma^2$ is the saturation parameter on resonance with Ω being the Rabi frequency, while $\Delta_{eff} = \Delta - \vec{k}\vec{v}$ gives the effective detuning between laser frequency and the Doppler shifted transition of the ion.

We are primarily interested in the regime of low velocities, where the spatial extent of the ion shrinks below the wavelength of the

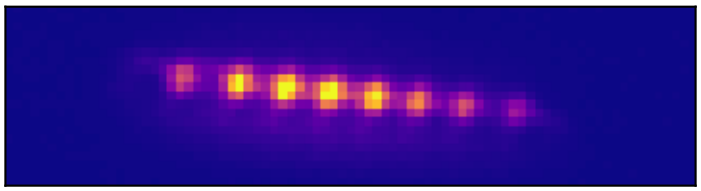

Figure 3.5: Fluorescent light at 397 nm of 8 $^{40}Ca^{+}$ions trapped in a linear configuration imaged on a camera.

laser, and the Doppler shift becomes small compared to the transition linewidth. In this case the force can be linearized in the velocity $\vec{v}$ [57]

$$\vec{F} \approx \vec{F}_0(1 + \vec{\kappa}\vec{v}) = \quad \hbar\vec{k}\Gamma \frac{s/2}{1 + s + 4\Delta^2/\Gamma^2} \left(1 + \frac{8k\Delta\Gamma}{1 + s + 4\Delta^2/\Gamma^2}\vec{v}\right). \tag{3.26}$$

For a red-detuned beam ($\Delta < 0$), the force F is opposed to the velocity, leading to a damping effect. For an ion confined in a trap we can classically write the velocity as a periodic motion $v(t) = v_0 \cos(\omega t)$. The cooling rate can then be calculated by averaging over many oscillation cycles of the ion in the trap, where

$$\dot{E}_{\text{cool}} = \langle \vec{F}\vec{v} \rangle = F_0(\langle \vec{v} \rangle + \kappa \langle \vec{v}^2 \rangle), \tag{3.27}$$

where $\langle \vec{v} \rangle = 0$ for a particle in a harmonic potential.

Due to the random nature of the emission process, the ion cannot cool to zero temperature. Even at zero velocity, it will continue to scatter, gaining momentum from the recoil [57] and thus kinetic energy, creating a heating effect that counteracts the cooling.

This heating effect can be described by the momentum kicks due to absorption and emission. The momentum kicks due to absorption are aligned with the direction of the laser beam, while the kicks of the emission are random. We can average over all directions, where the anisotropy of the emission is described by a geometric scale factor $\xi = 2/5$ for dipole radiation [74], leading to a heating rate of:

$$\dot{E}_{\text{heat}} = \dot{E}_{\text{abs}} + \dot{E}_{\text{em}} = \dot{E}_{\text{abs}}(1 + \xi) \tag{3.28}$$

$$= \frac{(\hbar\vec{k})^2}{2m} \Gamma \rho_{ee} (1 + \xi) \tag{3.29}$$

Neglecting correlations between absorption and emission, which corresponds to a low enough laser intensity such that the transition is not saturated ($\Omega \ll \Gamma$), we can set $\dot{E}_{\text{heat}} = \dot{E}_{\text{cool}}$ and infer the final temperature

$$k_B T = m\langle v^2 \rangle = \frac{\hbar\Gamma}{8}(1 + \xi) \left((1 + s)\frac{\Gamma}{2\Delta} + \frac{2\Delta}{\Gamma}\right), \tag{3.30}$$

which is minimal for a choice of detuning

$$\Delta = \Gamma \frac{\sqrt{1+s}}{2}. \tag{3.31}$$

We can relate a temperature to an average number of motional excitations $\bar{n}$ of an ion in the trap by $\hbar\omega(\bar{n}+1/2) = k_b T$. For calcium we get with an optimal choice of detuning, low saturation $s \approxeq 0$ and a decay rate $\Gamma = 2\pi \cdot 22.4 \cdot 10^6 \mathrm{s}^{-1}$ with a typical trap frequency of $\omega = 2\pi \cdot 1\mathrm{MHz}$ a limit of $\bar{n}_{\min} \approx 7$, while for Strontium ($\Gamma = 2\pi \cdot 20.2 \cdot 10^6 \mathrm{s}^{-1}$) with a trap frequency of $\omega = 2\pi \cdot 0.7\mathrm{MHz}$ we expect $\bar{n}_{\min} \approx 10$.

Effects of micro-motion have been neglected in this treatment here, which can have a significant influence for non-crystallized ions [75], and can increase the residual energy. However, it does not change the cooling dynamics expected from the harmonic trap approximation [76].

The closed cooling transition $S_{1/2} \leftrightarrow P_{1/2}$ used for Doppler cooling is also used for detection. The photons scattered by the ions can be focused onto a camera to form an image of the ions as can be seen in Fig. 3.5, or send the light onto a photo multiplier tube (PMT). This not only confirms the presence of the ions in the trap, but can facilitate state detection relative to the long-lived $D_{5/2}$ state. This does not couple to the closed cooling transition and consequently does not scatter any photons. We can utilize the presence or absence of light scattered by a given ion to infer its electronic state, determining if it is either in the $S_{1/2}$ level or the $D_{5/2}$ level, corresponding to a projective measurement in the σ_z basis.

3.4.2 *Resolved Sideband Cooling*

In the regime where the effective transition linewidth is smaller than the motional sideband frequency $\Gamma < \omega$ it then becomes possible to tune the laser frequency to the red sideband transition $\Delta = -\omega_m$. The condition on the sidebands being resolved means that the targeted transition is predominantly being driven, causing each absorption event to reduce the phonon number by one. In the Lamb-Dicke regime spontaneous decay predominately occurs over the carrier transition, which leaves the motional state unchanged. Fig. 3.6 shows the energy of the combined electronic and motional states, where we can start moving down the sideband ladder, with each cycle removing a phonon until we reach close to the motional ground state. This technique is called resolved sideband cooling.

For a Lorentzian excitation profile of the transition with no detuning from the sideband and an effective Rabi frequency in the Lamb-Dicke regime of $\Omega_{RSB} = \eta\sqrt{n}\Omega$ the cooling rate Γ_{cool} is given by [57]

$$\Gamma_{\text{cool}} = \Gamma_{\text{transition}} \frac{n\eta^2\Omega^2}{\Gamma^2_{\text{transition}} + 2n\eta^2\Omega^2}, \tag{3.32}$$

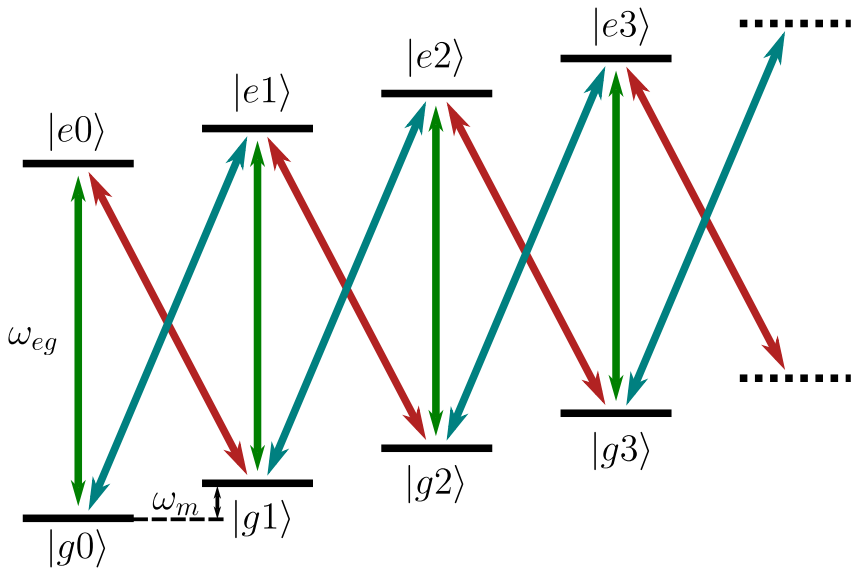

Figure 3.6: STATE LADDER FOR A TWO-LEVEL SYSTEM COUPLED TO A HARMONIC OSCILLATOR. The states are split by ω_{eg} while the levels of the oscillator are separated by ω_m. The red and blue sideband transitions change simultaneously the internal and motional state, while the carrier transitions marked in green do not change the motional state.

where $\Gamma_{\text{transition}}$ is the decay rate of the upper state. Due to the phonon state dependent coupling strength the cooling rate now depends on the current phonon number, disappearing for $n = 0$ as the red sideband becomes suppressed. Given the long-lived nature of the $D_{5/2}$ states in both $^{40}Ca^{+}$and $^{88}Sr^{+}$it would be impractical to attempt to cool them by natural decay. Instead the lifetime is artificially shortened by an additional laser that couples the $D_{5/2}$ to the short-lived $P_{3/2}$ levels, leading to an effective decay rate [77]

$$\Gamma_{\text{transition}} = \frac{\Omega^2_{\text{quench}}}{(\Gamma_{P_{3/2}\to S_{1/2}} + \Gamma_{P_{3/2}\to D_{5/2}})^2 + 4\Delta^2_{\text{quench}}}\Gamma_{P_{3/2}\to S_{1/2}}, \tag{3.33}$$

where $\Omega_{\text{quench}}, \Delta_{\text{quench}}$ are the Rabi frequency and the detuning of the quenching laser. From the $P_{3/2}$ levels the ions decay down to the $S_{1/2}$ state, completing the cycle.

Resolved sideband cooling is limited by competing heating processes. The leading order processes that can heat are off-resonant excitation of the carrier transition followed by a decay on the red sideband, or off-resonant excitation of the blue sideband transition followed by a decay on the carrier. Either of these processes reintroduces a phonon into the system [57]. The probability for off-resonant excitation is $\Omega^2/(4\omega_m^2)$ for the carrier and $\Omega^2/(4(2\omega_m)^2)$ for the sideband, respectively. The chance for a red sideband decay is given by $\eta'^2\Gamma_{\text{transition}}$, the chance for a carrier decay is given by $\Gamma_{\text{transition}}$ instead. The Lamb-Dicke factor η' for the decay is not equal as photons have a

different wavelength and can be scattered in any direction. The rate of heating can then be written as a sum of the two contributions:

$$\Gamma_{\text{heat}} = \frac{\Gamma_{\text{transition}}\Omega^2}{4\omega_m^2}(\eta'^2 + \eta^2/4). \tag{3.34}$$

We can equate in the steady state $\Gamma_{\text{heat}} = \Gamma_{\text{cool}}$ and estimate for small phonon numbers ($2n\eta^2\Omega^2 < \Gamma^2_{\text{transition}}$) the residual phonon number $\bar{n}$ given by

$$\bar{n} = \left(\frac{\Gamma_{\text{transition}}}{2\omega_m}\right)^2 \left(\frac{\eta'^2}{\eta^2} + \frac{1}{4}\right) \tag{3.35}$$

There is a trade-off between the minimal achievable temperature (Eq. (3.35)) and the cooling rate (Eq. (3.32)) depending on the effective decay rate of the upper state, controlled by the quenching laser. No detuning and $\Omega_{\text{quench}} = 2\pi \cdot 300\text{kHz}$ for the quenching laser in $^{40}Ca^+$leads to an effective decay rate of 170kHz, resulting in a theoretical limit on the minimum phonon number of $\bar{n} \approx 0.007$.

3.5 COHERENT CONTROL

In the following we will discuss how we can utilize the interaction of the laser with the ions described in Section 3.3 to coherently manipulate their state, which enables performing the quantum gates required for implementing algorithms.

3.5.1 *Single Qubits*

The atom-light interaction described above in Eq. (3.20) can be used to perform single qubit operations directly. If set on resonance, the interaction performs the rotation

$$R(\theta, \phi) = \exp\left[-i\theta(\sigma_x \cos(\phi) + \sigma_y \sin(\phi))\right] \tag{3.36}$$

where we introduce the rotation angle $\theta = \Omega t$.

For a choice of a pulse duration of $\Omega t = \pi/2$ and a phase of $\phi = 0, \pi/2$ a σ_x, σ_y Pauli operation is performed.

A σ_z operation can be applied by means of the AC Stark effect. From Eq. (3.21) we do not expect any changes of the populations for large detunings $\Delta \gg \Omega$ as the resonant coupling tends to 0, but the applied field will lead to a shift of the energy levels. Under these conditions we can apply the James-Jerke approximation [78] to Eq. (3.20), retaining only the zeroth order term in η to get the following interaction:

$$H_{\text{AC}} = \frac{\hbar\Omega^2}{4\Delta}\sigma_z. \tag{3.37}$$

These AC Stark shifts can also appear as an unwanted source of errors, as applied laser beams can off-resonantly couple to other

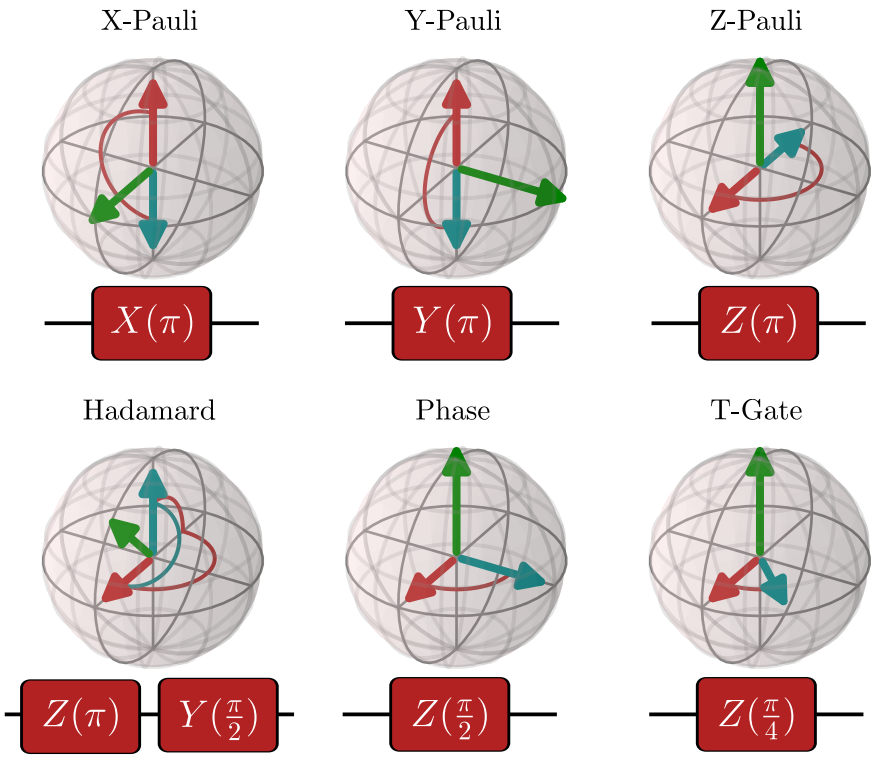

Figure 3.7: GATE SET OF SINGLE QUBIT OPERATIONS. The rotations are illustrated on the Bloch sphere, transforming the starting red state to the final blue state. The Rotation axes are shown in green

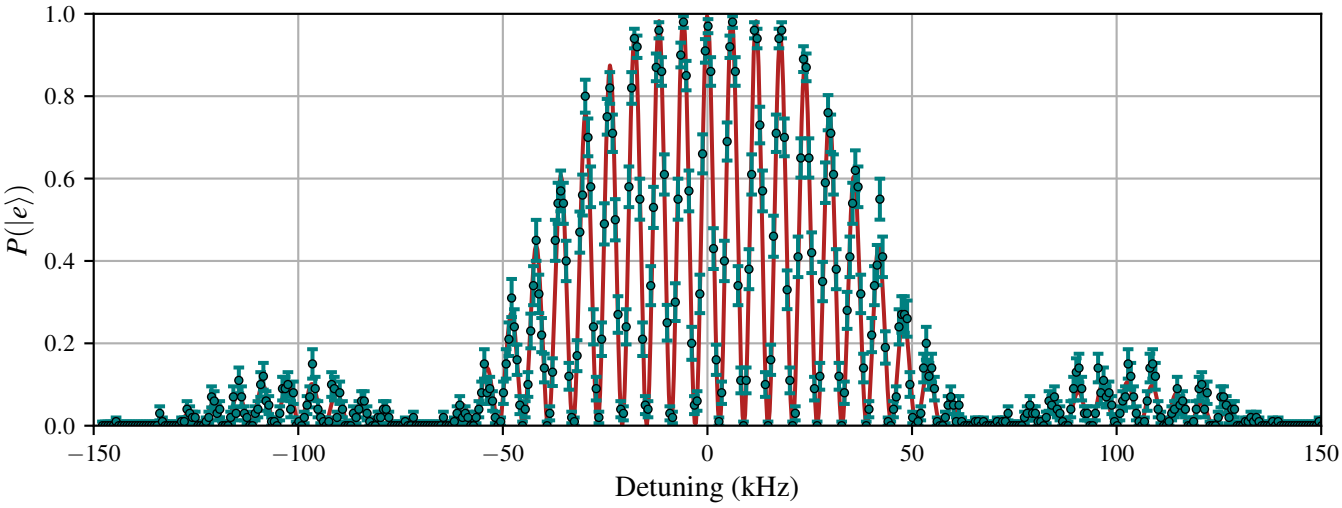

Figure 3.8: EXCITATION OF A RAMSEY EXPERIMENT AS FUNCTION OF FREQUENCY. Ramsey fringes showing the excited state population $P(|e\rangle)$ for a waiting time of 150µs and a Rabi frequency of $\Omega = 2\pi \cdot 17.5\text{kHz}$

transitions, introducing undesirable phase shifts. It should be noted that σ_z gates can also be implemented virtually by adjusting the phase of the frequency reference that controls the phase of the gate laser for other operations [59].

With this toolbox we can implement the single qubit gate set shown in Fig. 3.7 and discussed in Section 2.2.

3.5.2 *Ramsey Measurement*

Coherent rotations of qubits can be used to perform Ramsey experiments [79], a fundamental tool both for performing frequency measurements and characterizing the performance of qubits. This technique involves first applying a $\pi/2$ pulse to the qubit. Then it is left to evolve for a certain wait time, after which a second $\pi/2$ pulse is applied with a phase ϕ relative to the first pulse.

During the wait time the qubit acquires a phase due to any mismatch of the frequency of the laser versus the frequency of the qubit transition, which can originate either from systematic shifts or from noise affecting either the laser or the qubit.

For such an experiment the expected population to be measured in the excited state is given by [80]

$$P(|e\rangle, \tau) = \frac{4\Omega^2}{\Omega_{\text{eff}}^2} \sin^2(\Omega_{\text{eff}} t/2) \Big[\cos(\Omega_{\text{eff}} t/2) \cos(\Delta\tau/2 + \phi) + \frac{\Delta}{\Omega_{\text{eff}}} \sin(\Omega_{\text{eff}} t/2) \sin(\Delta\tau/2 + \phi) \Big]^2, \tag{3.38}$$

where the effective Rabi frequency is given by $\Omega_{\text{eff}} = \sqrt{\Omega^2 + \Delta^2}$. The time t is the duration of the $\pi/2$ laser pulses. The shape of this excitation pattern can be seen in Fig. 3.8, consisting of a slow envelope corresponding to the Rabi coupling to the transition and a fast oscillating term depending on the wait time τ, giving rise to so-called *Ramsey fringes*.

Typically, the detunings of interest are much smaller than the Rabi frequency $\Delta \ll \Omega$, allowing simplification of Eq. (3.38) to

$$P(|e\rangle, \tau) = \frac{1}{2}\left[1 + \cos\left(\Delta(\tau + \frac{4t}{\pi}) + \phi\right)\right] \sin^2(\Omega_{\text{eff}} t/2). \tag{3.39}$$

This type of measurement is frequently used to determine the frequency difference of a transition to the probing laser. For this purpose the measurement is performed with a Rabi frequency $\Omega t = \frac{\pi}{2}$ and a phase of $\pm\pi/2$ of the second pulse relative to the first, resulting in the measured probabilities $P_{+\pi/2}, P_{-\pi/2}$. For $\Delta = 0$ we expect an excitation probability of 50% for both measurements, and the slope of the pattern as function of detuning is maximal. We can connect the measured outcomes to the phase acquired during the experiment by

$$\arcsin\left(\frac{P_{-\pi/2} - P_{+\pi/2}}{P_{-\pi/2} + P_{+\pi/2}}\right) = \Delta\left((\tau + \frac{4t}{\pi})\right), \tag{3.40}$$

allowing us to determine the frequency detuning as long as the total phase acquired is $< \pi/2$[1].

Another application of the Ramsey technique is to measure the coherence of the system. In a quantum computing application the coherence limits the ability to perform the identity operation, on how long a state can be stored. This is crucial as all other quantum operations rely on the information being reliably stored. In this context we assume that the detuning changes between each measurement due to fluctuations of the laser frequency and the qubit transition frequency being affected by noise. We can average Eq. (3.39) over different realizations of the experiment, where for long probe times $t \ll \tau$ we can write the excitation probability as

$$P(|e\rangle, \tau) = \frac{1}{2}\left[1 + C(\tau)\cos\left(\Delta\tau + \phi\right)\right] \sin^2(\Omega_{\text{eff}} t/2), \tag{3.41}$$

where we introduce $C(\tau)$ as the waiting-time dependent contrast given by integrating over the probability distribution $p(\Delta')$ of detunings

$$C(\tau) = \left|\langle e^{i\Delta\tau}\rangle\right| = \left|\int_{-\infty}^{\infty} p(\Delta') e^{i\Delta'\tau} \mathrm{d}\Delta'\right|. \tag{3.42}$$

1 The issue of a wrong frequency estimate due to a too large acquired phase is called fringe hopping, it can be avoided by evaluating the measurements using Bayesian methods as has been shown in [81].

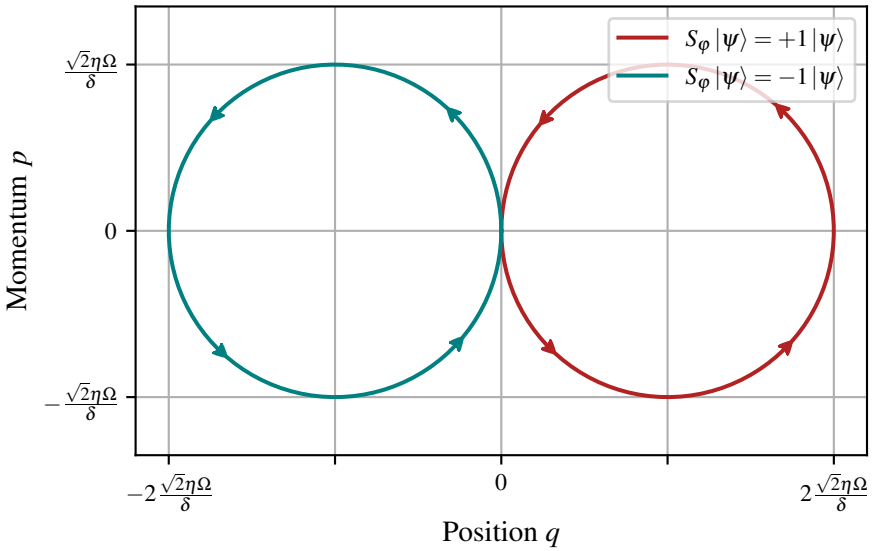

Figure 3.9: TRAJECTORY OF THE GATE IN PHASE SPACE. Shown are the two S_φ eigenstates under the Hamiltonian of the Mølmer Sørensen gate. Notably the trajectories meet at the origin again, leaving the spin and motional states separable.

We can explore the expected contrast for some choices of a probability density function. As Eq. (3.42) describes a Fourier transform, for a Gaussian distribution $p(\Delta) = \frac{1}{\sqrt{\pi}\sigma}\exp\left(-\frac{\Delta^2}{\sigma^2}\right)$ we expect the contrast to follow a Gaussian shape

$$C(\tau) = \exp\left(-\frac{(\sigma\tau)^2}{4}\right). \tag{3.43}$$

If we instead insert a Lorentzian lineshape of $p(\Delta) = \frac{1}{\pi}\frac{\gamma}{\gamma^2+\Delta^2}$ for the frequency detuning fluctuations we expect an exponential decay.

$$C(\tau) = \exp(-\gamma\tau) \tag{3.44}$$

With this we can find conclusions about the noise affecting a qubit from the measured coherence time. A general noise spectral density $p(\Delta)$ can be used to predict the Ramsey contrast [58, 82]

A variant of the Ramsey measurement includes adding a π pulse after half the waiting time. This is known as a *spin echo*, and the spin flip cancels constant phase shifts during a single experiment [83]. This allows us to distinguish the kind of noise affecting the coherence, separating slow sources that introduce phase shifts varying shot-to-shot from fluctuations on timescales faster than the wait time.

3.5.3 *Geometric Phase Gates*

The single-qubit control has to be augmented by an implementation of the CNOT gate to complete the gate set as previously discussed

in Section 2.2. This gate can be directly implemented using the Cirac-Zoller scheme [21], but a different type of gate has proven itself as the primary way for mediating interactions in trapped ion systems; the geometric phase gates, as this type of gate is more robust to the initial phonon state. They rely on spin-dependent forces that couple to the motion, producing closed trajectories in phase space. Fig. 3.9 shows the trajectory taken depending on the initial state of the system due to the spin-dependency of the force. At the point where the paths close, the spins and the motion are separable again, leaving a phase conditional on the path taken [84]. Different physical mechanisms allow generating a spin-dependent force. In the following we will look at a way to produce a $\sigma_x\sigma_x$ type interaction leading to a gate known as the Mølmer-Sørensen gate [85, 86], and subsequently we will discuss a mechanism that generates a $\sigma_z\sigma_z$ interaction, which is known as a light-shift gate [87].

3.5.4 *Mølmer-Sørensen Gate*

The Mølmer-Sørensen gate couples two qubits mediated via a shared motional mode, with a bichromatic drive field detuned from the shared mode, coupling the spin state of the ions with the motion. Fig. 3.10 shows the four possible paths by which the bichromatic field couples the $|gg\rangle$ to the $|ee\rangle$ state.

In the following we will review how the laser interaction can produce the desired gate action on the qubits. Given the Hamiltonian of the atom-light interaction described in Eqs. (3.14) and (3.16), the system of two qubits and a single motional mode can be described by the following Hamiltonian

$$H = H_0 + H_{\text{int}} \tag{3.45}$$

$$H_0 = \sum_{j=1}^{2} \frac{\hbar\omega_{eg}}{2}\sigma_{z,j} + \hbar\omega_m(a^\dagger a + 1/2) \tag{3.46}$$

$$\begin{aligned} H_{\text{int}} = &\sum_{j=1}^{2}\sum_{i=1}^{2} \frac{\hbar\Omega(t)}{2}(\sigma_j^+ + \sigma_j^-) \\ &\times [e^{i(\vec{k}_i\vec{x}_j - \omega_i t + \phi)} + e^{-i(\vec{k}_i\vec{x}_j - \omega_i t + \phi)}] \end{aligned} \tag{3.47}$$

where the frequencies ω_i correspond to the two laser frequencies of the bichromatic drive field, while j indexes the two ions.

We can rewrite the frequencies of the two tones of the laser as a combination of the symmetric ($\omega_s = (\omega_1 - \omega_2)/2$) and asymmetric ($\omega_a = (\omega_1 + \omega_2)/2 - \omega_{eg}$) detuning from the qubit transition frequency ω_{eg}:

$$\omega_1 = \omega_{eg} + \omega_s + \omega_a, \tag{3.48}$$

$$\omega_2 = \omega_{eg} - \omega_s + \omega_a \tag{3.49}$$

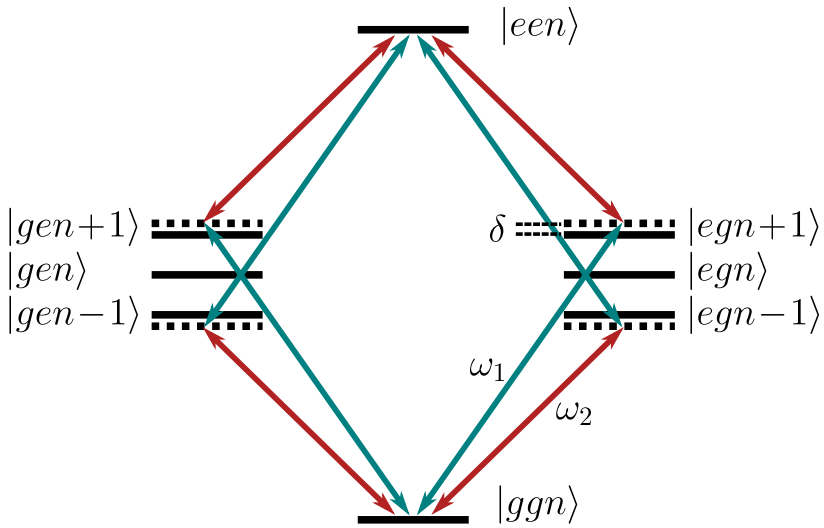

Figure 3.10: LEVEL SCHEME OF THE MØLMER-SØRENSEN GATE. The bichromatic laser beam with frequencies ω_1 (blue), ω_2 (red) couples the symmetric internal state via the levels with asymmetric levels with ± 1 phonon with a detuning δ.

The combination of AC stark shifts of the electronic levels and the asymmetric detuning create a so called *center line detuning* of $\omega_{cl}(t) = \omega_{AC}(t) - \omega_a$ between the mean of the bichromatic frequencies and the carrier transition.

We can then go to the interaction picture and apply the rotating wave approximation, allowing us to discard any fast rotating terms at $2\omega_{eg}$, leaving us with

$$\begin{aligned}\hat{H}_{\text{int}} = &\sum_{j=1}^{2} \frac{\hbar\Omega(t)}{2}(\sigma_j^+ + \sigma_j^-) \\ &\times \left[e^{i(\vec{k}_1\vec{x}_j - (\omega_{cl}+\omega_s-\omega_m)t+\phi)} + e^{i(\vec{k}_2\vec{x}_j - (\omega_{cl}-\omega_s+\omega_m)t+\phi)} + h.c.\right].\end{aligned} \tag{3.50}$$

We then introduce the detuning $\delta = \omega_m - \omega_s$ as the difference between the motional mode frequency and the symmetric detuning. Furthermore, we can rewrite the position and momentum term as $\vec{k}\cdot\vec{x} = \eta_i(a^\dagger + a)$, where η_i is the Lamb-Dicke factor of the ith tone. However, since $\omega_d \ll \omega_{eg}$, we can approximate them as $\eta_1, \eta_2 \approx \eta$. As we operate in the Lamb-Dicke regime, we can perform the same expansion of the exponential as in Eq. (3.20), keeping only up to the first order terms in η:

$$\begin{aligned}\hat{H}_{\text{int}} = &-\eta\hbar\Omega(t)(a^\dagger e^{i\delta t} + a e^{-i\delta t}) \\ &\times \left[S_y \cos(\phi + \Lambda(t)) + S_x \sin(\phi + \Lambda(t))\right],\end{aligned} \tag{3.51}$$

where we used the spin operators

$$S_\alpha = \frac{1}{2}\sum_{j=1,2}\sigma_{\alpha,j}, \quad \alpha = x,y,z \tag{3.52}$$

and $\Lambda(t)$ contains the integrated phase due to any center line detuning, defined as

$$\Lambda(t) \equiv \int_0^t \omega_{cl}(t')dt'. \tag{3.53}$$

Ideally the gate applied does not include any center line detuning, leading to the case of $\Lambda(t) = 0$. Under this condition the Hamiltonian can then be exactly integrated to obtain the evolution operator [86]

$$\hat{U} = D[\gamma(t)S_\phi]\exp\left[i\theta(t)S_\phi^2\right], \tag{3.54}$$

$$\gamma(t) = i\eta\hbar\int_0^t \Omega(t')e^{i\delta t'}\mathrm{d}t', \tag{3.55}$$

$$\theta(t) = (\eta\hbar)^2\,\mathrm{Im}\left\{\int_0^t\int_0^{t'}\Omega(t')\Omega(t'')e^{-i\delta(t'-t'')}\mathrm{d}t''\mathrm{d}t'\right\}, \tag{3.56}$$

where $D[\alpha]$ is the displacement operator and we introduce the spin operator $S_\phi = S_y\cos(\phi) + S_x\sin(\phi)$. For a constant $\Omega(t) = \Omega$, the integrals can be simplified to

$$\gamma(t) = \frac{\eta\Omega}{\delta}\sin\left(\frac{\delta t}{2}\right)e^{i\delta t/2}, \tag{3.57}$$

$$\theta(t) = \frac{(\eta\Omega)^2}{\delta^2}(\delta t - \sin(\delta t)). \tag{3.58}$$

To implement the desired gate action entangling the two qubits involved, we need to choose the proper gate parameters for the evolution in Eq. (3.55): As we do not want any residual entanglement with the motional mode remaining, we want $\gamma(t_g) = 0$ at the gate time t_g, ensuring that the gate operation causes no displacement of the final motional state relative to the starting state. In case of a square pulse profile, this occurs at every full period of the oscillating term of Eq. (3.58):

$$|\delta| = 2\pi K/t_g, \tag{3.59}$$

where the integer K is the number of loops performed. For the MS gate we will only use the single loop case of $K = 1$. The previous condition allows us to only consider the spin states, where the action with $\phi = 0$ is now described by

$$\begin{aligned}\hat{U}_{MS} &= \exp\left[i\theta S_x^2\right] \\ &= \begin{pmatrix} \cos(\theta/2) & 0 & 0 & -i\sin(\theta/2) \\ 0 & \cos(\theta/2) & -i\sin(\theta/2) & 0 \\ 0 & -i\sin(\theta/2) & \cos(\theta/2) & 0 \\ -i\sin(\theta/2) & 0 & 0 & \cos(\theta/2) \end{pmatrix}.\end{aligned} \tag{3.60}$$

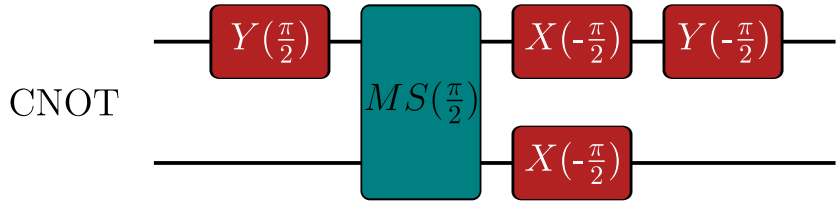

Figure 3.11: Decomposition of the CNOT gate into an Mølmer-Sørensen gate and local rotations on the qubits.

Further we typically want to drive a gate with a rotation angle of $\theta = \pi/2$ to obtain entanglement between the qubits. For a square pulse this results in a condition on the effective Rabi frequency of

$$(\eta\Omega)^2 t_g/\delta = \pi/2\,. \tag{3.61}$$

Fig. 3.11 shows how the Mølmer-Sørensen gate can be used to implement a CNOT gate by adding local rotations before and after the entangling gate, completing the universal gate set, and thus any circuit can be also written as a composition of Mølmer-Sørensen gates and local rotations.

3.5.5 *Light-Shift Gate*

The light-shift gate is an alternative method to generate interaction between a pair of ions. Like the Mølmer-Sørensen gate, it relies on producing a spin-dependent force to drive a closed loop in phase space.

The gate is realized using a pair of Raman beams that produce a standing wave, which generates spatially varying light shifts on the qubits. We can write the Hamiltonian of a pair of beams indexed by i on a pair of ions indexed by j in the interaction picture as [57]

$$H_{\text{int}} = \sum_{j=1,2}\sum_{i=1,2}\sum_{s\in\{e,g\}} -\frac{\hbar\Omega_{i,s}}{2}\left|a_j\right\rangle\left\langle s_j\right| e^{i(\vec{k}_i\vec{r}_j-\delta_{i,s}+\varphi_i)} + h.c., \tag{3.62}$$

where r_j is the position of the j-th ion, $\Omega_{i,s}$ denotes the coupling of each state $|s\rangle$ to the auxiliary state $|a\rangle$ generated by both Raman beams, and $\delta_{i,s}$ describes the detuning from the respective $|s\rangle \leftrightarrow |a\rangle$ transition, while φ_i is the phase of that beam. We now assume that the difference in detunings is much smaller than the absolute detuning from the respective transitions $|\delta_{1,s} - \delta_{2,s}| \ll |\delta_{1,s}|, |\delta_{2,s}|$ such that we can apply the James-Jerke approximation [78].

The result is a combination of time-dependent and time-independent light shifts with no population transfer between the states $|a\rangle$ and either of the $|s_j\rangle$ states [78].

$$H_{\text{int}} = \sum_{j=1,2} \sum_{s\in\{e,g\}} \left\{ -\frac{\hbar\Omega_{1,s}\Omega_{2,s}}{4\Delta_s} |s_j\rangle\langle s_j| \left[e^{i\vec{\delta k}\vec{r}_j - \omega t + \phi} + h.c. \right] + \sum_{i=1,2} \frac{\hbar\Omega_{i,s}^2}{4\Delta_{i,s}} (|s_j\rangle\langle s_j| - |a\rangle\langle a|) \right\}, \tag{3.63}$$

where $\omega = \Delta_{2,s} - \Delta_{1,s}$ is the difference frequency between the beams and $\frac{1}{\Delta_s} = \frac{1}{2}(\frac{1}{\Delta_{1,s}} + \frac{1}{\Delta_{2,s}})$. Notably, this interaction does not affect the population of the ions. Since we do not expect any populations in the auxiliary state $|a\rangle$, we can drop the terms affecting only this state.

We can rewrite the positions $\vec{r}_j = \vec{r} + \vec{\delta r}_j$, where $\vec{r}_j$ are the offsets from the equilibrium position of the ion crystal. Restricting ourselves to the center-of-mass (COM) mode, the term $\vec{\delta k} \cdot \vec{r}$ can be written as $\eta(a + a^\dagger)$. We can now switch to the interaction picture with regards to Eq. (3.47) and take the Lamb Dicke approximation and expand the exponential to first order, resulting in equation

$$\begin{aligned} H_{\text{int}} = \sum_{j=1,2} \sum_{s\in\{e,g\}} \Bigg\{ -\frac{\hbar\Omega_s}{2} |s_j\rangle\langle s_j| \Big[& 2\cos\left(\vec{\delta k}\vec{\delta r}_j - \omega t + \phi\right) \\ & + i\eta \left(a e^{i(\vec{\delta k}\vec{\delta r}_j - (\omega-\omega_m)t + \phi)} + a^\dagger e^{i(-\vec{\delta k}\vec{\delta r}_j + (\omega-\omega_m)t + \phi)} \right. \\ & \left. - a e^{-i(\vec{\delta k}\vec{\delta r}_j - (\omega+\omega_m)t + \phi)} - a^\dagger e^{-i(-\vec{\delta k}\vec{\delta r}_j + (\omega-\omega_m)t + \phi)} \right) \Big] \\ & + \sum_{i=1,2} \frac{\hbar\Omega_{i,s}^2}{4\Delta_{i,s}} (|s_j\rangle\langle s_j|) \Bigg\}, \end{aligned} \tag{3.64}$$

where we introduced the effective Rabi frequency $\Omega_s = \frac{\Omega_{1,s}\Omega_{2,s}}{2\Delta_s}$. The time-dependent light shift oscillating at ω becomes small for $\omega \gg \Omega_s$ and can furthermore be minimized by shaped pulses [88, 89]. We now choose a difference frequency close to the motional mode $\delta = \omega_m - \omega$, $|\delta| \ll \omega_m$ allowing us to neglect the terms oscillating at $\omega_m + \omega$. As the non-time-dependent frequency shifts commute with the time dependent terms, we will later address them separately. We are left with the terms

$$H_{\text{int}} = \sum_{j=1,2} \sum_{s\in\{e,g\}} -\frac{\hbar\Omega_s}{2} |s_j\rangle\langle s_j| \, i\eta \left[a e^{i(\vec{\delta k}\vec{\delta r}_j - \delta t + \phi)} + a^\dagger e^{i(-\vec{\delta k}\vec{\delta r}_j + \delta t + \phi)} \right]. \tag{3.65}$$

We can identify this as a spin-dependent force, where we can apply the same kind of integration that was used on the Hamiltonian of the Mølmer-Sørensen gate to find the propagator

$$\hat{U} = D[\gamma(t)\Gamma] \exp\left[i\theta(t)\Gamma^2\right], \tag{3.66}$$

$$\Gamma = \sum_{j=1,2} \sum_{s\in\{e,g\}} -\frac{\hbar\Omega_s}{2} \left|s_j\right\rangle \left\langle s_j\right| e^{i\vec{\Delta k}\vec{r_j}}, \tag{3.67}$$

$$\gamma(t) = \frac{\eta}{\delta} \sin\left(\frac{\delta t}{2}\right) e^{i(\phi-\delta t/2)}, \tag{3.68}$$

$$\theta(t) = \frac{\eta^2}{\delta^2}(\delta t - \sin(\delta t)). \tag{3.69}$$

where $D[\alpha]$ is the displacement operator and we introduce the spin operator Γ to describe the interaction on the electronic states. $\gamma(t)$ has the same form as for the Mølmer-Sørensen gate, and consequently the displacement vanishes at times $\delta t = 2\pi$, decoupling the spins and the state of motion. This Hamiltonian gives different forces on the four possible state combinations which are listed in the following for a choice of $\phi = -\vec{\Delta k}\cdot\vec{r_1}$ and $\Delta\phi = \vec{\Delta k}\cdot\vec{r_2} - \vec{\Delta k}\cdot\vec{r_1}$

$$\begin{aligned} |ee\rangle &: \Omega_{e,1} + e^{i\Delta\phi}\Omega_{e,2} \\ |eg\rangle &: \Omega_{e,1} + e^{i\Delta\phi}\Omega_{g,2} \\ |ge\rangle &: \Omega_{g,1} + e^{i\Delta\phi}\Omega_{e,2} \\ |gg\rangle &: \Omega_{g,1} + e^{i\Delta\phi}\Omega_{g,2} \end{aligned} \tag{3.70}$$

where $\vec{r}$ corresponds to the separation of the ions. As long as the phase acquired by the even states $|ee\rangle, |gg\rangle$ is different from the phase acquired by the odd states, the interaction acts as an entangling gate, but for maximizing efficiency, we want to control the phase $\Delta\phi$ to maximize the phase difference.

We have previously neglected the time-independent frequency shifts. These can be addressed in different ways; for qubits in the Zeeman manifold of the same species, the shifts can be canceled by choosing the appropriate polarization to equalize the Rabi frequencies $\Omega_g = -\Omega_e$, setting the shifts for $|gg\rangle, |ee\rangle$ to zero while $|ge\rangle, |eg\rangle$ experience the same force amplitude $\pm(\Omega_e + \Omega_g)$. For cases where the coupling cannot be equalized such as mixed species gates or optically encoded qubits, a spin-echo sequence can be used to balance the force on the states $|ge\rangle, |eg\rangle$. As the propagator of the light-shift gate

$$\hat{U}_{LS} = \exp\left[i\theta S_z^2\right] \tag{3.71}$$

matches the propagator of the Mølmer-Sørensen gate Eq. (3.60) up to a basis change, a similar composition can be used to implement the CNOT gate, and thus it can also be used to form a complete gate set.

The gate that has been just described can be generalized to be applied to more than two states $|s\rangle$ per ion, where the following Hamiltonian can be derived

$$H = \sum_j \sum_s \frac{i\hbar\eta}{2} \Omega_{s,j} |s_j\rangle \langle s_j| \left(e^{-i(\delta t+\phi)} e^{i\vec{\Delta k}\vec{r_{0,j}}} a^\dagger + h.c. \right). \tag{3.72}$$

We can integrate this Hamiltonian to produce phase shifts on the pair of ions after closing the loop in phase space. We now assume the couplings to both ions to be equal $\Omega_{s,1} = \Omega_{s,2} = \Omega_s$ and choose an encoding of states such that $\Omega_0 \gg \Omega_s$ for $s > 0$. This can be practically achieved by selecting one state from the $S_{1/2}$ manifold and a set of states from the $D_{5/2}$ manifold, with a detuning close to the $S_{1/2} \leftrightarrow P_{1/2}$ transition such that the differences in detuning between different $D_{5/2}$ states are negligible. In this case the phase shifts are now given by

$$\widetilde{\Phi}_{ij} = \begin{cases} \Phi_{00} & \text{if } i = 0 \\ \Phi_{\text{odd}} & \text{if } i = 0 \text{ or } j = 0 \\ \approx 0 & \text{if } i > 0, j > 0 \end{cases}. \tag{3.73}$$

This interaction can be symmetrized by interleaving multiple applications of this interaction with cyclic permutations where the populations are transferred to the level with the next higher index each. These cyclic permutations for dimension d take the form of

$$X_d = \sum_{j=0}^{d-1} |j+1 \pmod d\rangle \langle j|, \tag{3.74}$$

which can be implemented by a succession of $d-1$ π-pulses between the 0th and each successive level $j > 0$. In this scheme, each logical state spends the same amount of time in each physical state, symmetrizing the phases imprinted on the levels:

$$G(\theta) = \begin{cases} |jj\rangle \rightarrow |jj\rangle \\ |jk\rangle \rightarrow \exp(i\theta) |jk\rangle & \text{if } j \neq k \end{cases}. \tag{3.75}$$

This operator generates qudit entanglement with a single gate operation as opposed to merely embedding qubit-level entanglement in a larger Hilbert space.

3.6 CHALLENGES FOR SCALING ION TRAP TECHNOLOGY

Ultimately the goal of a quantum processor is to be capable of solving problems of interest in fields of science that cannot be solved on classical hardware. There is a major challenge in scaling up ion trap hardware to the size required for accomplishing this task. The difficulty stems from the fact that this scaling requires simultaneously

more and higher fidelity gates. However, many error sources scale with the number of qubits, decreasing performance of the gates. For example, as more ions are added, the axial mode frequency needs to be decreased to keep the ions in a linear string, which leads to both higher heating rates and decreased cooling performance. Furthermore the spacing between individual modes decreases, leading to mode crowding that makes it harder to isolate any particular mode.

As a consequence we want to limit the number of qubits stored in a single potential well. Instead a large scale architecture will require multiple trapping sites in order to retain high-fidelity control over the ions in each register, but this also requires methods to connect the different sites. This decoupling comes at the disadvantage that the all-to-all connectivity in a single crystal is lost, leading to more overhead. Furthermore connecting sites by splitting and merging the crystal is generally slower than gate operations inside a single register, making them costlier in terms of decoherence being acquired.

Quantum error correction promises to be able to boost fidelities once a certain threshold for the fidelity of gate operations is exceeded by redundantly encoding quantum information and correcting for errors that occur during operations. This redundant encoding has a cost, as it comes with a significant increase in the number of physical qubits required and the error correction by itself requires gate operations to be performed. Error correction does introduce additional challenges of mid-sequence readout, which is necessary for identifying if and where an error has occurred. For this process to be beneficial, the readout must not compromise the information stored in other qubits. Furthermore, most readout schemes lead to heating of the ion, which will affect logic operations following the readout.

The experimental setup described in the following chapter is designed to tackle several of these challenges. By using a segmented trap, the ions can be split up into several independent wells; and by using two species, this enables the possibilities of using one species for readout and cooling during a sequence, without affecting the ions of the other species. We developed an automatic calibration algorithm that is suitable for ensuring high fidelity entangling gate operations, which is crucial for future operation of multiple parallel trapping and interaction sites. Finally we investigated light-shift gates in two different applications. It was used to implement a mixed-species entangling gate, where this capability enables using the second species as an ancilla qubit that can be read out independently. We demonstrate a novel gate for generating qudit entanglement. While qudits cannot be scaled indefinitely given the limited suitable electronic levels available, they offer an interesting pathway to increase the capability of a single register in a larger architecture without increasing the particle count.

4

EXPERIMENTAL SETUP

In this chapter, the components of the experimental setup are discussed, with a particular focus on the changes and improvements made during this work. The setup is an evolution of the apparatus designed by Matthias Brandl [90, 91], which was named Cryostina by him. The experimental setup has been modified during the course of this thesis to accommodate a new generation of traps.

In the first section the vacuum assembly housing the ion trap is described, followed by the electronic components and the control system of the experiment. Next the laser systems for manipulating the ions are presented, and the detection optics is discussed. The chapter concludes with the trap that was utilized for the work presented in the following chapters.

4.1 VACUUM CHAMBER

The cryogenic vacuum system is the core of the experimental setup: It houses the ion trap in the UHV environment required for trapping and manipulating the ions. First a description of the cryostat is provided, then the surrounding vacuum system is discussed.

4.1.1 *Cryostat*

For cryogenic cooling, a flow cryostat is used which operates by evaporating a liquid cryogen that provides cooling power. Its main advantage is the lack of any moving parts in contrast to for example pulse tube or Gifford-McMahon cryo coolers, and thus the absence of any moving valves or switching magnetic fields that may introduce noise into the system. While the cryostat does not vibrate at any specific frequencies, the boiling of liquid cryogen inside the cold-finger still produces movement. These vibrations do have a detrimental effect on the phase stability between the ions and an applied laser beam. For this reason the cold-finger is decoupled by flexible braided copper strands thermally connecting the experimental section of the apparatus with the cold-finger. Fig. 4.1 illustrates the cryostat system: Liquid cryogen is supplied by a storage Dewar which is connected through an insulated transfer line to the cold-finger. The natural boil off in

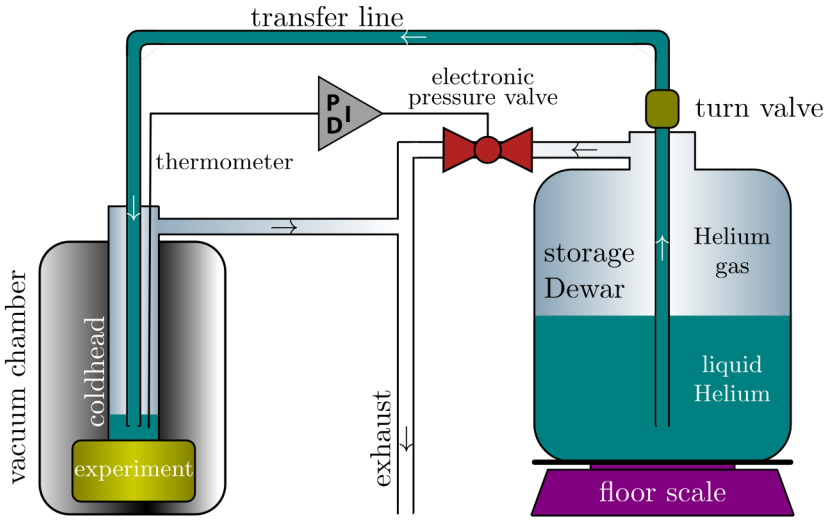

Figure 4.1: SCHEMATIC OF THE CRYOSTAT SYSTEM. The pressure in the Dewar pushes the cryogen through the transfer line into the coldhead of the cryostat. A temperature probe connected to a proportional integral derivative (PID) controller controls an electronic pressure valve to regulate the Dewar pressure.

the Dewar produces a positive pressure, pushing cryogen through the transfer line into the cryostat. The flow of cryogen is roughly regulated by a turning valve on the lance. Both liquid nitrogen (LN) and liquid helium (LHe) can be used as cryogens. To keep the flow of cryogen stable, a pressure regulator limits the pressure of the Dewar. A fixed regulator is used for nitrogen while an electrically adjustable regulator is used for helium. The adjustable regulator is set from the control computer by a slow PID, in order to keep the temperature constant. When operating using nitrogen the exhaust gas is piped out of the laboratory. When LHe is used, the gaseous helium is instead fed to a recovery facility in the basement, where it is captured in a balloon and then compressed into high-pressure gas bottles to be later re-liquefied by the on-site helium liquefier.

The temperature profile for a typical cooldown is shown in Fig. 4.2: To limit the consumption of LHe, the setup is precooled with LN when starting from room temperature. Once the setup is thermalized at liquid nitrogen temperatures, in this example after 24h, the cryostat is switched to liquid helium. The process typically takes 2 days.

During regular operations the temperature of the coldfinger is kept at 15K in order to maintain a practical usage of cryogens using $0.68(7)\,\mathrm{L\,h^{-1}}$ of LHe. Under these conditions the Dewar needs to be refilled approximately every two weeks. The temperature can be pushed lower at the expense of efficiency, as the gas that exits the cryostat under these circumstances is still cold. This leads to visible ice formation around the exhaust lines from freezing water vapours in the air. The 15K operating temperature is sufficient to reach an

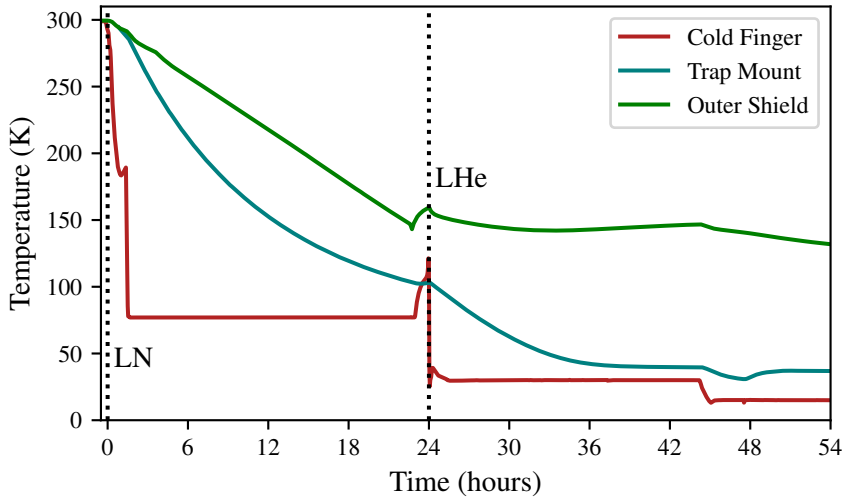

Figure 4.2: TEMPERATURE OVER TIME OF THE CRYOSTAT DURING A COOL-DOWN FROM ROOM TEMPERATURE: Initially liquid nitrogen is used to pre-cool the setup from room temperature. Once the temperature of the trap mount is low enough, the cryostat is switched to liquid helium. An initial rise of the cold finger temperature while switching between cryogens stems from gaseous helium flowing through the cryostat as initially the liquid evaporates still inside the transfer line until it is sufficiently cooled.

inner shield temperature of approximately 35K, at which point the single-ion lifetimes increase from minutes to timescales longer than we were typically measuring ($>$ 8h).

4.1.2 *Mechanical Assembly*

The cutaway render of the setup in Fig. 4.3 shows the vacuum chamber. It consists of an upper utility section and a lower octagon that houses the experimental section. The utility section includes the DC feedthroughs for the trap electrodes. Two ion pumps and two non-evaporable getters (NEGs) are installed here. Auxiliary equipment such as a venting valve, a pressure gauge, an angle valve for the turbo-molecular pump which is used for initial evacuation of the chamber, and the feedthroughs for heaters and for the temperature probes are all mounted in this section.

Inside the chamber, this section houses the mid shield which contains the DC filters for the electrodes, as well as the vibration isolation and thermal connection between the cold head and the experimental section. The outer thermal shield is mounted to the mid shield. Its primary purpose is to reduce the thermal conductivity by black-body radiation. Inside the outer shield, a the steel tube is attached below the mid shield which mechanically supports the inner shield. This

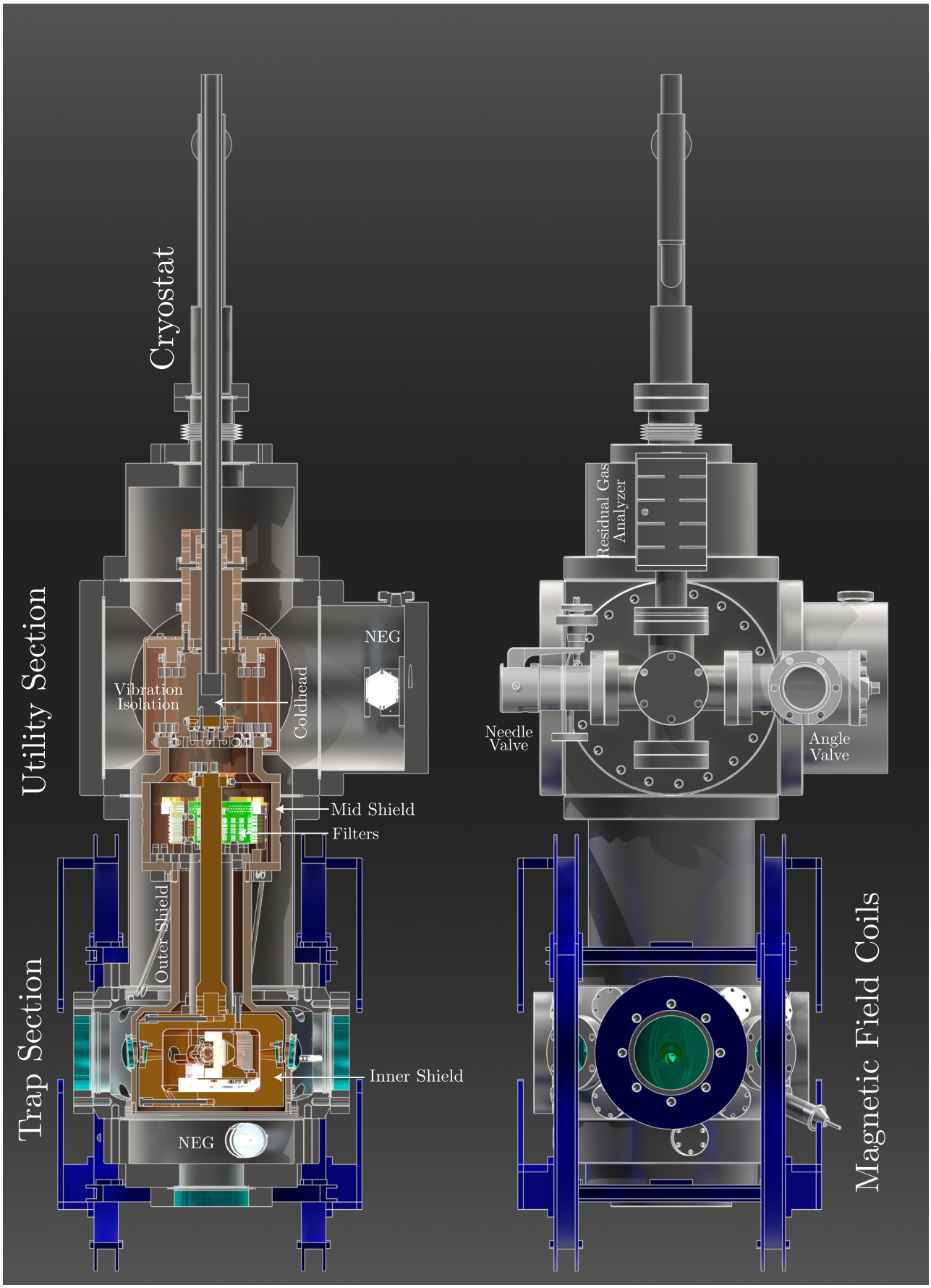

Figure 4.3: Cutaway view of the vacuum chamber on the left, with the external view on the right.

tube houses the copper rod that thermally links the vibration isolation stages from the cold head to the inner shield.

The inner shield houses the trap assembly, which consists of a base plate housing the resonator (see Section 4.2.2). On this plate the in-vacuum optics (Section 4.6) are mounted and aligned with respect to the trap mount (Section 4.2.1) on which the actual trap is installed.

The shields have windows aligned with the 8 viewports of the octagon, giving optical access at increments of 45° in a plane perpendicular to the surface of the trap.

The ovens that produce the neutral atom beams are mounted on the room-temperature octagon due to the energy dissipated while actively running the oven, which could lead to thermal expansion of the apparatus if it was mounted on the cold stage. This would in turn cause a misalignment of the beams after loading. The beam of neutral atoms passes through a hole in both shields and enters the trapping region through the central slot of the trap. The outer shield is equipped with a shutter to block the atom beam. The shutter protects the trap while initially melting the indium seals of the ovens and when establishing the relation between atom flux and oven current.

The whole vacuum chamber assembly is mounted on a floated optical table for vibration isolation. The optical table has two layers, where the chamber is placed in a cutout of the upper optical table such that the center of the view ports lines up with the beam height of the optics on the upper layer.

4.2 ELECTRONICS

In the following section, the electrical components of the vacuum chamber assembly will be discussed. This is followed by a description of the driving electronics for controlling the experiment.

4.2.1 *Trap Mount*

For ease of handling, the trap is glued and wire-bonded to a PCB. This interposer PCB routs all the connections for the electrodes from the landing pads of the wirebonds to pads on the backside of the interposer. Fig. 4.4 shows the packaged and bonded trap while in the cleanroom. The PCB is then inserted and mechanically clamped to a socket.

The socket[1] itself contains so-called fuzz buttons, which are small gold springs. These springs get compressed by the inserted interposer, providing electrical contact between the pads of the interposer and the matching pads of the breakout PCB on which the socket is placed as can be seen in Fig. 4.5 showing a cross-section of the stack. The socket and breakout PCB are mounted to the copper mounting bracket

1 Custom Interconnects

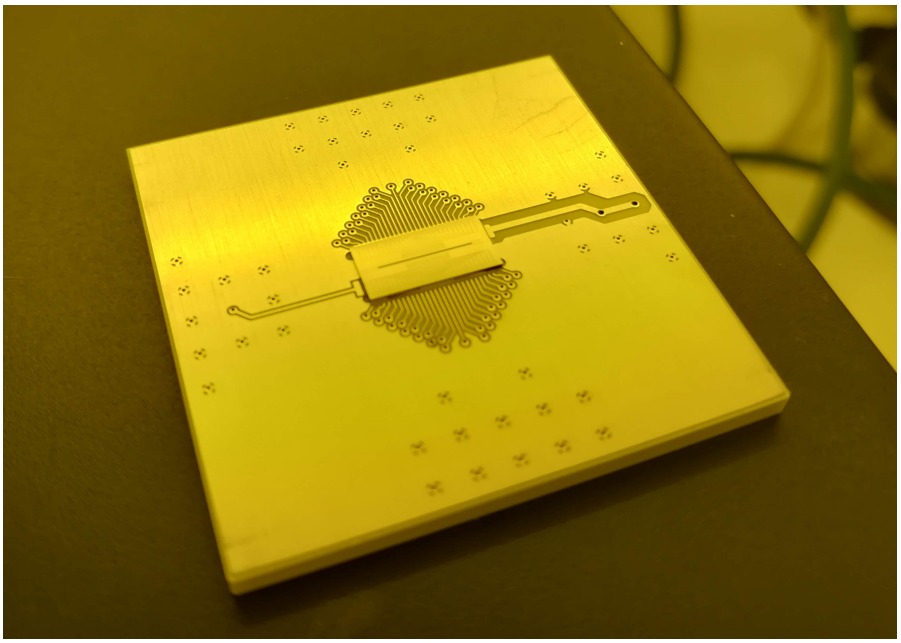

Figure 4.4: PACKAGED TRAP GLUED AND WIRE-BONDED ON INTERPOSER PCB: The separated lead for the RF is visible on the right side, with the center electrode connected from the left side. The traces for the segments are fanned out symmetrically at the top and bottom edge of the trap.

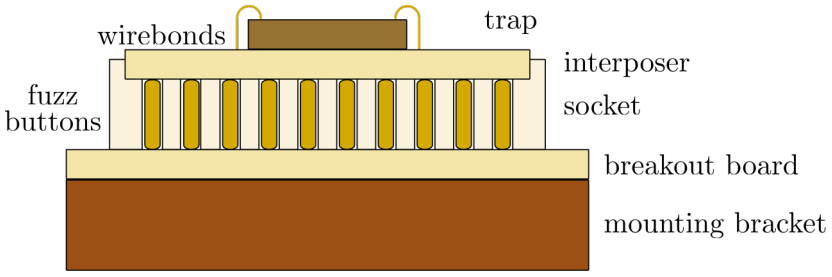

Figure 4.5: SCHEMATIC CROSS-SECTION OF THE STACK FOR THE TRAP MOUNTING. Wirebonds along the edge of the trap connect to the interposer. The fuzz buttons provide electrical connectivity between the breakout board and the interposer.

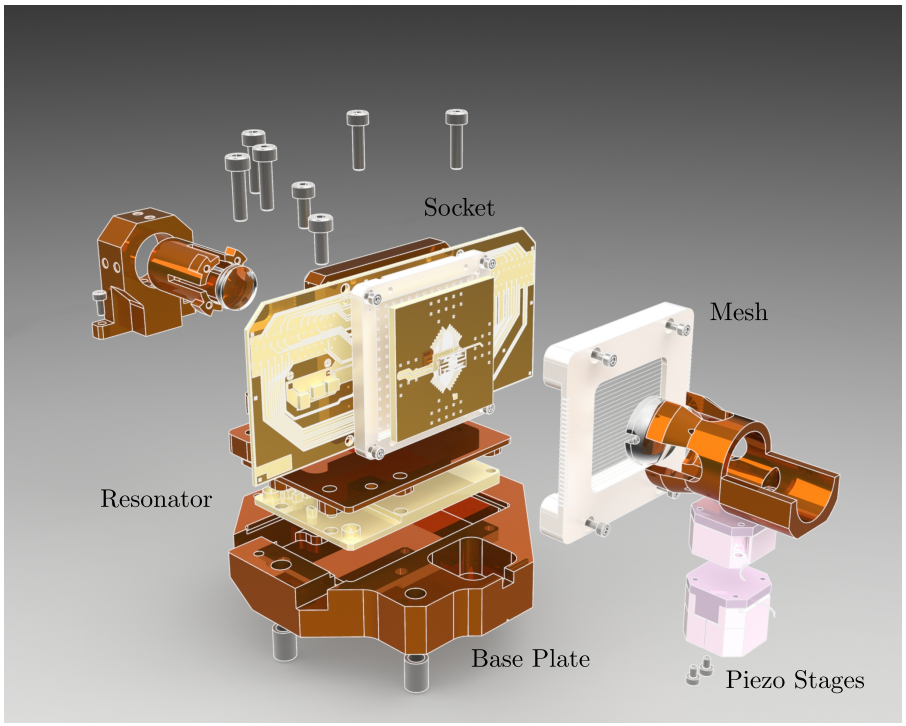

Figure 4.6: COMPONENT VIEW OF THE TRAP MOUNT. The packaged trap is fixed vertically in the socket, which is in turn held by the mounting bracket. The resonator is installed inside the base plate, on top of which the optics and the bracket are attached.

as shown in Fig. 4.6. This bracket provides mechanical support for the assembly and aids as a thermal conductor to thermalize the trap with the inner shield, as RF dissipation in the trap is the largest source of heat inside the experimental section.

In previous iterations of the setup, the electrical connections were routed from the trap to the feedthroughs via twisted wire pairs made of phosphor bronze. Given the increased number of connections desired for operating the new trap, the twisted-pair solution was impractical for the current iteration. The expected thermal loads and resistances for some common wire materials used in cryogentic applications are tabulated in Table 4.1. The size of the combined cross-section to physically mount in the system, the increased thermal load of the wires, and the challenge of tracking the connectivity of the wire pairs during assembly made the previous method non-viable. Instead, wire harnesses made of polyether ether ketone (PEEK) with 24 manganin cable strands each were utilized, offering a more compact solution. As 80 control channels were available to generate DC voltages (see Sec. 4.2.4), 4 wire harnesses were used, where from each 20 connections (Resistance $\approx 19\Omega\,\mathrm{m}^{-1}$ per connection) are connected to the DC control channels, while the remainder are designated as ground connection. The choice of manganin was made according to availability by the manufacturer; copper assemblies impose excessive

Table 4.1: Calculated heat load between stages and resistance per individual lead for possible wire materials: Twisted-pair options, wire harness designs and flex PCB traces are listed. Values for thermal and electrical conductivity taken from [92, 93]

	Size (µm)	Resistance $(\Omega\,\mathrm{m}^{-1})$		Heat load (mW)	
		$4-77\mathrm{K}$	$77-300\mathrm{K}$	$4-77\mathrm{K}$	$77-300\mathrm{K}$
Copper twisted pair	⌀202	0.011	0.14	4.4	6
Phosphor-Bronze twisted pair	⌀202	1.4	1.5	0.07	0.53
Copper loom	⌀90	0.06	0.72	0.87	1.2
Copper Flex PCB trace	12×50	0.6	7.6	0.08	0.1
Manganin loom	⌀110	18	19	0.02	0.1
Constantan loom	⌀110	22	22	0.02	0.1

heat load, while constantan is ferromagnetic, and assemblies made of phosphor-bronze were not available.

This arrangement simplifies assembly of the apparatus while increasing the available channels from 24 to 80, reducing the chance of assembly errors. The two photos in Fig. 4.7 display the wiring with the old and the new solution.

The breakout board was designed to be mounted with nano-D connectors, but due to difficulties in sourcing the appropriate connectors, the leads of the wire harnesses were hand-soldered instead. For the connections to the filterboard 25 pin micro-D connectors were used, while the feedthrough for the vacuum chamber consists of 4 DSub-25 connectors. The wire assemblies were first sourced from CMR-Direct with polyester insulation, which were later replaced by assemblies from Tekdata with polyimide insulation due to concerns over out-gassing of the insulation.

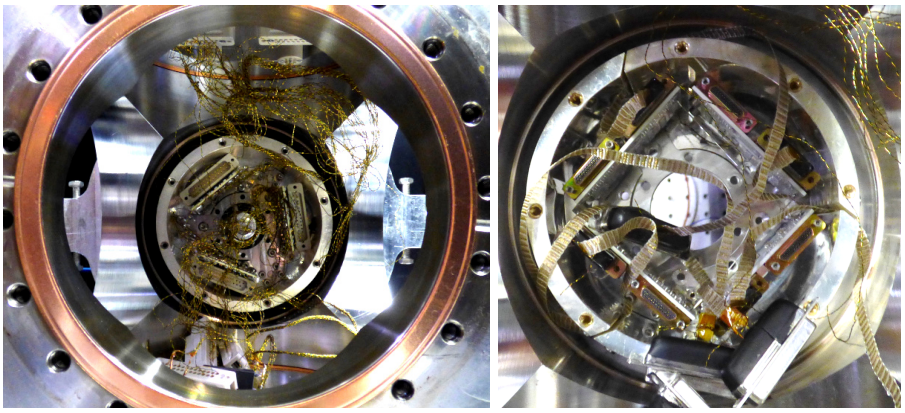

(a) Twisted-pair wiring (b) Loom-based wiring

Figure 4.7: Comparison of the old twisted pair wiring (a) compared to the new wire harness based DC connections shown in (b). The wire harnesses enable a reduction in individual connections that need to be completed while increasing the amount of available channels.

4.2.2 *Resonator*

To produce the necessary RF voltages for operating an ion trap, resonators are commonly employed to amplify the voltage of a RF source. External helical resonators are popular for room-temperature setups, but prove impractical for a cryogenic setup, as the required low-Ohmic connection to the trap necessarily imposes a large heat load. Such a resonator can be placed directly on the cold stage, but available space is at a premium while designing cryogenic systems. This makes compact RLC-resonators an attractive alternative for cryogenic setups [94], where an inductance is combined with the natural capacitance of the trap to form a resonator circuit.

Previously, in this setup different kinds of compact coils were investigated to form a resonator with the capacitance of the trap device [95]. While a coil made from high-temperature superconductor showed the best performance in terms of quality factor and thus voltage amplification, this coil experienced a critical failure under repeated temperature cycles. Thus a more conventional wire coil was utilized to ensure more reliable trap operation. To fabricate the wire coil of the RLC resonator, a core made of substrate commonly used for creating PCBs is used[2] with equally spaced holes drilled at two radii. A silver plated copper wire is then manually threaded through the holes, forming a coil. A single separate loop of wire is additionally included in the coil to function as an inductive pickup. Fig. 4.8 shows how the coil is housed together with an impedance matching circuit inside the base plate below the trap mount, where it is connected to the trap

2 Rogers 4350B

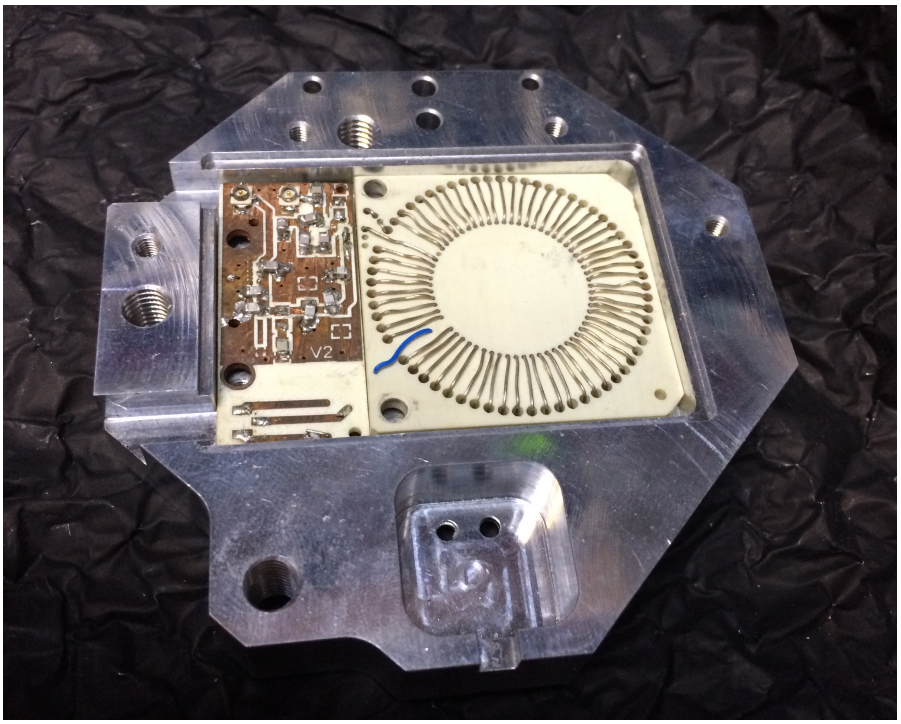

Figure 4.8: Wire coil wound through a PCB core housed inside the base plate. The smaller PCB on the left allows mounting of the capacitors for impedance matching.

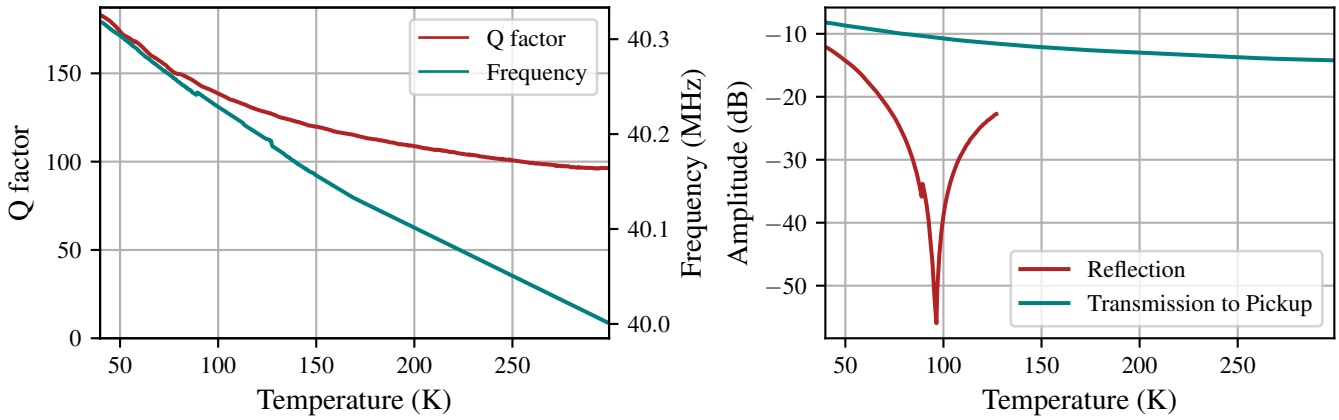

Figure 4.9: The quality factor and resonance frequency of the resonator are shown in the left graphic, while on the right the back reflection and the transmission to the pickup are shown versus its temperature.

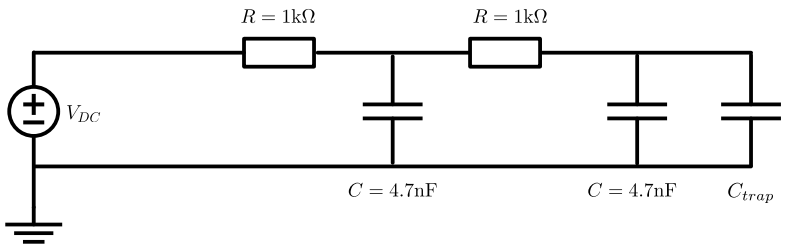

Figure 4.10: Schematic of the filters between the voltage source V_{DC} and the DC segments of the trap with a cutoff frequency of 34kHz.

PCB. The matching circuit is required as the resonator is driven by a transmission line with an impedance of 50Ω, but an RLC resonator on resonance has a low impedance, which would lead to almost all power being reflected back. By matching the impedance the back-reflection can be minimized. The left plot of Fig. 4.9 shows how the quality factor of the coil increases with lower temperatures as the resistance of the coil decreases, accompanied by a shift in resonance frequency. The right plot displays how the impedance matching of the resonator changes with the temperature of the inner shield as the matching is also sensitive to the resistance of the coil and matching circuit.

An in-house RF stabilization unit is used to keep the RF voltage level stable [90]. The device works by measuring the voltage at the pickup coil of the resonator and using it as the input for the PID controller regulating a voltage controlled attenuator inserted between direct digital synthesis (DDS) frequency source generating the trap frequency and the amplifier.

4.2.3 *DC Filters*

The DC filters are designed to prevent noise from either the voltage source or picked up by the cables from reaching the trap electrodes where it will affect the ions. The DC filters for a segmented surface trap are a trade-off between filtering high-frequency noise that causes heating of the motional modes, which in turn limits the fidelity of quantum gates, and the requirement to have sufficiently high cutoff frequency to change the applied voltages quickly to perform shuttling operations. A cutoff frequency of 34kHz was selected.

We chose 2nd order RC filters for the task, the circuit of which is shown in Fig. 4.10. Besides filtering, the second capacitor of the network also accomplishes the task of a shunt, diverting the RF picked up via capacitive coupling between the RF and the DC electrodes to ground. The filters were manufactured from Rogers 4350B PCB substrate, with a gold finish, and fitted with ceramic capacitors[3] which have been shown to have low temperature dependence [96]. The choice

3 C0G/NP0 ceramic capacitor

of RC filters was motivated to avoid a feature of the LC filters used previously, which included resonances in their frequency-response profile around their nominal cutoff frequency. These resonances do additionally distort higher-frequency components of time dependent waveforms, making it more difficult to compensate during shuttling operations [97].

A consideration when using resistors in a filter circuit is the generated Johnson–Nyquist noise. We can estimate the expected heating rate Γ from the electric field noise spectral density $S_E(\omega)$ [65].

$$\Gamma \approx \frac{e^2}{4m\hbar\omega} S_E(\omega) \tag{4.1}$$

where m is the mass of the ion species and ω is the frequency of the motional mode of the trap.

The noise spectral density can in turn be estimated from the voltage noise $R(\omega)$

$$S_E(\omega) = 4k_B T \frac{R(\omega)}{D^2}. \tag{4.2}$$

The frequency-dependent voltage noise $R(\omega)$ is simulated using a SPICE simulation of the filter network, while the characteristic distance D can be inferred from a simulation of the trapping fields. For a $^{40}Ca^{+}$ion at a trap frequency $\omega = 2\Pi \cdot 1\text{MHz}$ we estimate a heating rate of $\Gamma_{Ca} < 0.1\text{ph}\,\text{s}^{-1}$ on the axial mode due to Johnson noise for an electric field noise of $4 \cdot 10^{-16}\text{V}^2\,\text{m}^{-2}\,\text{Hz}^{-1}$ (See Fig. 4.11), and we thus do not expect the filters to limit the performance.

External RC-filters with a cutoff frequency of 1 Hz can be added at the feedthroughs of the vacuum chamber for applications that do not require shuttling to provide better suppression of any technical noise originating from the voltage source.

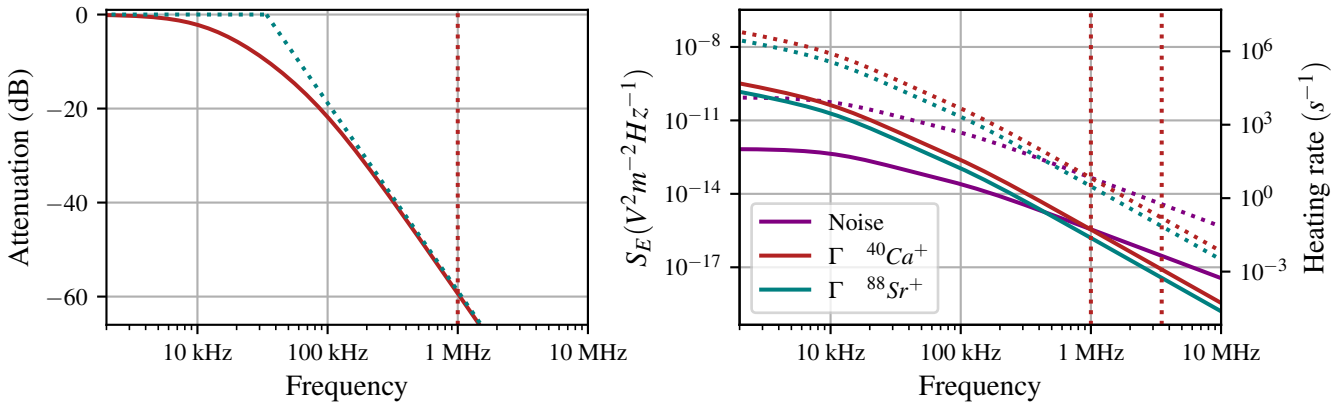

Figure 4.11: CALCULATED FILTER RESPONSE (LEFT) AND EXPECTED FIELD NOISE AND HEATING RATE DUE TO JOHNSON NOISE (RIGHT). The solid lines correspond to the largest contribution to the axial heating rate, while the dashed lines give the largest influence in the radial direction. The vertical lines mark the expected trap frequencies of 1MHz axial and 3.5MHz radial.

4.2.4 *Control System*

To perform quantum operations the frequency and amplitude of various laser pulses as well as the voltages of the trapping potentials need to be controlled on the timescale of microseconds. In the following we will give an overview over the system used in this experimental setup.

For controlling frequency, amplitude and phase of laser pulses works we generate RF pulses, which are the transferred onto the light. For this the device of choice is the acousto-optic modulator (AOM), which imprints the properties of the RF pulses onto the laser.

Some channels need to be controlled synchronously with an experimental cycle, while for other channels asynchronous control is sufficient as they do not need to be updated during a single experiment.

Fig. 4.12 gives an overview of the components of the control system and how they are being connected: The core of the control system to produce these RF pulses is the *PulseBox* [99], a field programmable gate array (FPGA) that controls the timing, amplitude, frequency and phase of pulses produced by the 6 DDS frequency generator channels and the the timing of 32 transistor–transistor logic (TTL) channels. This device provides all the synchronous control channels utilized in the experiment.

The pulse generator is programmed by the Trapped Ion Control Software (TrICS) running on the control PC [100]. A software interface called trixit allows setting experimental parameters as well as scheduling and evaluating experiments from python code instead of

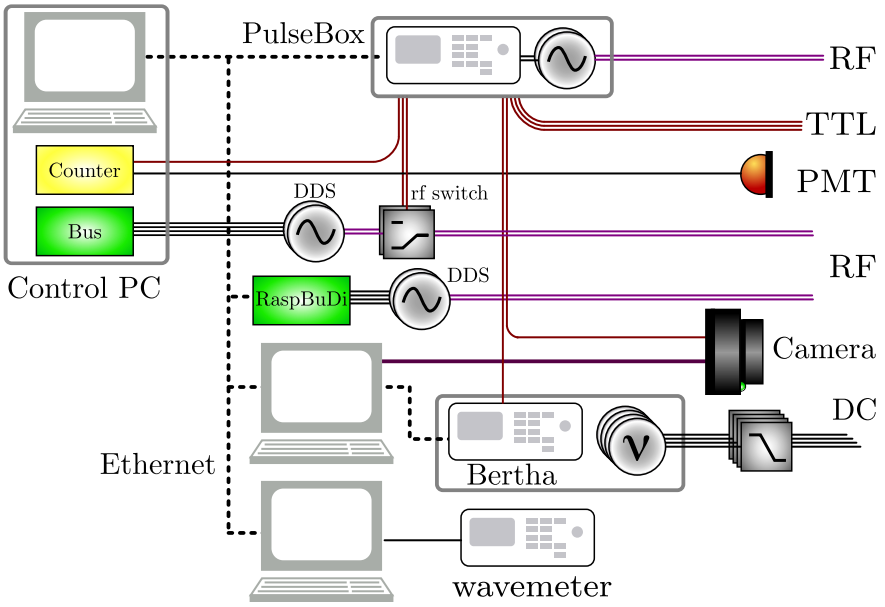

Figure 4.12: OVERVIEW OF THE EXPERIMENT CONTROL SYSTEM. The system allows for RF control as well as DC channels for trap voltage control. The bus system controls DDS frequency sources either via a output card in the computer or a raspberry pi. Ethernet communication is used for non-timing sensitive channels. The PulseBox is programmed by the control PC and controls the timing of RF and TTL channels. With the TTL channels PMT and camera are synchronized to perform measurements. Illustration made using [98].

the graphic user interface (GUI), which is a central feature in enabling the automation routine presented in Chapter 5.

For asynchronous frequency channels, DDSs are used that are programmed from TrICS and are switched via TTL if required. The commands for programming the DDS are sent via a parallel bus system [101], either driven by a NIDAQ card, or a raspberry-pi based bus controller (See Appendix D). The RF switches[4] are controlled by the TTL signals, and allow to enable and disable these channels synchronized to the experiment.

The control software also can send commands to secondary control programs, such as the controllers for the camera, the trap voltage supply, and the wavemeter locks (see Appendix D). The control PC also runs software to control the ovens and to program the cryostat as discussed in Section 4.1.1.

To control the voltages applied to the electrode segments of the trap, we utilize a custom FPGA-based arbitrary waveform generator developed by collaborators in Mainz [102, 103]. The system named Bertha supports 80 digital-to-analog converter (DAC) channels with an output range of ± 40V and a resolution of ≈ 1.2mV. The system can

4 Mini-Circuits ZASWA-2-50DR+

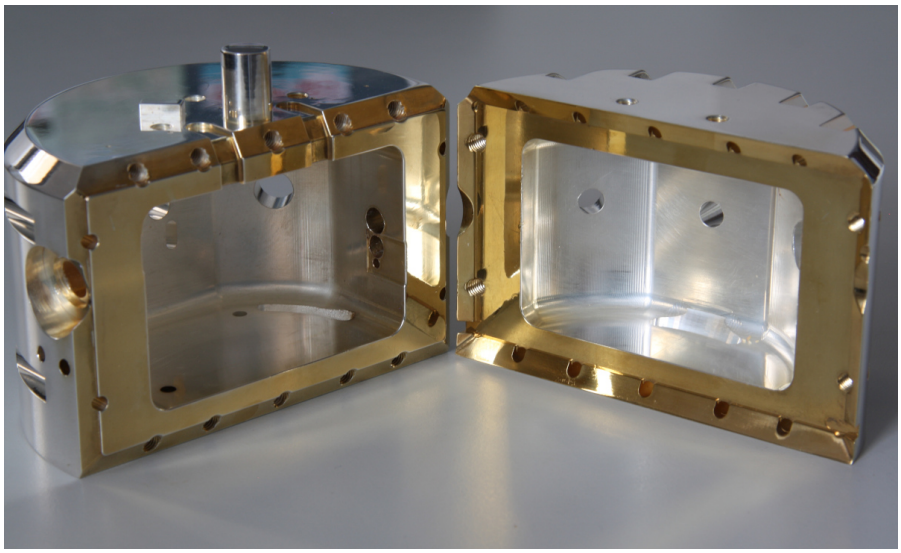

Figure 4.13: INNER SHIELD AFTER SILVER-PLATING AND BEFORE INSTALLATION. The contact surfaces were gold plated to maximize conductivity across the interface. Visible at the top rim of the left half shell are the two slots for passing through the ribbon cable assemblies.

run at a maximum sample rate of 2.5 MSamples/s The voltage ramps are programmed via ethernet, and are then synchronized to the pulse generator via a TTL channel.

For measurements a PMT and an electron multiplying charge-coupled device (EMCCD) camera[5] are available. The camera is synchronized via TTL and read out via CameraLink from a PC, while the PMT data is collected by a counter card[6] connected to the control PC.

4.3 MAGNETIC FIELD

To operate a quantum processor a magnetic field is required to spatially define the quantization axis and split the Zeeman sublevels in frequency such that they can be individually addressed. A field of $\approx 3.5\,\mathrm{G}$ is targeted, leading to a splitting of the $S_{1/2}$ states by about 10 MHz while neighboring $D_{5/2}$ sublevels are split by about 6 MHz. To this end, we utilize a pair of Helmholtz coils driven by a stable current supply[7] to generate this field. Initially we used a pair of coils producing $11\,\mathrm{G\,A^{-1}}$, but we found that the high inductance ($\approx 46\,\mathrm{mH}$) made the current difficult to stabilize, and we switched instead to a coil pair ($\approx 1\,\mathrm{mH}$) that was initially intended to compensate the gradient. It generates only $0.6\,\mathrm{G\,A^{-1}}$, so a much higher current of 6 A is required to produce the same field, but the relative stability of

5 Andor iXon Ultra 897
6 National Instruments NI-6733
7 Keithley 2280S Programmable DC Power Supply

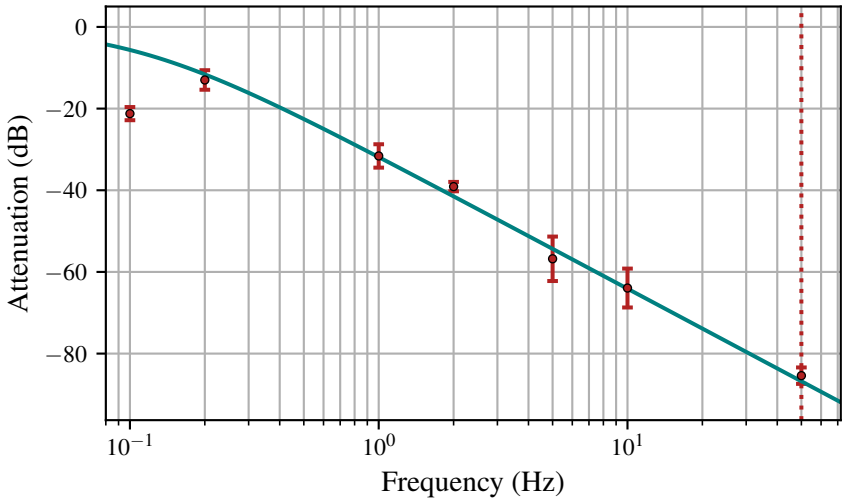

Figure 4.14: MAGNETIC FIELD SUPPRESSION OF THE INNER SHIELD AS FUNCTION OF FREQUENCY. For sub-Hz frequencies the effect vanishes, while at the mains frequency of 50Hz a suppression of $\approx$ 75dB is achieved. The fit has a slope of 32(1) dB/dec. The first data point is omitted from the fit as the frequency is so low that during the measurement the noise is not sufficiently averaged over all phases, leading to an overestimate of the field attenuation.

the current was improved, which resulted in an improvement of the observed coherence times.

4.3.1 *Magnetic Field Shielding*

Noise from current fluctuations in the bias coils as well as stray magnetic fields adversely affect the coherence of the qubits. Of particular importance is the 50Hz noise generated by the alternating current (AC) mains that powers all the laboratory equipment. To suppress this noise, we utilize a copper shield enclosing the trap assembly with a wall thickness of $> 20\,\mathrm{mm}$. The shield can be seen in Fig. 4.13 before installation. The skin effect significantly attenuates alternating magnetic fields passing through a conductor once the thickness exceeds the skin depth [90].

We measure the magnetic field suppression by intentionally applying an AC current of varying strength and frequency to a separate coil next to the vacuum chamber. The field created by the additional coil is aligned with the direction of the bias field. It is the most sensitive direction as we are primarily sensitive to changes in the field magnitude rather then its direction. For small noise amplitudes the effect of fields perpendicular to the bias field the change is quadratically suppressed compared to fields aligned with the bias field.

We then observe the decay of the Ramsey fringe contrast (Eq. (3.39)) for a given noise environment. The measured Ramsey contrast can be fitted with a combination of a reference decay without any intentionally applied noise, and a contribution from the induced fluctuations at a fixed frequency. As both the sensitivity of the transition to magnetic fields and the field generated by the coils are known, one can calculate the suppression ratio between externally applied magnetic field and the field measured at the ion The results are plotted in Fig. 4.14 where we find a suppression exceeding 70dB at the crucial 50 Hz frequency.

Note that besides attenuating magnetic fields this shield also acts as a shield for the purpose of limiting thermal radiation transfer.

4.3.2 *Stabilization System*

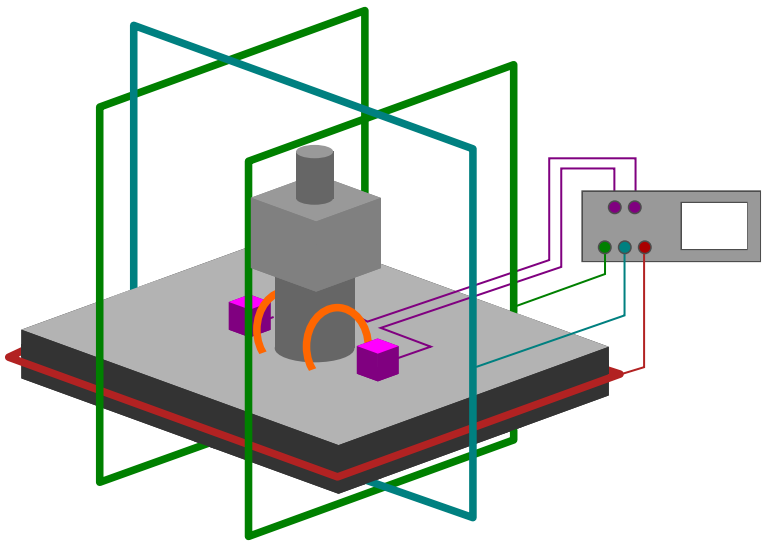

Figure 4.15: INSTALLATION OF STABILIZATION SYSTEM: The two sensors are placed on either side of the vacuum chamber. Three sets of coils are installed around the optical table. A double loop (green) in Helmholtz configuration was used in the direction aligned with the bias field generated by the Helmoholtz coils (orange), as noise along this direction has the largest influence on coherence. The single loops (blue, red) compensate in the other two axes.

As the effectiveness of the inner shield drops for low frequencies, slow magnetic field fluctuations still affect the ions on a shot-to-shot basis. Effectively during each individual measurement the ions will experience a different detuning from the transition frequency. These shot-to-shot detunings can be compensated in spin-echo sequences, but it would be still preferable to eliminate rather than compensate the noise. To this end we installed a commercial magnetic field canceling

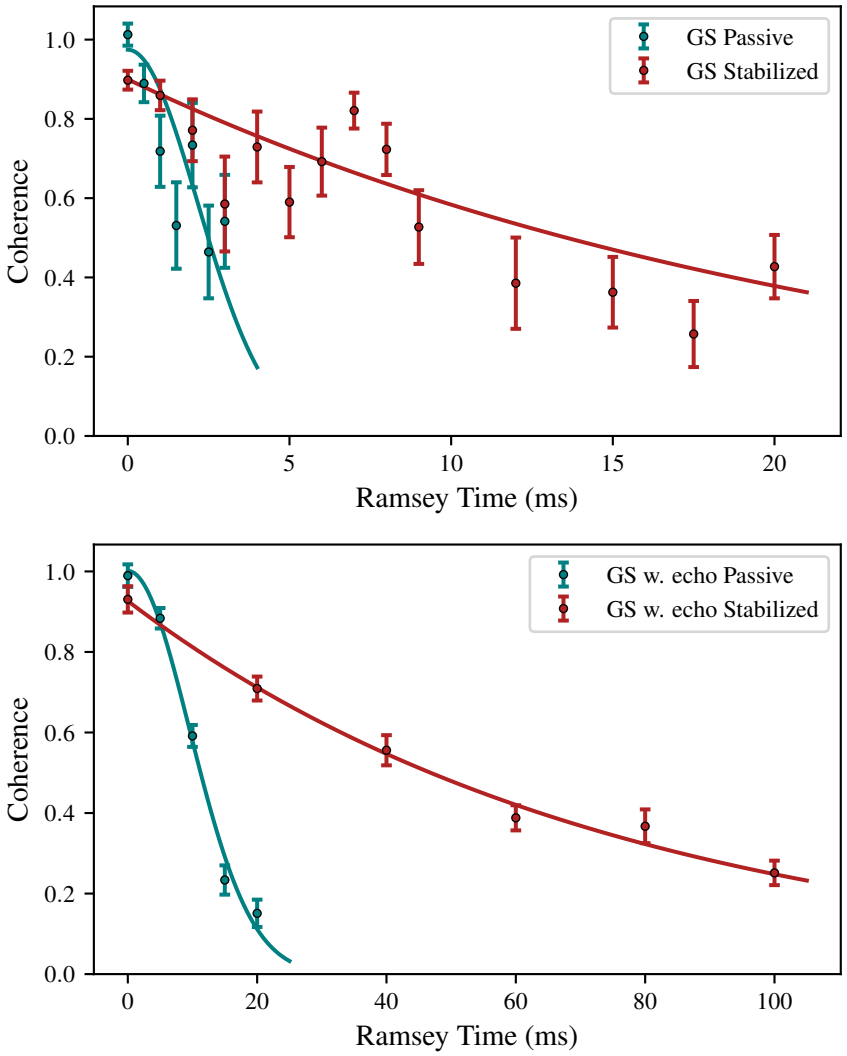

Figure 4.16: Coherence times with and without the magnetic field compensation system measured between the Zeeman states $|4^2S_{1/2}, m_j = -1/2\rangle \leftrightarrow |4^2S_{1/2}, m_j = 1/2\rangle$. For both Ramsey and Spin-Echo experiments the coherence time is increased by the stabilization system, from 3.0(5) ms to 23(4) ms and from 13.5(6) ms to 76(4) ms respectively. The reduced initial contrast for the stabilized measurements is attributed to imperfect calibration of the transfer π pulses.

system[8] around the experimental apparatus. The system uses two magnetic field sensors placed on the optical table on either side of the vacuum chamber to measure the magnetic field. The PID in the control unit then uses the sensor readings to control the current in compensation coils, consisting of large cable loops around the entire optical table, each aligned with a different axis. For the geometry of the compensation coils see Fig. 4.15.

The effect of the magnetic field cancellation system can be seen in an improvement of the coherence times on the ground state qubit show in Fig. 4.16, where we observe an increase of the ground state coherence time from 3.0(5) ms to 23(4) ms without a spin echo pulse, while with the addition of a spin echo the coherence time increases from 13.5(6) ms to 76(4) ms. The passive measurements were best fitted by a Gaussian, while the stabilized data was better modeled with an exponential, which points to a different shape of the distribution of fluctuations (See Section 3.5.2).

While the improvement of the coherence times demonstrates the utility of the field cancellation system, the observation that the addition of a spin echo pulse to cancel static frequency offsets still has a significant effect indicates that slow fluctuations are still present even with the cancellation system being active, likely due to the sensors not being at the same position as the ions.

4.4 QUADRUPOLE LASER SETUP

As described in Chapter 3 we can utilize light to control the quantum state of the ions as well as their coupling to motional states, necessitating light sources with the appropriate frequencies and line-widths. Diode lasers are highly popular as a source of light for this task in quantum optics applications as they require a small footprint, are comparatively affordable, and are also highly efficient, such that they can typically operate without the complexity of additional cooling systems such as water-cooling. For both ion species $^{40}Ca^{+}$ and $^{88}Sr^{+}$ discussed in this thesis diodes are available at all relevant wavelengths for quantum information processing. In particular the external cavity diode laser (ECDL) design has proven itself as a reliable option to provide light to drive dipole transitions, offering sub-Megahertz linewidths while free running, while also being tuneable to match the targeted transitions.

The requirements on lasers driving the quadrupole transition are more stringent than those affecting the dipole transitions due to the different task these transitions are used for. For an optically encoded qubit the relative stability of the frequency of the laser and the atomic transition directly affects the performance of the qubit [104]. Ideally the linewidth of the laser is smaller than the inverse of the upper state

8 Spicer Consulting SC24 Magnetic Field Canceling System

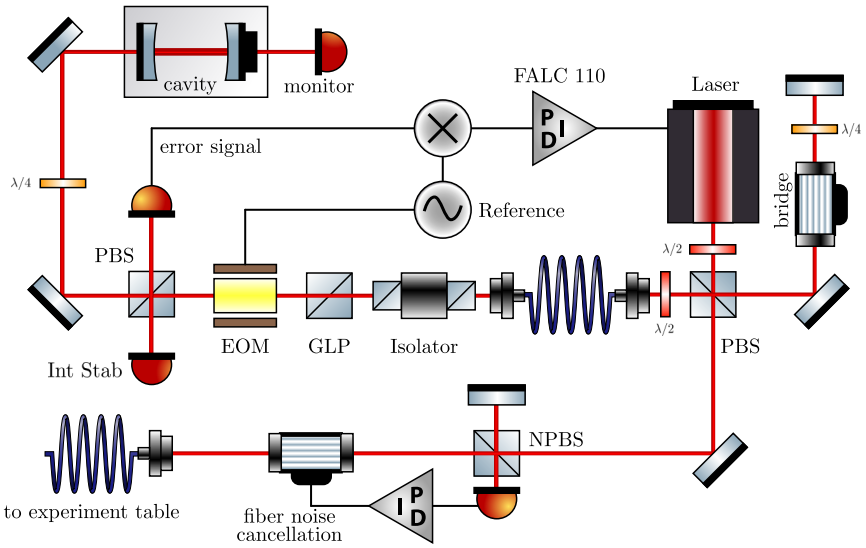

Figure 4.17: Layout of the optical setup of the Quadrupole Laser inside the shielding box. Two identical setups are housed inside the box, one each for a 729 nm and for a 674 nm laser.

lifetime, such that the coherence of the qubits encoded in these states is not limited by the laser.

Ion trapping quantum information has an additional requirement on phase noise at frequencies offset from the carrier due to the nature of the implementation of entangling gates. As described in Section 3.5.4 the gates involve applying laser tones close to the motional sidebands, typically spaced at $\approx$ 1MHz. This causes any spectral components of the laser at the same distance away from the center frequency of the laser to become resonant with the carrier transition of the ions. As the coupling to the sidebands is lower than to the carrier by the Lamb-Dicke factor and the sidebands are driven off-resonantly, the effective coupling of these spectral components is increased compared to the strength of these components in the laser spectrum. This can turn into a significant source of errors for entangling gate operations. Coincidentally, many typical laser lock setups for diode lasers have a matching control bandwidth $\approx$ 1 MHz. This means that at this frequency, the phase lag of the feedback loop reaches 180°, and the intrinsic phase noise of the laser diode is no longer suppressed, or even worse, can be amplified by the servo loop [105, 106]. In the following a laser system is described designed to enable higher servo bandwidths to suppress this crucial source of errors.

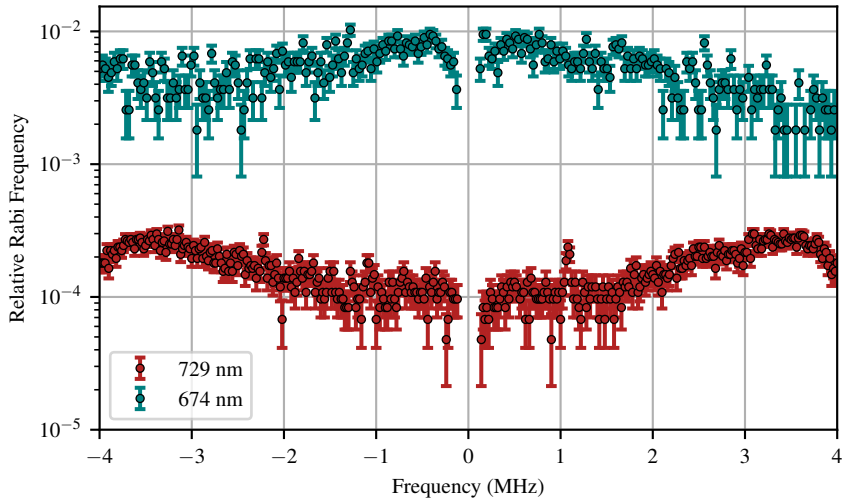

Figure 4.18: Power spectrum of the two quadrupole lasers measured on the ion. The excitation is measured relative to resonantly driving the Rabi frequency of the central carrier.

4.4.1 *Intracavity EOM ECDL*

The linewidth of the laser is stabilized by a Pound-Drever-Hall (PDH) lock [107, 108] to a high-finesse cavity from Stable Laser Systems[9]. The cavities are built around spherical ultra low expansion glass (ULE) spacers with a diameter of 50 mm to minimize the effects of drifts due to thermal expansion [109]. They have a finesse of $\mathcal{F} = 242742(6)$ [110] for 729 nm and $\mathcal{F} = 253200(600)$ for 674 nm (see Appendix C), respectively. The schema for locking is illustrated in Fig. 4.17 and works the following: The light is first split into a branch that is sent to be amplified for the experiment, and a branch to generate the feedback signal. The second branch passes a frequency-shifting AOM setup to bridge part of the frequency difference between ion resonance and the cavity mode. Subsequently, it is then sent through a clean-up fiber to reduce scattering into non-TEM00 modes of the cavity due to the non-perfect spatial mode profile of the diode laser and to decouple the alignment of laser and cavity. The light passes an optical isolator to prevent undesirable feedback caused by backreflections to the laser, followed by a Glan-Taylor laser polarizer (GLP)[10] to clean up the polarization. A polarizing beam splitter (PBS) is used to redirect part of the light to a photo diode for intensity stabilization, with the stabilization adjusting the power of the frequency-shifting bridge AOM. This intensity stabilization is necessary as it has been observed that the incident laser light ($\approx 20\,\mu W$) can cause frequency shifts on the

9 Stable Laser Systems
10 Thorlabs GL10-B

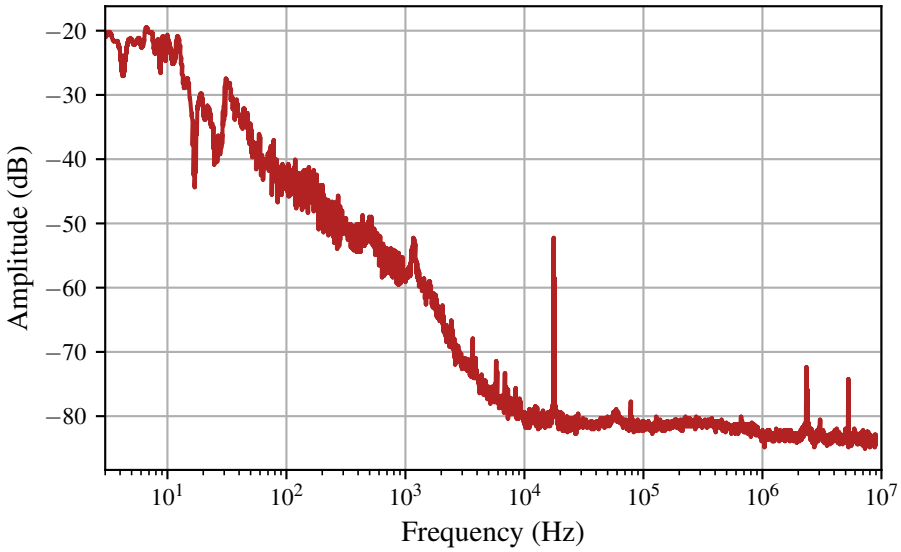

Figure 4.19: PHASE NOISE OF THE 729nm LASER. The noise is recorded by a beat note measurement with a narrow-linewidth 729nm TiSa laser [82] from the LinTrap experiment.

order of $\approx 100\,\mathrm{Hz}\,\mu\mathrm{W}^{-1}$ [111], and intensity fluctuations of the light in the locking branch can thus translate into frequency fluctuations.

An electro-optic modulator (EOM)[11] is then used to generate the sidebands for the PDH lock. To minimize the effect of residual amplitude modulation [112], the EOMs are temperature-stabilized[12] by a feedback loop controlling a Peltier element mounted to the side of the EOM. The modulated light is then coupled into the TEM_{00} mode of the cavity. The backreflection from the cavity is recorded by a fast photo diode, and then demodulated by mixing it with the reference frequency that was used for producing the sidebands, generating the frequency-dependent error signal characteristic of a PDH locking scheme [107, 113]. The phase of the reference signal sent to the mixer is adjusted by the choice of cable length to maximize the contrast of the PDH signal.

The down-modulated error signal produced by the PDH is then fed to a fast PID controller[13], which produces both a fast and a slow feedback signal. The fast branch is applied to the intra-cavity EOM, while the slow branch is sent to the laser control unit affecting both the piezo-controlled grating and the current of the diode. The EOM provides a feedback element with a high response speed, enabling a bandwidth of approximately 3.5MHz for the 729nm laser, while the slow branch controlling the piezo can follow large drifts (The tuning coefficients are on the order of $1\,\mathrm{GHz}\,\mathrm{V}^{-1}$). With a much higher DC gain, it keeps the bias point of the fast branch close to 0.

11 QUBIG PM7-NIR_18F
12 Thorlabs TED200C
13 Toptica FALC 110

The narrow-linewidth light in the branch directed to the experiment is amplified by a tapered amplifier (TA)[14] before it is sent to the switching setup. The output power of the TA is stabilized using a photo diode, with a controller[15] feeding back onto the current of the TA.

The setups for Calcium and Strontium are in principle identical, except for additional beam shaping optics at the output of the 674nm laser to reduce the ellipticity of the laser output mode. However despite the similarities of the setup, the performance of the lasers significantly diverges as can be seen in Fig. 4.18, where the spectral components of the laser were recorded by measuring the excitation probability of a single ion relative to the strength of the carrier coupling. The off-resonant components of the 729 nm laser are lower than those of the off-resonant components of the 674 nm laser by more than an order of magnitude. We attribute this to the response of the laser diode itself by process of exclusion, as the natural cavity linewidths are comparable, their mechanical construction identical, and swapping of the locking electronics between the two setups had no effect on the performance.

To provide a reliable long-term frequency reference the cavities need to be shielded from external influences. To achieve this, they are temperature stabilized and mounted in vacuum chambers. As set-temperatures the zero-crossing temperature (ZCT) is chosen, corresponding to $-0.6\,^{\circ}\mathrm{C}$ for the 729nm cavity and $-2.5\,^{\circ}\mathrm{C}$ for the 674nm cavity (See Appendix C). The entire setup is installed on active vibration isolation stages[16], which are then installed in a box, including further active temperature stabilization of the interior of the box and passive acoustic shielding. A detailed description of the box can be found in [114]. The temperature of the cavities is stabilized by a PID[17] controlling a Peltier element each. As we found residual frequency drifts of the cavity relative to the ion transition frequency that were correlated to the temperature of the box, additionally the temperature of the box itself was stabilized. This was accomplished by implementing a feedback on the water chiller[18] of the box via a PID running on a Raspberry Pi. This controller adjusts the set point of the chiller dependent on the temperature measurement inside the box. This leaves the transition frequency with a residual drift of $\approx 100\,\mathrm{mHz\,s^{-1}}$ due to ageing of the cavity.

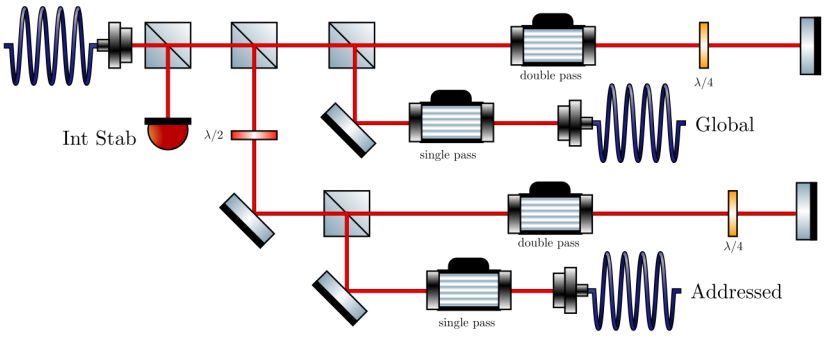

Figure 4.20: QUADRUPOLE LASER SWITCHING SETUP. The intensity stabilization photo diode feeds back on the current of the TA. The double pass AOMs operate at 250MHz while the single pass AOMs are driven at 80MHz

4.4.2 *Laser Switching Setup*

The narrow bandwidth light is sent through a fiber to the experimental setup. As environmental noise tends to induce phase fluctuations on a kHz scale in long fibers, a fiber noise cancellation setup is used to suppress this effect [115]. The light is then amplified using a tapered amplifier[19], and the sent to a switching setup depicted in Fig. 4.20: Here the light is split into two lines, each with a double-pass AOM[20] and a single-pass AOM[21] in sequence. The double-pass AOM diffracts light with acceptable efficiency over a wide range of frequencies, enabling to access all quadrupole transitions, while multiple RF tones can be applied to the single-pass AOM simultaneously, producing multiple laser tones required for implementing Mølmer-Sørensen entangling gates.

4.4.3 *Coherence time of the optical qubit*

The goal would be to have a laser sufficiently narrow such that the coherence of the qubits is entirely given by the natural linewidth of the qubit transition, which in the case of Calcium corresponds to 136 mHz.

The performance of the laser can be evaluated using a Ramsey experiment. For $^{40}Ca^{+}$we measure a $T_2 = 19.2(13)$ ms extracted from the decay shown in Fig. 4.21. We can extract an upper bound on the laser linewidth by assuming it is entirely limited by laser noise using Eq. (3.43), resulting in a linewidth of $\delta\nu_{729} = \frac{1}{\pi T_2} = 16.6(4)$ Hz.

14 Toptica BoosTA
15 Stanford Research Systems SIM960
16 Halcyonics Micro-60
17 Stanford Research Systems PTC10
18 Coherent T225P
19 Toptica BoosTA
20 Brimrose TEM-270-65-729/TEM-270-65-674
21 Brimrose TEM-80-10-729/TEM-80-10-674

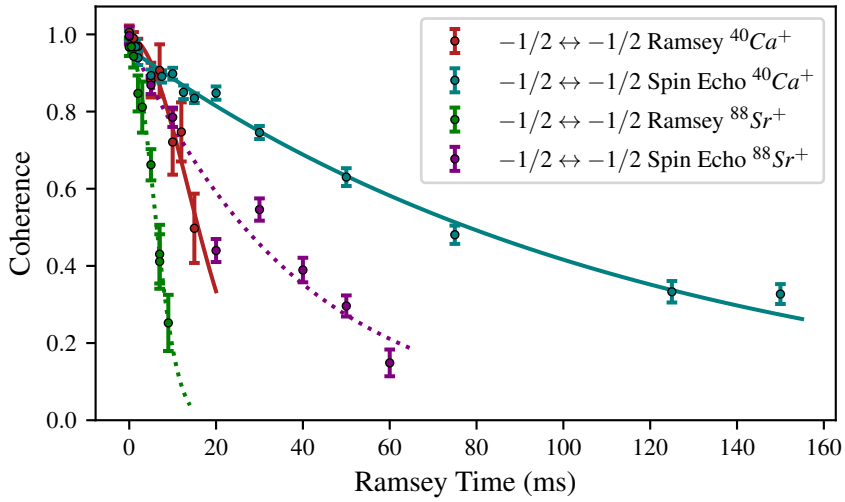

Figure 4.21: Coherence times of the 729nm and 674nm ECDL with and without spin echo measured on the $|4^2S_{1/2}, m_j = -1/2\rangle \leftrightarrow |3^2D_{5/2}, m_j = -1/2\rangle$ transition in $^{40}Ca^+$and on the $|5^2S_{1/2}, m_j = -1/2\rangle \leftrightarrow |4^2D_{5/2}, m_j = -1/2\rangle$ transition in $^{88}Sr^+$, respectively. The difference between Ramsey (19.2(13) ms) and Spin-Echo (119(7) ms) decay times for $^{40}Ca^+$indicates the presence of slow frequency fluctuations. For $^{88}Sr^+$a Ramsey time of (7.8(3) ms) and a Spin-Echo decay time of (38(5) ms) are extracted from fits.

This is consistent with a beat measurement with another 729nm laser shown in Fig. 4.19. A spin-echo sequence can be used to gain more information about the type of noise affecting the laser frequency. We measure $T_2^* = 119(7)$ ms where fluctuations slower than the probe duration are canceled. This kind of noise can be partially mitigated by decoupling techniques.

A similar analysis can be done for the 674nm laser for $^{88}Sr^+$(See Fig. 4.21). We find that $^{88}Sr^+$has significantly reduced coherence time of $T_2 = 7.8(3)$ ms compared to $^{40}Ca^+$, corresponding to a linewidth of $\delta\nu_{674} = 40.8(5)$ Hz for the 674nm laser. As the sensitivity of the two species to magnetic field noise is identical, we can conclude that the noise for $^{88}Sr^+$originates from the laser itself.

4.5 RAMAN LASER SETUP

For light-shift gates a pair of laser beams illuminating the ions in a Raman configuration are required. These are provided by a frequency-doubled titanium sapphire (Ti:Sa) laser system[22] which was set up by Benjamin Wilhelm in the course of his master's thesis (see [116]).

22 M Squared SolsTiS + ECD-X

The Ti:Sa is pumped by a Nd:YAG laser emitting at 1064 nm [23], which is then frequency-doubled to produce up to 18 W of output power at 532nm. After frequency-doubling the emission of the Ti:Sa with a nonlinear optical lithium-triborate crystal in a bow tie cavity the system can produce ≈ 1.2 W of optical power around 400 nm. A $\lambda/2$ waveplate and a Glan-Taylor laser polarizer (GLP)[24] allow for adjusting the power, with the unwanted light sent to a beam dump.

The beam is coupled into a fiber, transferring it to the experiment table. For the optical fiber both a high power photonic crystal fiber[25] and a regular polarization-maintaining fiber[26] were used.

On the experiment table the beam is split up into two branches. Each is individually controlled and switched by an 80 MHz AOM[27] and then coupled into a separate optical fiber, guiding the light to the upper table. Due to thermal effects the switching AOMs suffer from beam pointing perpendicular to the plane of deflection, which causes intensity fluctuations when the beam is re-coupled into a fiber. This problem is mitigated by applying RF at a higher frequency (115 MHz) during periods where the AOM is supposed to be off, heating the device without coupling any diffracted light into the fiber, keeping the temperature constant.

The two laser beams are then sent to the trap at a 90° angle to each other, with a 45° angle to the axial direction of the trap. A GLP and a $\lambda/2$ wave plate each allow control of the polarisation. Each beam contains a sampler, directing some power to a monitoring photo diode (PD). The laser intensity is stabilized by a sample-and-hold PID unit, feeding back on the RF power of the switching AOMs. The beams are steerable using motorized mirror mounts[28] which can be controlled from the experiment control PC, and were typically optimized daily for maximizing coupling to the ions.

4.6 HIGH COLLECTION EFFICIENCY LENS

For both fast and high-fidelity detection of the state of the ions it is desirable to collect as many photons scattered by the ions as possible. While for a surface the available numerical aperture (NA) to the back is limited by the slot, the NA to the front is unobstructed. Exploiting that NA does pose challenges: Room-temperature setups frequently employ inverted view ports to position collection optics close to the ions. Such a viewport, however collides with the need for thermal shields to limit the radiative heat transfer from the warm walls to the cold trap. Out-of-vacuum optics without inverted viewports would require infeasibly

23 Lighthouse Photonics Sprout-G18W
24 Thorlabs GL10-A
25 NKT Photonics aeroGUIDE-5-PM
26 OZ Optics QPMJ-3A3A-400-3/125-3
27 Brimrose QZF-80-40-397
28 Newport 8821 Picomotor Mount

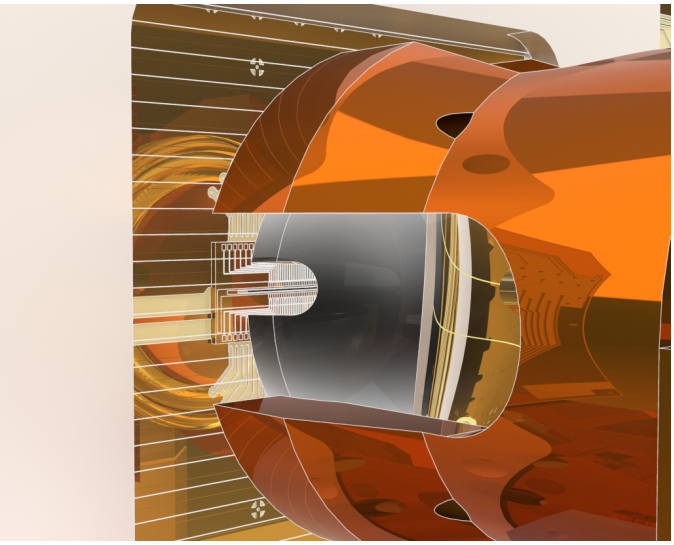

Figure 4.22: View of the trap through the slot in the high NA lens. The cut allows for optical access at 45° to the trap axis.

large optics and demand large holes in the thermal shields which is also undesirable. This leaves in-vacuum optics inside the inner shield as an option where high-NA optics with a small footprint is possible due to the small distance to the trap. However, these optics pose its own set of challenges: To compensate for possible misalignment of the inner lens, it is mounted on two nanopositioners stages[29] which allows us to move the lens perpendicular to the trap axis and to adjust the focal length. The copper lens mount sits atop the nanopositioners, holding the high-NA lens. The lens mount itself must conform to the weight limits of the nanopositioners to be capable of moving at cryogenic temperatures, and is balanced to not exert any torque on the positioners. The aspheric lens with a focal length $f = 9\,\mathrm{mm}$ has been modified to incorporate two slots for laser access, as the radius of the lens exceeds the front focal length, and thus interferes with beams passing at 45°. The slots enable access for the Doppler and repump lasers, with Fig. 4.22 showing a render of the lens from the direction of the Doppler beam.

A secondary lens with an NA of 0.2 and a focal length $f = 22.5mm$ is installed on the backside of the mount, limited by the geometry of the central slot. It allows for additional optical access, and the increased focal length gives a larger field of view. The slot further acts as shutter, blocking light scattered from the surface of the trap. Fig. 4.23 gives a view of the entire assembly with both lenses.

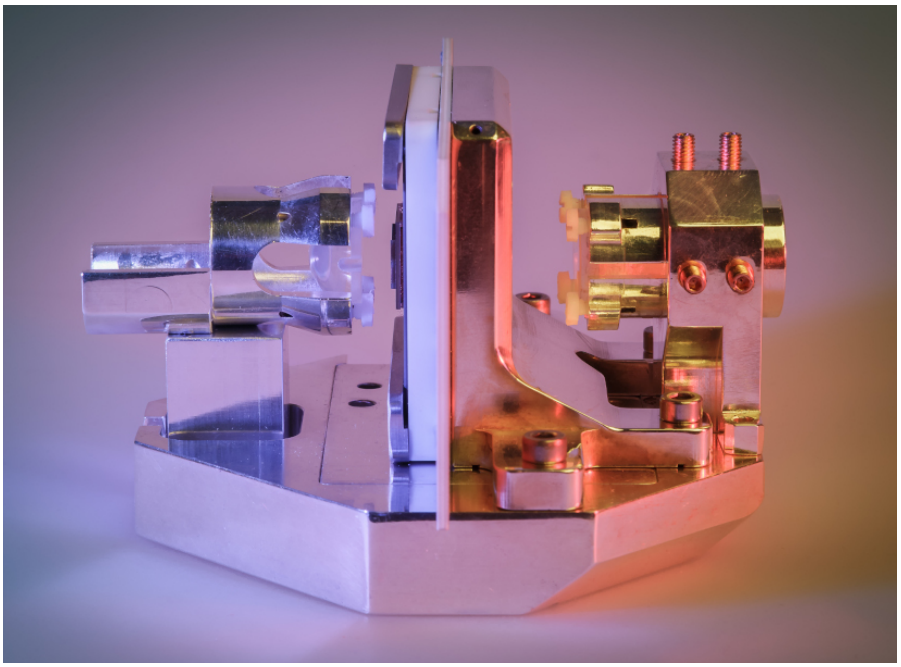

Figure 4.23: TRAP ASSEMBLY WITH LENSES MOUNTED. The high NA lens (NA=0.83, left) has an unobstructed access to the surface, while the lower NA lens (NA=0.22, right) is restricted to the numerical aperture of the slot.

4.6.1 *Fluorescence Detection*

For state detection two tools are available, a PMT[30] and an EMCCD camera. The camera can read out the full state of the ions, but it is limited in terms of readout speed due to the technical overhead in reading out the camera. This overhead is independent of the exposure time. Meanwhile a PMT can be directly read by an electronic counter, but can only record the summed fluorescence of all ions. This limits which states can be distinguished.

By proper blocking of background stray light, we can achieve with the PMT a signal-to-noise ratio of 30 with a bright count rate of $453(3) \times 10^3 \mathrm{s}^{-1}$ for one ion.

To characterize the detection capabilities of the system, we can prepare a single ion in a superposition of the bright $S_{1/2}$ and the dark $D_{5/2}$ state and record the counts on the detecting PMT for a varying duration. The distribution of counts can then be fitted with a sum of two Poisson distributions $c_{\mathrm{dark}} * \mathrm{Pois}(\lambda_{\mathrm{dark}}, n) + c_{\mathrm{bright}} * \mathrm{Pois}(\lambda_{\mathrm{bright}}, n)$, with weights $c_{\mathrm{bright,dark}}$ and the rates $\lambda_{\mathrm{bright,dark}}$ corresponding to the average bright and dark counts. For a given threshold t the detection error can then be determined by integrating the probability distributions over the region corresponding to a misidentification of the state. For

29 Attocube ANPx51, ANPz51
30 Hamamatsu H10682-210

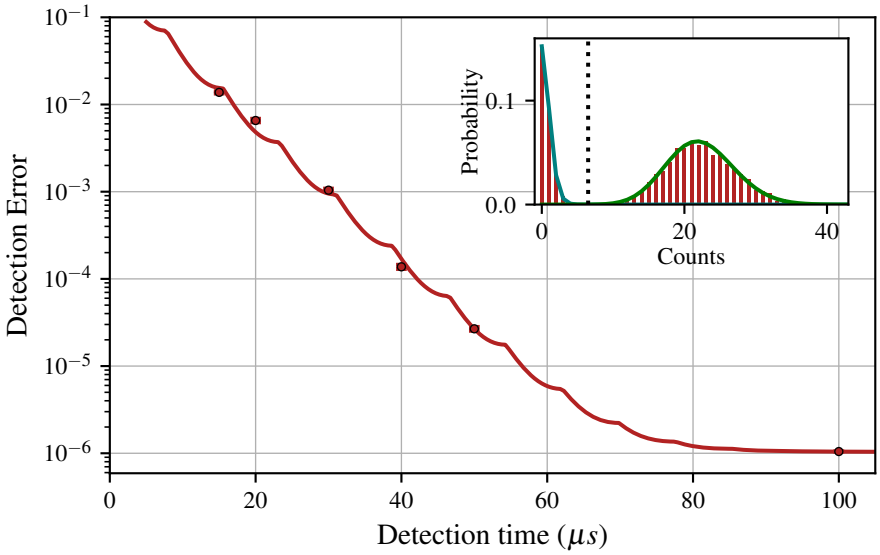

Figure 4.24: DETECTION ERROR FOR A SINGLE ION AS A FUNCTION OF DETECTION TIME. Statistical error bars are comparable to the size of the markers. The steps in the detection error curve correspond to a change of the optimal threshold value. The inset shows the measured distribution of counts for $50\mu s$ detection window. The threshold for which the detection error is minimized is marked with a dotted line.

the bright state this corresponds to the Poisson distribution, while the dark state does acquire an additional correction due to the probability of an ion in the $D_{5/2}$ state decaying to the bright state during the detection time t_{det} due to its finite lifetime of about $\tau \approx 1.1\,\mathrm{s}$. The probability distribution then becomes [117]

$$P_{\mathrm{dark}} = \frac{\tau - t_{det}}{\tau}\,\mathrm{Pois}(\lambda_{\mathrm{dark}}, n) + \frac{t_{det}}{\tau}\,\frac{\Gamma(\lambda_{\mathrm{bright}}, n+1) - \Gamma(\lambda_{\mathrm{dark}}, n+1)}{\lambda_{\mathrm{bright}} - \lambda_{\mathrm{dark}}} \tag{4.3}$$

where $\Gamma(\lambda_{\mathrm{bright,dark}}, n+1)$ is the gamma distribution. By minimizing the summed error for both states over all possible thresholds we can extract the detection error for both states. The summed error is shown in Fig. 4.24 as function of detection time. The steps in the curve correspond to changes of the optimal threshold, which can only take integer values. The lens allows us to achieve a detection error $< 10^{-4}$ in a $50\,\mu\mathrm{s}$ detection window. Such a time window is shorter than a single typically used entangling gate, and thus not a limiting factor. For practical in-sequence detection the timing is instead limited by the requirement for recooling the ion crystal after a bright detection, as that will lead to the ion crystal thermalizing at the Doppler temperature due to the photons being scattered during the detection time.

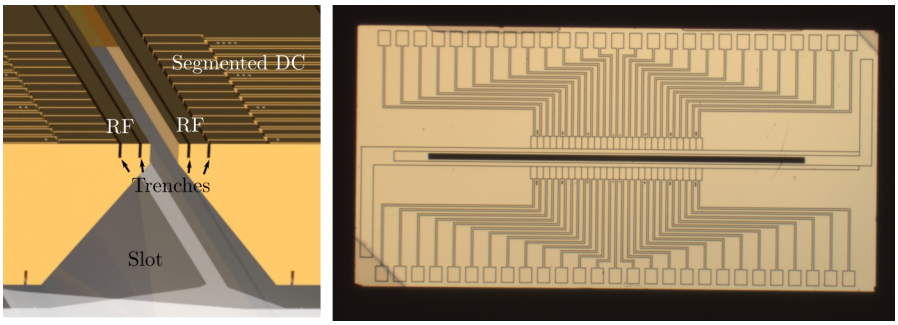

Figure 4.25: LEFT: TRAP CROSS SECTION. Trenches separate the different electrodes. The widening slot allows for optical access from the backside. RIGHT: TOP VIEW OF THE DEVICE. 27 electrode pairs shape the DC potential. The RF electrode is connected from the left, while the central DC electrode is routed in from the right.

4.7 GOLDEN GATE TRAP

The redesign of this setup anticipated use of a segmented surface microtrap developed at Sandia National Labs [118]. As the performance of that trap was insufficient for high-fidelity gate operations, an alternate trap design described in the following was used which we named the *Golden Gate Trap*, details of which can be found in the thesis of Martin van Mourik [97].

4.7.1 *Trap Description*

The surface trap used for the experiments presented in this thesis is an iteration of a design originally developed by the group of Hartmut Häffner at University of California, Berkeley, which was adapted to a previous version of this setup by incorporating a central slot as can be seen on the left of Fig. 4.25, which shows a cross section of the trap structure. The electrode structure can be seen in the top view of the device on the right. The new version of the trap has a tighter electrode spacing of 100µm compared to the previous 200µm electrode pitch. It retains the same optical access with a NA of 0.24 from the backside, with the front NA being unrestricted. The trap consists of a fused silica die that was structured by Translume[31]. The electrodes are then formed by covering the structured die with gold, where the trenches separate the regions being metalized to ensure that they form separately usable electrodes. This step is performed in-house in the cleanroom of the university. After the evaporation step the trap is glued and wirebonded to the interposer PCB (see [97]). This package is then installed in the socket.

31 Translume Inc., 655 Phoenix Dr, Ann Arbor, MI 48108, USA

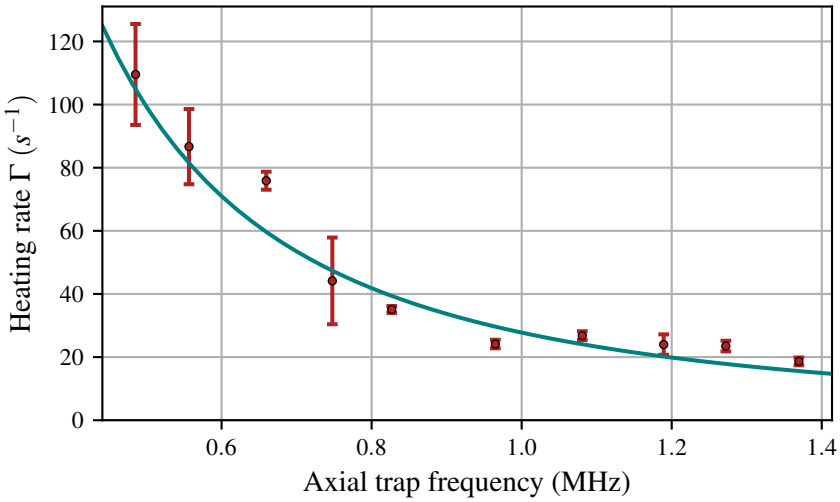

Figure 4.26: Axial heating Rate Γ_{Ca} measured as function of the axial trapping frequency. A power law with an exponent of -1.8(3) has been fitted to the data.

4.7.2 *Motional Characteristics*

When installing a new trap, it is crucial to know the motional coherence of the ions in the trap. For one, the coupling strength of the lasers does depend on the motional state of the ions, and thus a different motional state from the expected one can lead to errors in the rotation angle of quantum operations. Even more sensitive is the effect on entangling operations, which utilize the motional modes of the ion crystal as bus for information. If the motional state changes in an uncontrolled way during a quantum operation, this will directly lead to an error on the gate being performed.

The two characteristics of interest are the heating rate and the motional coherence. The heating rate Γ is determined by measuring the phonon number for different waiting times [119]. The phonon number can be measured using sideband thermometry. Here the spectrum of the red and blue sideband are both measured with a probe duration corresponding to a π-pulse on the blue sideband. The coupling strength of the two transitions depends on the motional occupation number $\overline{n}$, thus for a thermal state we get a total excitation probability

$$P_{\uparrow}(t,\Delta) = \sum_{n=0}^{\infty} \frac{\overline{n}^n}{(\overline{n}+1)^{n+1}} \frac{\Omega_n^2}{\Omega_n^2+\Delta^2} \sin^2(\sqrt{\Omega_n^2+\Delta^2}\, t/2) \tag{4.4}$$

where Δ is the detuning of the sideband, and Ω_n is the motional state dependent coupling strength of the red and blue sideband, respectively. This model of the excitation probability can be fitted to the data. A linear fit as function of waiting time is then used to determine the rate.

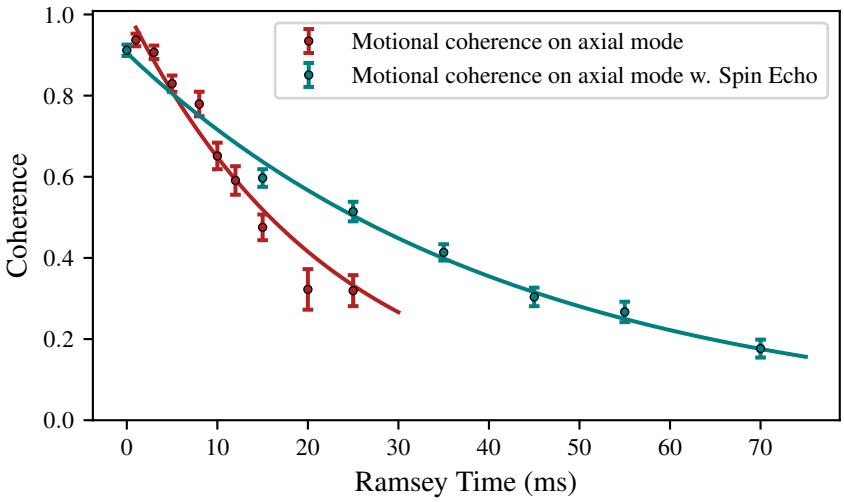

Figure 4.27: Motional coherence of the axial mode at 1.08 MHz measured with a single $^{40}Ca^{+}$ion. The fits correspond to a Ramsey time of 22(2) ms and a spin echo time of 43(2) ms

Fig. 4.26 shows the heating rate for different axial trap frequencies. For our typical operating axial trap frequency of 1.08 MHz we find a heating rate of 27(2) s^{-1}.

The motional coherence can be measured using Ramsey interferometry. First a superposition is created between the $S_{1/2}$ and the $D_{5/2}$ qubit levels with phase 0 on the carrier transition. With a π pulse on the blue sideband the population is then transferred back to the $S_{1/2}$ state, creating a superposition between the $n = 0$ and $n = 1$ motional states. After the interrogation period the motional coherence population in the $n = 1$ state is mapped back to the optical qubit with another π-pulse on the blue sideband followed by a measurement of the contrast, i.e. a $\pi/2$-pulse with variable phase on the carrier. Fig. 4.27 shows the measured contrast as function of the waiting time. For the spin echo, a π pulse on the carrier is interleaved between two π pulses on the blue sideband. We measure a motional coherence time of 22(2) ms(43(2) ms) without (with) spin echo. The difference between the two values indicates the presence of slow fluctuations of the trap frequency, likely induced by the voltage supply.

5

AUTOMATED GATE CALIBRATION

The work presented in this chapter has been published in:

L. Gerster, F. Martínez-García, P. Hrmo, M. van Mourik, B. Wilhelm, D. Vodola, M. Müller, R. Blatt, P. Schindler, and T. Monz
"Experimental Bayesian calibration of trapped ion entangling operations"
PRX Quantum, vol. 3, no. 2, (2022)[1]

F. Martínez-García, L. Gerster, D. Vodola, P. Hrmo, T. Monz, P. Schindler, and M. Müller
"Analytical and experimental study of center-line miscalibrations in Mølmer-Sørensen gates"
Phys. Rev. A, vol. 105, no. 3, (2022)[2]

The fidelity of a quantum gate operation depends on its control parameters, and the ability to correctly determine these control parameters is a requirement to consistently achieve fidelities limited by the noise processes of a system. Additionally, gates acting on different subsets of qubits may require unique sets of control parameters, making it increasingly challenging for an operator to manually calibrate the gates.

Thus we want to find a calibration procedure that can determine the optimal control parameters accurately and without human intervention, such that the procedure can be integrated into a larger framework for calibrating all the elementary operations of a trapped ion quantum computer system.

In this chapter we first discuss the creation of a model that describes the action of a miscalibrated Mølmer-Sørensen gate. We then describe how Bayesian inference can utilize such a model to generate parameter estimates from measurements, and discuss the issues arising to practically apply the Bayesian parameter estimation to the particular problem of the Mølmer-Sørensen gate. We test the algorithm by running it on our trapped ion system, and characterize the performance of the procedure with regards to consistency and achievable infidelity as well as the time required for the algorithm.

1 The author of the present thesis designed the experiment, measured and analyzed the data.

2 The author of the present thesis measured and analyzed the data.

5.1 MODEL GENERATION

As a starting point for the model we use the interaction of the ideal Mølmer Sørensen gate that has been previously discussed in Section 3.5.4. From this we identify the parameters of the interaction Hamiltonian that need to be determined for the correct application of the gate. We find the set of parameters

$$\mathbf{\Theta} = (\Omega, \omega_{cl}, \delta, \Delta\varphi), \tag{5.1}$$

where Ω is the carrier Rabi frequency, ω_{cl} the center line detuning, δ the sideband detuning, and $\Delta\varphi$ the phase difference of the gate, as they all can be affected by the control parameters.

These gate parameters should be as close as possible to their optimal values

$$\mathbf{\Theta}_{opt} = \left(\Omega_{opt} = \frac{\pi}{\eta t_g}, \omega_{cl,opt} = 0, \delta_{opt} = \frac{2\pi}{t_g}, \Delta\varphi_{opt} = 0\right) \tag{5.2}$$

to achieve a high-fidelity gate.

As we are focusing on the effects of systematic parameter miscalibration, we are neglecting incoherent error sources such as finite motional and spin coherence times, laser amplitude noise, resonant carrier excitation or unequal coupling strengths to the ions.

We need to first verify that this description of the gate agrees with the experimental results, as the success of the routine presented later depends on the quality of this description, and to justify the neglecting of the additional error sources.

To this purpose, we measure the population outcome probabilities of different gate sequences as function of the control parameters. In Fig. 5.1 the expectation values obtained from numerically integrating the Hamiltonian are being compared with the measurements in the experiment for different numbers of applied gates to validate the model. For the numerical simulations, the QuTiP software package [120] written in the python programming language was used.

Comparing the measurement results to numerical simulations with the same parameters, we calculate reduced χ^2 values of < 2.5 for varying the center line detuning, sideband detuning and phase, while the Rabi frequency scans for $N_g = 5$ and $N_g = 7$ gates have higher χ^2 values of up to 4. We attribute the higher χ^2 to the AC Stark shift not being re-compensated during these measurements as the actual laser power was varied instead of adjusting detuning and gate time to control the effective Rabi frequency Ω, leading to a simultaneous shift of the effective center line detuning. While the χ^2 are larger than one, these results do indicate that the Hamiltonian (Eq. (3.51)) captures the effects of the parameter miscalibrations and is not dominated by unmodelled error sources. This suggests that the described Hamiltonian is a viable model to describe our experimental

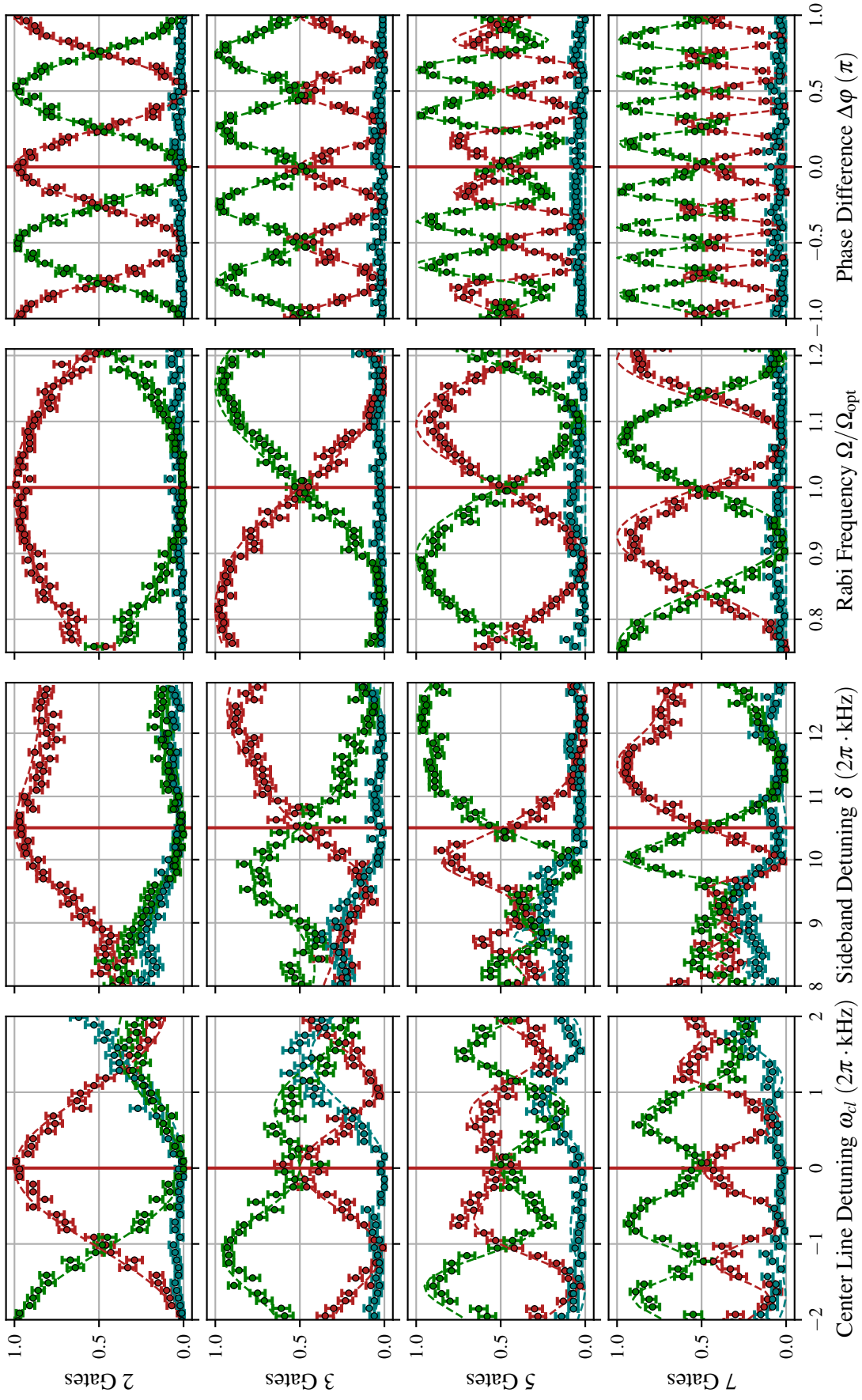

Figure 5.1: Dependency of the populations $|gg\rangle$ (green), $|ee\rangle$ (red), $|eg\rangle$ and $|ge\rangle$ (blue) on the control parameters after the application of 2, 3, 5, and 7 gates. For each measurement run the other parameters have been held constant at the optimal value for the Mølmer-Sørensen gate. The error bars are estimated from shot noise. The vertical lines indicate the target value for each parameter and dashed lines display the numerical simulations.

system, and the results from numerically integrating the dynamics can be used as a probability landscape to perform Bayesian inference on.

5.1.1 *Experimental Control Parameters*

We previously identified that calibrating the Mølmer-Sørensen gate requires to set the parameters of the interaction Hamiltonian (Eq. (5.1)) to the optimal values given in Eq. (5.2). The challenge now lies in that we do not have direct access to the parameters of the Hamiltonian, but we instead rely on changing the control parameters of the gate

$$\Xi_c = (t_g, f_{cl}, f_{sb}, \phi), \tag{5.3}$$

i.e. the gate time t_g, the common frequency $f_{cl} = (f_r + f_b)/2$ is the mean frequency between the red (f_r) and blue (f_b) tone of the laser, the difference frequency $2f_{sb} = f_b - f_r$ of the bichromatic laser field, and the difference in the common phases between consecutive gates, ϕ, of the two laser tones.

These control parameters Ξ_c can be used to calibrate the gate in the following way: By performing measurements of the populations of the ions after the application of a gate sequence we can obtain estimates of the parameters of the Hamiltonian that we denote as

$$\overline{\Theta} = (\overline{\Omega}, \overline{\omega}_{cl}, \overline{\delta}, \overline{\Delta\varphi}), \tag{5.4}$$

of the current parameters Θ. The control parameters Ξ_c can then be adjusted to set the parameters Θ to Θ_{opt} given the estimates of the parameters of the interaction Hamiltonian: The time of the gate will be corrected as

$$t_g \to t_g \frac{\Omega_{opt}}{\overline{\Omega}}, \tag{5.5}$$

where we choose to change the time of the gate instead of the laser power since it is easier to control in the experiment, while producing an equivalent correction. This both avoids any non-linearity of the AOM and allows us to make use of all the available power.

The other corrections are implemented by subtracting the difference between the estimated and the ideal parameter value from the control parameter. In the case of the sideband detuning this is given by

$$f_{sb} \to f_{sb} - \overline{\delta} + \delta_{opt}, \tag{5.6}$$

where f_{sb} is the corresponding control parameter. As for the correction of the center line detuning, this is described by

$$f_{cl} \to f_{cl} - \overline{\omega}_{cl} + \omega_{cl,opt}. \tag{5.7}$$

Finally, the phase between consecutive gates is changed by

$$\phi \to \phi - \overline{\Delta\varphi} + \Delta\varphi_{opt}. \tag{5.8}$$

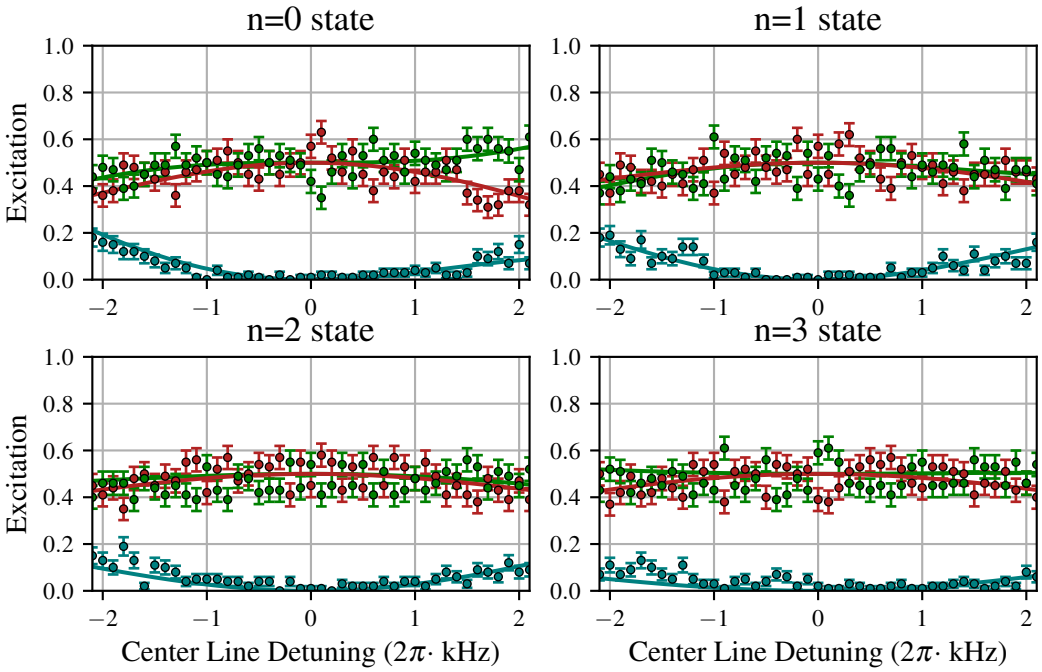

Figure 5.2: Measured populations for center-line detuned MS Gates applied to different Fock states. Solid lines correspond to model predictions by numerical integration.

With this set of rules, we update the parameters of the MS gate to iteratively bring the parameters $\boldsymbol{\Theta}$ to converge to $\boldsymbol{\Theta}_{opt}$ as the estimates are getting refined as more measurement data is being added.

5.1.2 *Model Validation with higher Fock States*

While the primary focus was on generating a suitable model to be used for gate calibration, its behaviour can also be explored in regimes usually not utilized for driving gates. One such example is to look at the different initial motional Fock states of the harmonic oscillator mode.

One of the advantageous features of the Mølmer-Sørensen gate is its insensitivity to the population of the motional mode, such that it can even be driven with thermal states [122]. Thus, for a perfectly calibrated gate, no differences are expected compared to the case of the gate driven starting from the motional ground-state. This behaviour however changes when considering parameter miscalibrations as can be seen in Fig. 5.2, where the center line detuning shows an asymmetric behavior of the populations for $n = 0$, while for higher Fock states the populations become more symmetric around 0 center line detuning.

Experimentally, the Fock states were prepared by shelving one ion to the $D_{5/2}$ manifold using the addressed beam [58]. Then π-pulses are alternatingly applied on the blue and red sideband on the axial

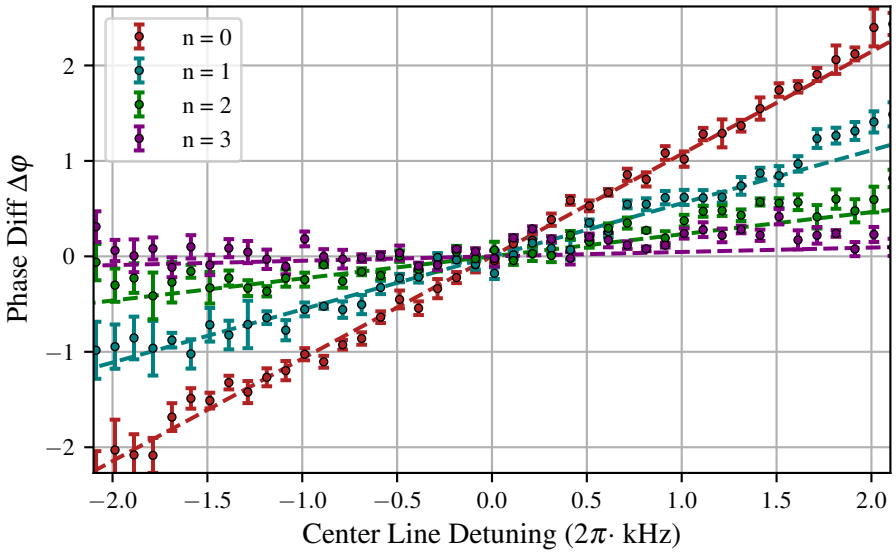

Figure 5.3: PHASE SHIFTS FOR A CENTER-LINE DETUNED MS GATES APPLIED TO DIFFERENT FOCK STATES. Dashed lines correspond to theory predictions from first order Magnus expansion of the Hamiltonian.

COM mode, with each pulse adding one phonon [67]. For odd target states a π pulse on the carrier is added to return to the electronic ground state. The preparation sequence is terminated by a final pulse returning the shelved ion. After the preparation sequence for Fock states $n > 0$, we measure 5% population outside the target electronic state, which decreases the signal-to-noise ratio of the measurement. We use an additional repumping step to return this population to the electronic ground state, but this leaves us with a corresponding error in the initial prepared Fock state.

We then perform a sequence of two center line detuned MS gates, where we intentionally change the phase φ_d of the second one with

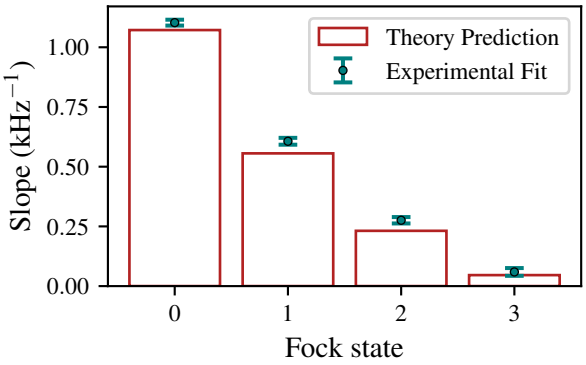

Figure 5.4: SLOPES OF PHASE SHIFTS FOR DIFFERENT FOCK STATES The linear fits to the data in Fig. 5.3 is compared to theory predictions from a semi-analytical model [121].

respect to the first one. For small center line detunings the state is then predicted by

$$P(ee) = \frac{1 + \cos(2\varphi_d + \phi(\omega_{cl}, n))}{2} \tag{5.9}$$

where $\phi(\omega_{cl}, n)$ denotes the phase shift depending on detuning and motional state. $\phi(\omega_{cl}, n)$ can then be extracted by fitting a sine to the measured populations as function of φ_d. Offset and amplitude of the fitting function are kept as free parameters to account for SPAM errors and errors of this simplified model.

The results are shown in Fig. 5.3, showing to first approximation a linear relationship between centerline detuning and the acquired phase, the slope of which depends on the initial motional Fock state.

In Fig. 5.4 these slopes are compared to theory predictions, where we find good agreement between the values predicted by a semi-analytical model applying a Magnus expansion to the Hamiltonian [121], and the slope of the measured experimental data.

5.2 BAYESIAN INFERENCE ALGORITHM

The model developed previously can predict the measurement outcome probabilities for a given set of parameters of the Hamiltonian. For the task of calibrating a gate, we are interested in the inverse problem, finding a set of parameters given a set of measurement outcomes. Bayesian statistics offers the tools to accomplish precisely this.

Bayes' theorem [123] prescribes how to estimate the probability distribution of a set of parameters $\mathbf{\Theta}$, given a prior distribution before the measurement $P(\mathbf{\Theta})$, a measurement with outcome m, and the likelihood of obtaining this measurement outcome according to the model of the process, $P(m|\mathbf{\Theta})$. The result is an updated probability distribution called the posterior distribution

$$P(\mathbf{\Theta}|m) = \frac{P(m|\mathbf{\Theta})P(\mathbf{\Theta})}{P(m)} \tag{5.10}$$

where $P(m)$ is the marginal likelihood, and effectively corresponds to a normalization factor as it does not depend on the set of parameters $\mathbf{\Theta}$, and thus does not affect the relative probabilities [124].

We can apply Bayes' theorem iteratively as new measurements are performed, for each one inserting the previously obtained posterior as the new prior for the subsequent measurement. This results in an iterative process where the probability distribution after T measurements is then given by

$$p(\mathbf{\Theta}|m_1, ..., m_T) \equiv p(\mathbf{\Theta}|m_{1:T}) \propto P(\mathbf{\Theta}) \prod_{t=1}^{T} P(m_t|\mathbf{\Theta}), \tag{5.11}$$

where we assume that all the measurement outcomes, m_t for $t = 1, ..., T$, are independent from each other. In order to refine the parameter estimates we want the degree of uncertainty of the parameters

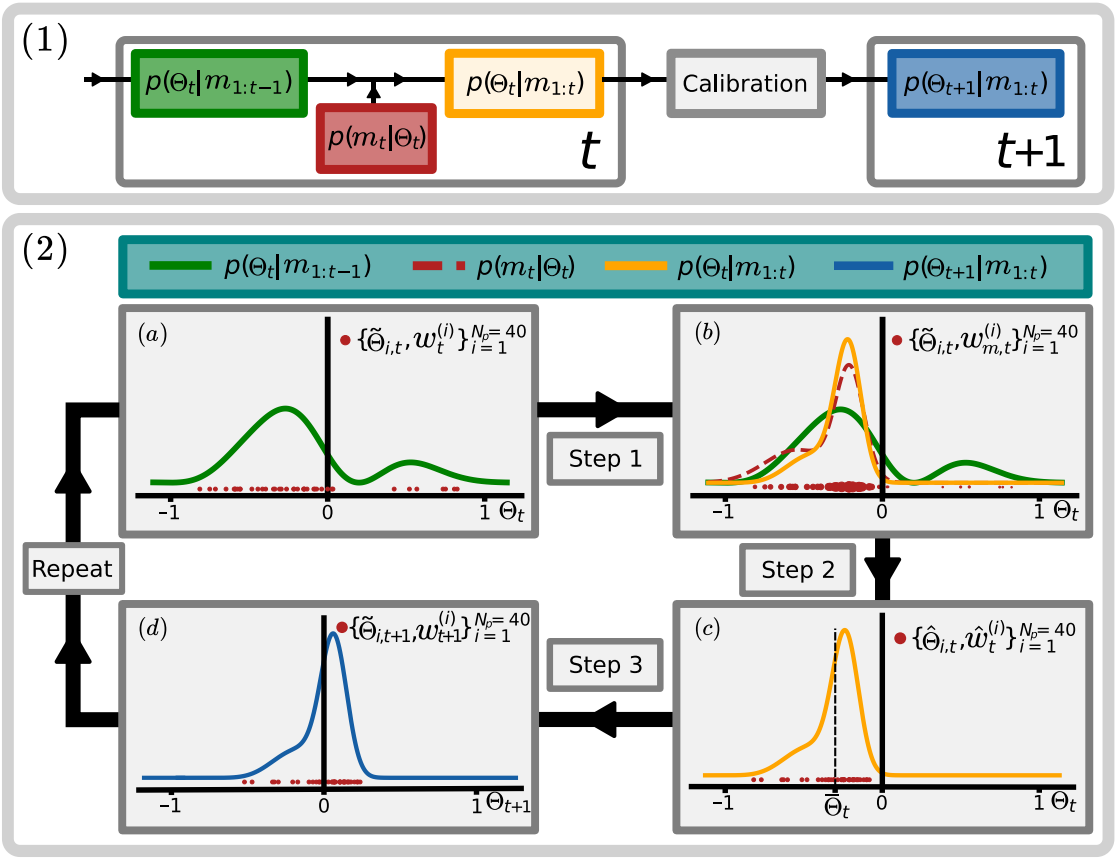

Figure 5.5: TOP (1): REPRESENTATION OF A CYCLE OF THE CALIBRATION PROCESS. The initial probability distribution at iteration t with $t-1$ measurements, $p(\boldsymbol{\Theta}_t|m_{1:t-1})$, is updated by performing a new set of measurements, m_t, to obtain $p(\boldsymbol{\Theta}_t|m_{1:t})$. The estimates obtained from this probability distribution can then be used to calibrate the parameters, obtaining the initial probability distribution for iteration $t+1$.
BOTTOM (2): STEPS FOLLOWED TO PERFORM AN ITERATION OF THE PARTICLE FILTERING ALGORITHM. A simplified case with only one parameter, Θ is shown here. In (a) we have particles $\{\tilde{\Theta}_{i,t}, w_t^{(i)}\}$ (red dots) from the prior probability distribution $p(\Theta_t|m_{1:t-1})$ (green). A new set of measurements is performed to obtain the posterior probability distribution $p(\Theta_t|m_{1:t})$ (yellow) in (b) by using the likelihood of the outcome obtained for the measurement, $p(m_t|\Theta_t)$ (red). The weights are updated following Eq. (5.13), where a bigger weight is visually represented by a bigger size of the particle. These weighted particles can be used to obtain the estimate of the parameter at this iteration, $\bar{\Theta}_t$, by using Eq. (5.14). In (c), a resampling process is performed to obtain particles with equal weights that approximate particles from the posterior probability distribution. The previously obtained value $\bar{\Theta}_t$ is also shown here. Finally, in (d), $\bar{\Theta}_t$ has been used to calibrate the parameter Θ, where for this example we are assuming that the ideal value of Θ is zero, therefore, the correction applied is to change the value of the parameter by $-\bar{\Theta}_t$. The probability distribution $p(\Theta_{t+1}|m_{1:t})$ (blue) consequently has an estimate of zero.

$\boldsymbol{\Theta}$ to decrease for an increasing number of measurements. This convergence is dependent on the choice of the measurement settings, as they affect how much information can be gained about the parameters. The process can be terminated if a desired limit of uncertainty for the estimates of $\boldsymbol{\Theta}$ is reached.

The framework just described can be mapped to a quantum experiment as follows:

- The process of the gate can be simulated to provide a model.
- The experiment provides discrete measurement outcomes.
- Repeated measurement outcomes are independent of each other.

It thus looks promising to be applicable for inferring the parameters $\boldsymbol{\Theta}$ of the Mølmer-Sørensen gate. However, while the model probabilities $P(m|\boldsymbol{\Theta})$ can be obtained by integrating the Hamiltonian in Eq. (3.51) for $\omega_{cl} \neq 0$, no analytical solution is known that results in a closed-form expression for these probabilities. As a consequence this type of miscalibration can only be studied numerically [122]. Without a closed-form expression, the Bayesian inference cannot be performed using analytic expressions of the probability distribution either, and has to be performed using discretized representations of the continuous probability functions, which will be described in detail in the following section.

5.2.1 *Particle Filters*

We can approximate the continuous probability distributions using a so-called particle filter[3] [125–127], where we represent the probability function by a sum of N_p weighted particles instead:

$$p(\boldsymbol{\Theta})d\boldsymbol{\Theta} \approx \sum_{i=1}^{N_p} w^{(i)} \delta(\boldsymbol{\Theta} - \widetilde{\boldsymbol{\Theta}}_i) d\boldsymbol{\Theta}, \tag{5.12}$$

with $\delta(\boldsymbol{\Theta} - \widetilde{\boldsymbol{\Theta}}_i)$ being the Dirac delta function around the vector of parameters $\widetilde{\boldsymbol{\Theta}}_i$. Each parameter vector $\widetilde{\boldsymbol{\Theta}}_i$ corresponds to a single particle with the associated weight $w^{(i)}$, and the set $\{\widetilde{\boldsymbol{\Theta}}_i, w^{(i)}\}_{i=1}^{N_p}$ forms the particle filter.

The Bayesian inference requires a choice of an initial prior, which is then transformed into a set of particles. A Gaussian function is a simple choice for an initial prior, corresponding to knowing a mean and standard deviation of the parameters, and allows for computationally inexpensive sampling from the distribution. We can then initialize the particle filter from that prior probability function by randomly sampling N_p times from the distribution and setting all the weights to $1/N_p$.

3 The nomenclature of a filter stems from filtering estimates out of a stream of noisy measurement data

5.2.2 *Bayesian Update*

In the next step we want to look at how these discretized probability function is getting updated. The procedure which is described in the following is illustrated in Fig. 5.5 for a one-dimensional example. The particle filter $\{\widetilde{\boldsymbol{\Theta}}_i, w^{(i)}\}_{i=1}^{N_p}$ is updated to incorporate the outcome m obtained by performing a measurement by adjusting the weights, according to the formula

$$w_m^{(i)} \propto P(m|\widetilde{\boldsymbol{\Theta}}_i) w^{(i)}. \tag{5.13}$$

The weights $w_m^{(i)}$ are normalized such that $\sum_{i=1}^{N_p} w_m^{(i)} = 1$, ensuring that the filter represents a valid probability distribution. This corresponds to step 1 in Fig. 5.5(2)

The update procedure requires the model probabilities $P(m|\widetilde{\boldsymbol{\Theta}}_i)$ for each discrete particle. These could be obtained by numerically integrating the Hamiltonian given in Eq. (3.51) for each specific set of parameters. However, performing these numerical calculations during an optimization run in real time would be prohibitively time consuming, as the computation for a single particle requires $\approx 1s$ on a desktop computer[4]. This would result in a computation time of several hours to update 10000 particles which we use in our particle filter (See Section 5.6).

To speed this process up, we instead precompute the outcome probabilities of a single experimental shot on an equally spaced 4 dimensional grid, corresponding to the 4 parameters of the Hamiltonian (Eq. (5.1)). The outcomes for particles with values between those grid points can then be calculated using an interpolation function. We use a cubic spline interpolator [128], which allows us to better approximate the outcome probabilities without increasing the number of grid points required compared to using linear interpolation. The spline interpolator requires a careful choice of grid parameters, for example to prevent nonphysical probabilities < 0 the number of points for interpolating the phase difference $\Delta\varphi$ is chosen such that the local extrema of the outcome probabilities when varying solely the phase difference do align with the grid points. The choice of the number of grid points and their ranges is shown in Table 5.1.

Querying the interpolation function to receive the outcome probabilities at any set of parameters inside the region can be done quickly, with 10000 particles taking approximately $100 - 500$ms to compute[5]. This computation is faster than the time required to acquire the experimental data for a single iteration (see Section 5.4), and thus does not represent a limiting factor on the total time of an optimization run.

We additionally include in our model probabilities a small amount (1%) of depolarizing noise to account for experimental errors, such

4 CPU: Intel i5-4670S@3.10GHz
5 CPU: Intel i7-6700K@4.00GHz

as SPAM, motional and spin dephasing errors. This is necessary as noise is always present, preventing the expectation values $P(|e,g\rangle)$ and $P(|g,e\rangle)$ from going to zero, while the perfect model predicts arbitrarily small expectation values at the targeted gate parameters. Without this adjustment any measurement result of an unwanted state $|g,e\rangle$ or $|e,g\rangle$ causes a strong suppression of the probability at the center of the distribution due to the small expectation value for the outcome, and any difference between the perfect model and the experimental outcomes causes instabilities in convergence. The added depolarizing noise instead limits how much the likelihood can be adjusted by a measurement of $|g,e\rangle$ or $|e,g\rangle$.

5.2.3 *Parameter Estimation*

From the particle filter we want to extract the important statistical information, most notably the mean $\overline{\boldsymbol{\Theta}}$ and the variance $\mathrm{Var}(\boldsymbol{\Theta})$ of the probability distribution. The particle filter allows us to directly extract these values, the integrals of the estimators over the probability distribution are transformed by Eq. (5.12) into

$$\overline{\boldsymbol{\Theta}} = \sum_{i=1}^{N_p} w_m^{(i)} \widetilde{\boldsymbol{\Theta}}_i, \tag{5.14}$$

$$\mathrm{Var}(\boldsymbol{\Theta}) = \sum_{i=1}^{N_p} w_m^{(i)} (\widetilde{\boldsymbol{\Theta}}_i - \overline{\boldsymbol{\Theta}})^2. \tag{5.15}$$

This information can be used to adjust the control parameters, to monitor the convergence of the calibration routine (see Section 5.3), and they can also inform decisions about the next experimental setting discussed in Section 5.4.

5.2.4 *Resampling*

We are expecting the probability distributions to converge as information from more measurements is added. This corresponds to a

Table 5.1: Choice of simulation parameters for range and spacing of the interpolation grids. The simulation points are linearly spaced over the given range. The gates are simulated for a 100µs gate duration.

	1 Gate		2-7 Gates	
	Range	Points	Range	Points
Ω/Ω_{opt}	1 ± 0.5	21	1 ± 0.5	21
ω_{cl}	$0 \pm 7 \cdot 2\pi$kHz	21	$0 \pm 3.5 \cdot 2\pi$kHz	21
δ	$10 \pm 10 \cdot 2\pi$kHz	21	$10 \pm 5 \cdot 2\pi$kHz	21
$\Delta\varphi$	0	1	2π	25

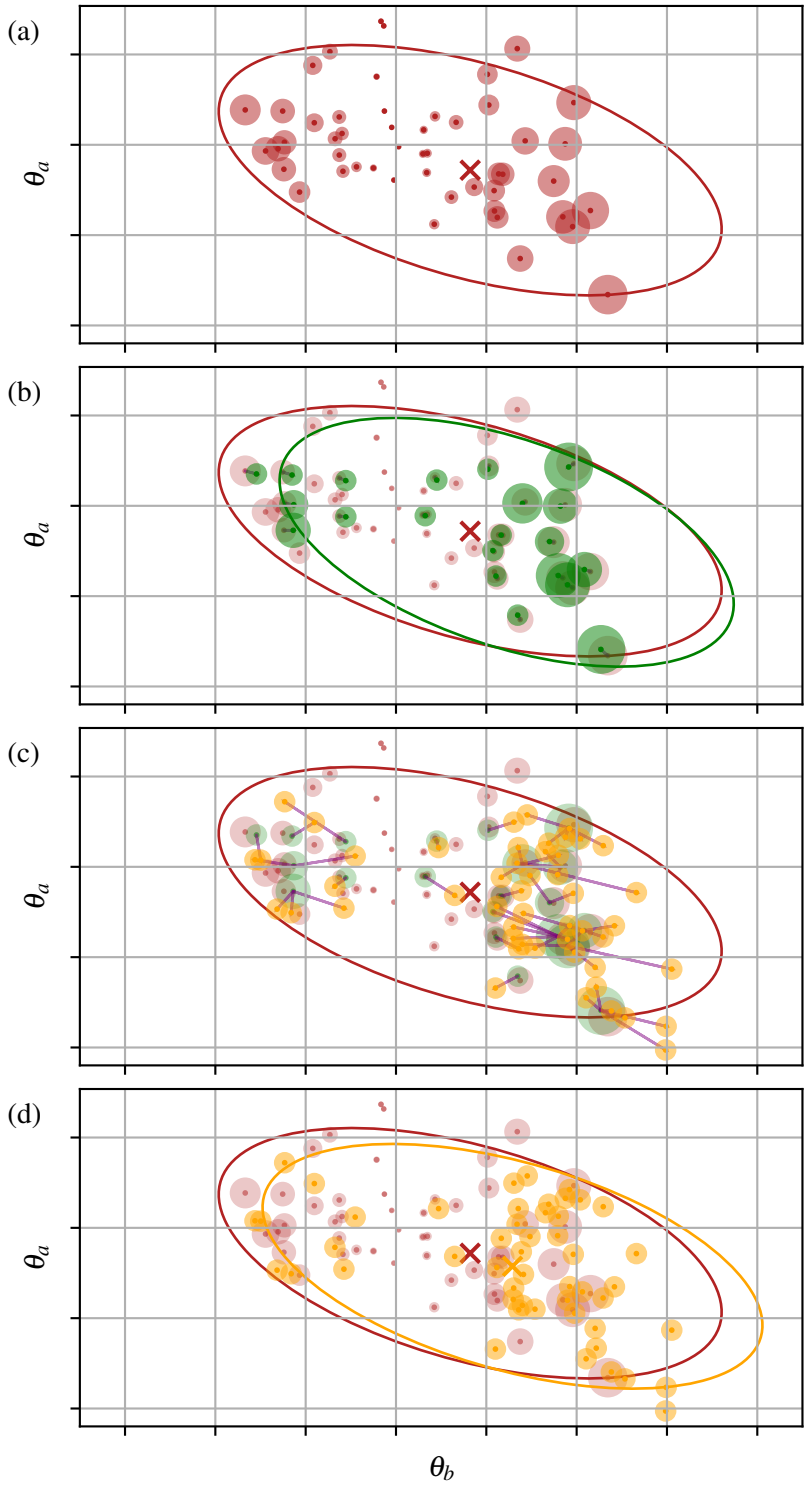

Figure 5.6: ILLUSTRATION OF THE RESAMPLING PROCESS. The distribution of weighted particles (the size of red dots indicates the weight) in (a) should be resampled while preserving the mean and covariance (ellipse and x in red). In (b) a new set is drawn from the weighted particles and moved towards the mean (covariance ellipse shown in green). As the points are sampled with replacement, some are chosen multiple times (the size of green dots indicates the frequency). In (c) offsets are randomly sampled from a normal distribution with a covariance matrix calculated from the covariance matrix of the initial distribution according to Algorithm 5.1 and are then added to the newly drawn points to lift the degeneracy of multiply chosen points. In (d) the new set of equally weighted points (yellow) now represents the distribution, the starting (red) and final (yellow) mean and covariance are shown. The process is shown in two dimensions for ease of illustration, with the axis θ_a, θ_b corresponding to two parameters of Θ.

Algorithm 5.1 : Liu-West Resampling

INPUT : A list of N_p weighted particles $\{w^{(i)}, \boldsymbol{\Theta}_i\}$ with dim n
loss parameter a
OUTPUT : A list of M_p equally weighted particles $\boldsymbol{\Theta'}_j$

BEGIN
  Set parameter h to $\sqrt{1-a^2}$
  Compute mean $\overline{\boldsymbol{\Theta}}$ over all particles $\widetilde{\boldsymbol{\Theta}}_i$ with weights $w^{(i)}$
  Compute covariance matrix $\mathrm{Cov}(\boldsymbol{\Theta})$ over all particles $\widetilde{\boldsymbol{\Theta}}_i$ with weights $w^{(i)}$
  Compute matrix square root S of $h \cdot \mathrm{Cov}(\boldsymbol{\Theta})$
  FOR $j \leftarrow 0$ TO M_p DO
    Randomly select s from $\overline{\boldsymbol{\Theta}}$ weighted by $w^{(i)}$
    Draw a sample N from a n-dimensional normal distribution
    Set $\boldsymbol{\Theta'}_j$ to $a \cdot s + (1-a) \cdot \overline{\boldsymbol{\Theta}} + \langle S, N \rangle$
  END
  RETURN *List of particles* $\boldsymbol{\Theta'}_j$
END

decrease of the variance of the parameter estimates, indicating that information about the parameters is being gained from the performed measurements. Repeatedly updating the weights poses a problem for the particle filter since it leads to many particle weights going to zero while simultaneously having only a few particles with high weights. This situation causes both unnecessary computations to update the weights on particles that represent a small probability and thus contribute little to the estimates, and under-sampling of the distribution around the particles with high probability, limiting the final precision of the estimate.

We counteract this problem by a so-called *resampling procedure* [129, 130], where we generate a new set of particles with equal weights to represent the same probability distribution, corresponding to step 2 in Fig. 5.5 (2).

$$\{\widetilde{\boldsymbol{\Theta}}_i, w_m^{(i)}\}_{i=1}^{N_p} \rightarrow \{\hat{\boldsymbol{\Theta}}_i, \hat{w}^{(i)} = 1/N_p\}_{i=1}^{N_p} \tag{5.16}$$

We use the Liu-West algorithm [131] for this task described in Algorithm 5.1, which generates a new set of particles by randomly sampling with replacement from the old weighted particles. The behavior of the algorithm is graphically shown in Fig. 5.6. Sampling with replacement already generates a set of equally weighted particles, but particles cannot explore new locations since they are up to this point duplicates of particles of the old set. To lift this degeneracy every particle of the filter is moved towards the mean of the filter. The loss parameter a of Algorithm 5.1 controls this interpolation, and has been kept at 0.98 for the work presented here. This corresponds in Fig. 5.6 to

selecting the distribution in (b) from the initial distribution in (a). A random perturbation is then applied to each particle, with the values of the perturbation sampled from a normal distribution. In Fig. 5.6 this matches generating the distribution shown in (c) from (b). The covariance matrix of this normal distribution is chosen as described in Algorithm 5.1 such that the mean and covariance of the particle filter is preserved. In Fig. 5.6 (d) the mean and covariance of the initial and final distribution are shown, with the visible mismatch due to the low number of particles used in the illustration.

5.2.5 *Feedback*

The last step remaining to complete the parameter estimation protocol is to transform the posterior probability distribution into the prior distribution for the next iteration. This is step 3 illustrated in Fig. 5.5(2). We calculate the required adjustments of our experimental control parameters Ξ_c for a gate with no miscalibration using Eqs. (5.5)-(5.8), given the current knowledge of our parameter estimates (Eq. (5.4)). We also apply these corrections to the positions of our particles such that the expectation values of the new prior now fulfill the relations required for a perfect gate. These new values for the experimental control parameters Ξ_c can now be used in the next iteration of the algorithm, performing additional measurements with the new settings, iteratively improving the estimates of the parameters. An example of this behaviour estimating the four MS gate parameters is shown in Fig. 5.7, where the probability distributions are mapped to the experimental control parameters t_g, f_{sb}, f_{cl}, and ϕ. At each update, 100 experimental shots are performed using the best estimates for the control parameters by the previous iteration and the particle filter is then updated according to those measurement results. Over several iterations the probability distribution narrows, reducing the uncertainty on the estimates (shown in orange), and the changes to the control parameters become smaller between iterations until the distribution fulfills the termination criterion, which will be explained in the following section.

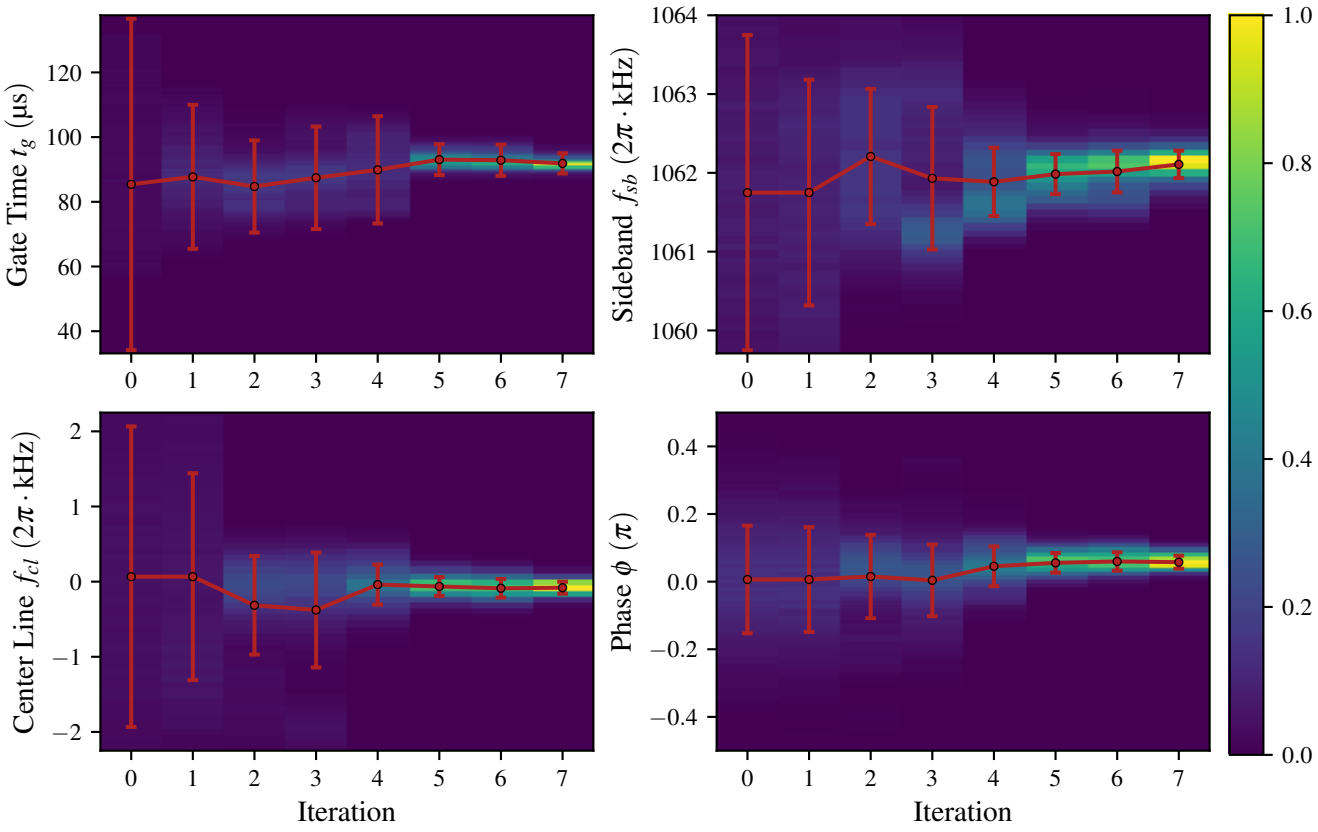

Figure 5.7: PROJECTIONS OF THE PARTICLE FILTER FOR THE CONTROL PARAMETERS Ξ_c AT EACH ITERATION OF A SINGLE CALIBRATION RUN. The same filter is projected to each of its 4 dimensions. The mean and standard deviation of the probability distribution of the control parameters calculated using the relations in Eqs. (5.5) to (5.8) is shown in orange. The probability density of each plot is normalized to its maximum. Each iteration uses the measurement outcomes of 100 repetitions of the experiment to update the probability density. As an initial prior a Gaussian with widths of $\sigma_\Omega = 0.2 \cdot \Omega_{opt}$ Rabi frequency uncertainty, $\sigma_{\omega_{cl}} = 2 \cdot 2\pi\text{kHz}$ center line uncertainty, $\sigma_\delta = 2 \cdot 2\pi\text{kHz}$ sideband uncertainty and $\sigma_{\Delta\varphi} = 0.16\pi$ phase uncertainty was chosen, which corresponds to typical experimental uncertainties after preliminary calibration.

5.3 STOPPING CRITERION FOR THE ALGORITHM

The standard deviations from the probability distributions provide a measure of progress of the routine, but this measure does raise the question of how accurately do the parameters need to be determined. Typically, entangling gates are not quantified by the uncertainty in their control parameters, but rather by the fidelity [32] of the output state compared to the ideal expected state, averaged over all possible input states.

As the fidelity of any real gate is limited by incoherent noise processes, it is thus sufficient to determine the parameters to an accuracy so the gate fidelity is limited by the present stochastic noise instead of the errors due to calibration.

A naive approach may look at the fidelities of the gate sequences used in the tuneup routine, but here the fidelity of different gate sequences have different dependencies on the parameters. Furthermore, all the errors considered here are coherent, and as a consequence the fidelity does not scale exponentially with the number of gates which makes it hard to assign a per-gate error.

5.3.1 *Randomized Benchmarking*

By averaging fidelities obtainable for various inputs states and unitary gate sequences, a more relevant quantity for performing an algorithm, the average gate fidelity, can be extracted [132–134]. In order to relate miscalibrated parameters to gate fidelity, we simulate randomized cycle benchmarking [135] with mis-set parameters. Here the multiple applications of the Mølmer-Sørensen gates are interleaved with random single qubit Pauli operations. We consider the effect of the parameters individually where only one parameter is imperfectly chosen, with the resulting infidelities shown in Fig. 5.8. For each parameter we can then define a threshold T_Θ which defines an acceptable region in which a miscalibration is no longer expected to significantly influence the gate performance. In our case we choose a threshold of $2 \cdot 10^{-3}$ for the infidelity caused by a miscalibration of that single parameter, leading to a choice of thresholds on the individual parameters of $T_\Omega = 0.02 \cdot \Omega_{opt}$, $T_{\omega_{cl}} = 150 \cdot 2\pi\text{Hz}$, $T_\delta = 200 \cdot 2\pi\text{Hz}$, $T_{\Delta\varphi} = 0.028\pi$. We proceed to run the calibration algorithm until the particle filter converges in all four dimensions to an uncertainty below the thresholds. Assuming the parameters are normally distributed with the standard deviation of the distributions equal to the thresholds, we expect from simulation a median infidelity of $\approx 5 \cdot 10^{-3}$, but correlations between the errors in the parameters are expected to significantly affect the expected infidelity (see Section 5.7).

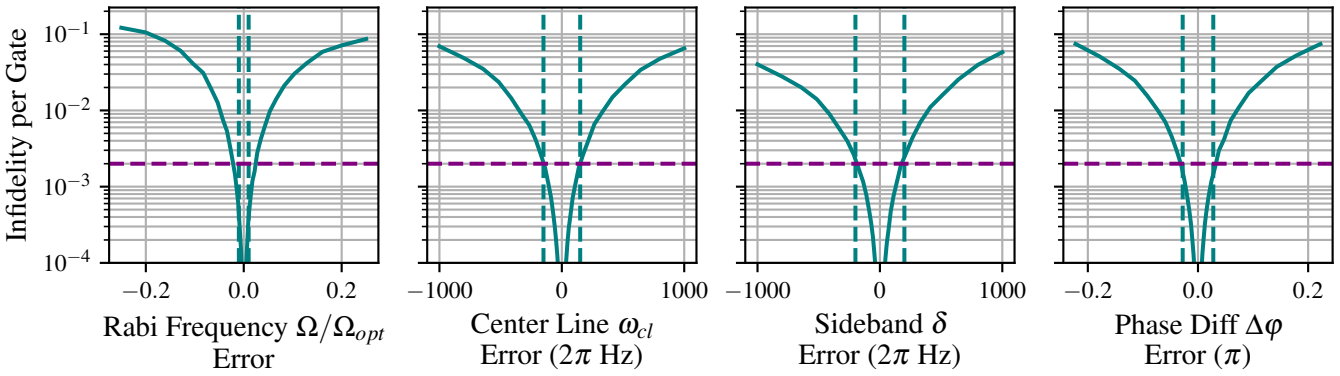

Figure 5.8: SIMULATED EXPECTED RANDOMIZED BENCHMARKING INFIDELITY. The infidelity is plotted as function of individual parameter miscalibrations for a $100\mu s$ gate. These curves inform the choice of target thresholds (cyan dashed lines), an infidelity of $2 \cdot 10^{-3}$ (purple dashed line) for each parameter has been chosen as a threshold. The fixed parameters were kept at $\Omega = \Omega_{opt}$, $\omega_{cl} = 0$, $\delta = 10 \cdot 2\pi$kHz, $\Delta\phi = 0$.

5.4 SELECTION OF MEASUREMENT SETTINGS

The framework discussed in Section 5.2 describes how to process the measurement obtained by an experiment, but there is no guarantee that this will lead to a reduction in uncertainty. This problem can be mitigated by performing different experiments, in this case we have a choice of the sequence of gates for which we want to perform a measurement. Different gate sequences have different dependencies on the modeled gate parameters. As an extreme example, a single gate has no dependency on the phase difference $\Delta\varphi$ between subsequent gates, thus a measurement of a single gate cannot provide any information about that parameter and thus will not reduce its uncertainty. A successful tuneup routine thus requires a strategy for selecting suitable measurement settings that ideally maximize the amount of information gained from performing a measurement using the selected gate sequence.

We restrict our considerations for possible experiments to sequences of MS gates without any local operations. Besides the number of gates N_g we can also intentionally introduce a phase difference $\Delta\varphi_{target}$ between the gates. We restrict the phase difference settings to either $\Delta\varphi_{target} = 0$ or $\Delta\varphi_{target} = \pm\pi/4$, corresponding to either consecutive $\mathrm{MS}_0(\frac{\pi}{2})$ gates or a sequence of $\mathrm{MS}_0(\frac{\pi}{2})\,\mathrm{MS}_{\pm\frac{\pi}{4}}(\frac{\pi}{2})\ldots\mathrm{MS}_{\pm(N_g-1)\frac{\pi}{4}}(\frac{\pi}{2})$ gates. We chose these two types of sequences as they change which parameters the sequence is most sensitive to as can be seen in Fig. 5.9. The model outcome probabilities for two selected sequences are shown here, with the slope of the probabilities determining the sensitivity to a parameter.

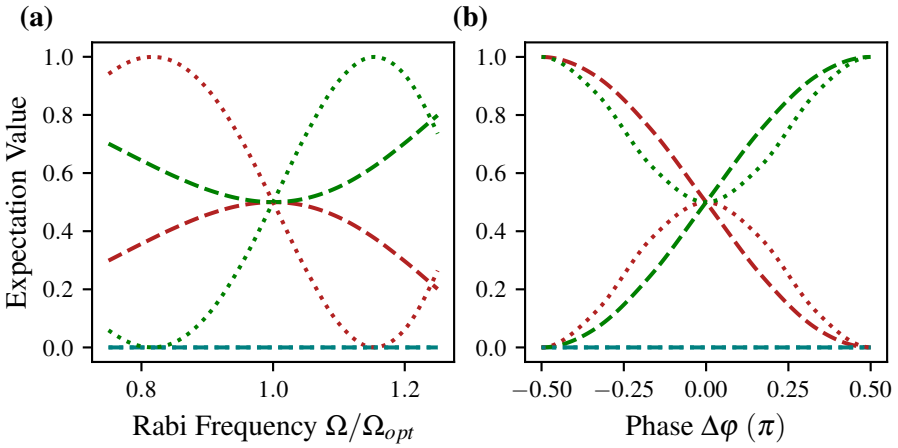

Figure 5.9: Expected outcome probabilities of $P(|g,g\rangle)$ (green), $P(|e,e\rangle)$ (red) and $P(|e,g\rangle) + P(|g,e\rangle)$ (blue) for a 3 gate sequence (dotted, 3 $\mathrm{MS}_0(\frac{\pi}{2})$) and for a 2 gate sequence (dashed, $\mathrm{MS}_0(\frac{\pi}{2})\mathrm{MS}_{\frac{\pi}{4}}(\frac{\pi}{2})$). The 2 gate sequence is first-order insensitive to Rabi frequency miscalibrations as can be seen in figure (a) due to the local minimum of the outcome probabilities around zero which leads to only small variations in the likelihood of possible outcomes, and its symmetry around zero does not allow us to discriminate the sign of the miscalibration. The same argument can be used to see in figure (b) that this sequence is first-order-sensitive to phase difference miscalibrations. For the second gate sequence the relation is inverted, being sensitive to Rabi frequency miscalibrations at the cost of first-order-insensitivity to the phase difference. The qualitative behaviour of the sensitivity of the center line matches the sensitivity of the phase difference, while the behaviour of the sideband detuning matches the Rabi frequency.

Applying more gates increases the sensitivity of the sequence as the features of the likelihood function $P(m|\boldsymbol{\Theta})$ become narrower, resulting in an increased first-order sensitivity to miscalibrations. At the same time, the peaks of the likelihood function become more closely spaced. This can lead to issues as a wide prior may cover several of these peaks, resulting in a multi-modal posterior distribution which causes slow convergence. Additionally, the effect of unmodelled error sources such as decoherence increases with the number of additional gates, limiting the total length of the sequence used in the optimization. The goal of the measurement strategy is thus for each step to choose the number of gates N_g applied, as well as the targeted phase difference between consecutive gates.

In the following two approaches for a measurement strategy are presented.

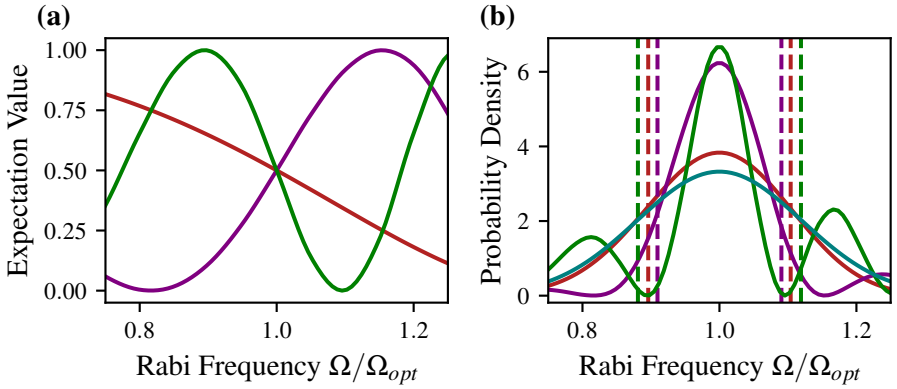

Figure 5.10: ILLUSTRATION OF THE DECISION-MAKING PROCESS FOR THE VARIANCE MINIMIZATION STRATEGY. Figure (a) shows the expected outcome probability $P(|g,g\rangle)$ for the $|g,g\rangle$ state according to the model for each setting ($N_g = 1$ red, $N_g = 3$ purple, $N_g = 5$ green with $\Delta\varphi_{target} = 0$) depending on the Rabi frequency Ω. In this case the outcome probability for $P(|e,e\rangle) = 1 - P(|g,g\rangle)$ with population in the remaining states being zero. Figure (b) illustrates the variance minimization strategy for the prior given in cyan and the expected posterior probability distributions calculated using the expected outcomes. We compare the standard deviations (dashed lines) of the expected posteriors for each setting under consideration ($N_g = 1$ red, $N_g = 3$ purple, $N_g = 5$ green with $\Delta\varphi_{target} = 0$) to select the smallest for next measurement setting. In this example the deviation for 3 gates is the narrowest and is thus chosen.

5.4.1 *Variance Minimization Strategy*

To maximize the information gain from a measurement, we want to perform a measurement that is expected to decrease the variance of our posterior distribution as much as possible. This can be accomplished by the strategy shown in Algorithm 5.2 described in the following: For each measurement setting s we can predict the posterior estimate $\overline{\boldsymbol{\Theta}}_{m_j,s}$ and variance $\mathrm{Var}(\boldsymbol{\Theta}_{m_j,s})$ for each measurement outcome m_j by first calculating the weights for each possible outcome of the measurement with Eq. (5.13) using the corresponding probabilities $P_s(m, \boldsymbol{\Theta})$

$$\overline{\boldsymbol{\Theta}}_{m_j,s} = \sum_{i=1}^{N_p} \boldsymbol{\Theta}_i P_s(m_j|\boldsymbol{\Theta}_i) w^{(i)}, \tag{5.17}$$

$$\mathrm{Var}(\boldsymbol{\Theta}_{m_j,s}) = \sum_{i=1}^{N_p} (\boldsymbol{\Theta}_i - \overline{\boldsymbol{\Theta}}_{m_j,s})^2 P_s(m_j|\boldsymbol{\Theta}_i) w^{(i)}. \tag{5.18}$$

We can estimate the total probability of an outcome by averaging over the particle filter

$$P_s(m_j) = \sum_{i=1}^{N_p} P_s(m_j|\mathbf{\Theta}_i)w^{(i)}. \tag{5.19}$$

By weighing the variance with the expected probability for that outcome we can calculate the most likely variance $\mathrm{Var}(\mathbf{\Theta}_s)$ for a given measurement setting given the current knowledge before actually measuring,

$$\mathrm{Var}(\mathbf{\Theta}_s) = \sum_j \mathrm{Var}(\mathbf{\Theta}_{m_j,s})\langle m_{j,s}\rangle. \tag{5.20}$$

We aim to minimize our variance to improve the estimate of all our parameters, however different measurement settings do not affect all parameters equally. For different parameters, there may be a different optimal setting with the lowest predicted variance. We thus employ a heuristic to calculate a score for each measurement setting for which we normalize each variance with its target threshold T_Θ defined in Section 5.3 and sum up all the normalized variances to get a score X_s for the measurement setting

$$X_s = \sum_\Theta \frac{\mathrm{Var}(\Theta_s)}{T_\Theta^2}. \tag{5.21}$$

We then apply the measurement setting with the lowest score to the experiment. The process is illustrated for 1 dimension in Fig. 5.10.

We need to calculate the outcome probabilities at each particle location for each measurement setting, which is computationally expensive. We interpolate probabilities from precomputed simulations to speedup this calculation, but the interpolation remains the most time consuming operation in our classical computations. While calculating the probabilities is an unavoidable step for performing the Bayesian update of the particle filter as discussed in Section 5.2.2, predicting the variances requires running this calculation for each measurement setting under consideration. This significantly increases the total classical computational overhead.

Algorithm 5.2 : Variance Minimization Strategy

INPUT : A particle filter $\mathbf{\Theta}_i, w^{(i)}$,
A list of measurement settings s
OUTPUT : A measurement setting s_{opt}

BEGIN
  FOREACH setting s DO
    Compute outcome probabilities $P_s(m_j, \mathbf{\Theta}_i)$
    Compute variance $\text{Var}(\mathbf{\Theta}_{m_j,s})$ for each outcome m_j.
    Average $\text{Var}(\mathbf{\Theta}_{m_j,s})$ by total probability $P_s(m_j)$ for an outcome.
  END
  Score variances $\text{Var}(\mathbf{\Theta}_s)$ by normalizing each parameter by its target treshold T_Θ.
  Select setting s_{opt} with the lowest score
END

5.4.2 *Thresholded Strategy*

While the previous strategy tries to minimize the number of measurements required, it does not account for the time required to choose that measurement setting. The strategy thus does not necessarily minimize the total run time of a calibration run, which affects the total fraction of time a quantum processor requires for calibration tasks. While it would be possible to decouple the processing and measurements and schedule other experiments during the evaluation time, it is much preferable if the processing time was not the limiting factor for the Mølmer-Sørensen gate calibration routine.

In order to find an alternative we want to look at which settings are considered optimal by the Variance Minimization strategy, and try to find a less expensive way to identify these settings. In practice this strategy means selecting the setting that uses the most gates while avoiding a multi-modal posterior distribution. These multi-modal posteriors are caused by the likelihood function having two maxima over the range of the prior. To avoid them, ideally the chosen measurement settings would yield outcome probabilities that have only one likely parameter value. While it is impossible to simultaneously fulfill this for all parameters, we can still attempt to limit the amount of possible maxima of the likelihood function with the right choice of measurement setting. To accomplish this, we want to impose a requirement on the maximal width of the prior before using a specific measurement settings.

We examine the expected outcomes of the model restricted to one dimension for each parameter and for each experimental setting, while the other parameters are set to their optimal values. We then choose the local extremum closest but not equal to the optimal value in the

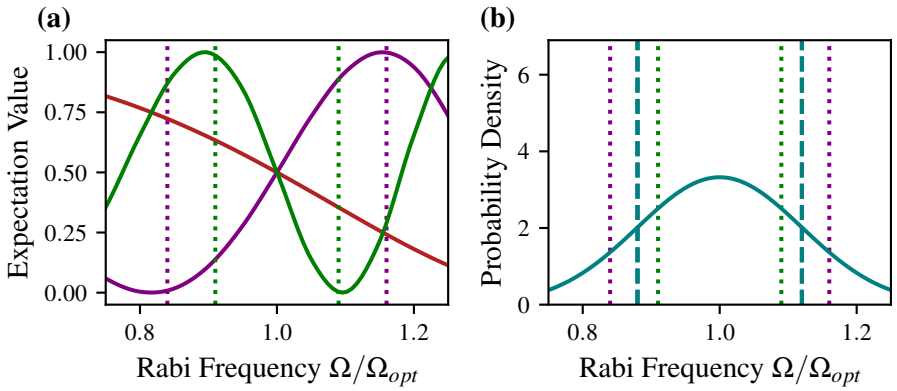

Figure 5.11: Illustration of the decision-making process for the thresholded strategy. The figure (a) shows the expected outcome probability $P(|g,g\rangle)$ for the $|g,g\rangle$ state according to the model for each setting ($N_g = 1$ red, $N_g = 3$ purple, $N_g = 5$ green with $\Delta\varphi_{target} = 0$) depending on the Rabi frequency Ω. In this case the outcome probability for $P(|e,e\rangle) = 1 - P(|g,g\rangle)$ with population in the remaining states being zero. The dotted lines show the thresholds used for the thresholded strategy, aligned with the local extrema of the expected outcome probabilities. In the right figure (b) these thresholds are used to evaluate the prior. We only consider the standard deviation of the prior (dashed lines), with the width of the prior being larger than the 5 gate threshold (green) but below the 3 gate threshold (purple), leading to the 3 gate setting being chosen. The single gate setting does not have any thresholds, being the fallback option if no other setting passes the thresholds.

outcome probabilities, and define a threshold as the distance of the extremum to the center for each measurement setting. While this ignores possible correlations of the probability distribution between the parameters, we have found in practice that these thresholds are already sufficient to avoid multi-modal posteriors.

We split the settings into first-order Rabi frequency Ω sensitive settings and into first-order phase difference $\Delta\varphi$ sensitive settings depending on whether the $|e,e\rangle$ and $|g,g\rangle$ populations have a local extremum exactly at the optimal parameter value or a linear slope in either phase or Rabi frequency respectively as can be seen for the outcome probabilities of two example sequences in Fig. 5.9.

These thresholds are now used to for the measurement strategy described in Algorithm 5.3 that will be used by the calibration algorithm: On each iteration we alternate between selecting from either Rabi frequency or phase first-order-sensitive settings, comparing the defined thresholds to the current variances to ensure that the variance of both Rabi frequency Ω and phase difference $\Delta\varphi$ are being improved. We now compare the variance of our prior with the thresholds, and

Algorithm 5.3 : Thresholded Strategy

INPUT : A particle filter $\mathbf{\Theta}_i, w^{(i)}$,
A sorted list of Rabi frequency sensitive settings s_A with thresholds $t_{s,A}$
A sorted list of phase difference sensitive settings s_B with thresholds $t_{s,B}$
OUTPUT : A measurement setting s_{opt}

```
BEGIN
    Calculate current mean and variance Θ̄Var(Θ)
    IF Last step used s_A settings THEN
        Use phase difference sensitive settings s_B
    ELSE
        Use Rabi frequency sensitive settings s_A
    END
    FOREACH setting s DO
        IF Var(Θ) < t_s for all parameters Θ THEN
            RETURN setting s as s_opt
        END
    END
END
```

discard any setting for which the variance exceeds a threshold in any parameter. Among the remaining settings we pick the setting with the highest number of MS gates (For an example see Fig. 5.11). This gives us a way to select measurement settings while avoiding the computational overhead incurred by the Variance Minimization strategy, with the time needed to evaluate the strategy ($\ll$ 1ms) being negligible compared to the time required to update the particle filter (Section 5.2.2).

5.5 RUN TIME OF THE ALGORITHM

A single experimental shot only takes ≈ 10 ms, while computing the particle filter update requires $\approx 100 - 500$ms. To balance the classical computational effort for updating the particle filter and the latency in updating the control system with the duration of the experiment, we run 100 experimental cycles with the same measurement setting before updating the particle filter and choosing the next experimental setting. The variance minimization strategy additionally needs time ($\approx 0.6 - 3$ s) for selection of the next measurement setting, while the time required to evaluate the thresholded strategy is negligible.

In Fig. 5.12 (a) we show the number of individual experiments required to reach the target thresholds, giving a comparable number of experimental shots for the variance minimization strategy (1200 ± 500 shots) and the thresholded strategy (1100 ± 500 shots). Fig. 5.13 (a)

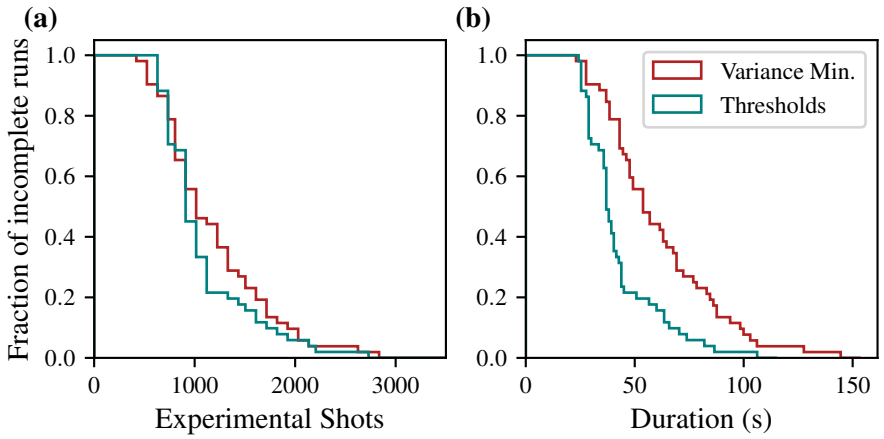

Figure 5.12: The number of experimental cycles required to reach the target thresholds is shown as a fraction of all runs in (a). The thresholded strategy takes 1100 ± 500 cycles on average compared to 1200 ± 500 for the variance minimization strategy. The total time required is show in (b), where the thresholded strategy takes $42 \pm 17s$ cycles while the variance minimization strategy requires $60 \pm 26s$.

and (b) display the measurement settings used during these calibration runs. The variance minimization strategy focuses on either the phase or the Rabi frequency sensitive setting, trying to reduce the largest variance component before switching. The thresholded strategy instead alternates between the settings of different sensitivity. Both settings increase the number of gates on later iterations as the variances decrease. While the order of which measurement setting is chosen is different between the strategies, the number of experimental shots required is comparable.

From this we can conclude that the thresholded strategy is a competitive heuristic to select measurement settings compared to the variance minimization strategy.

Fig. 5.12 (b) shows the distribution with the computational overhead taken into account. Here the thresholded strategy has the advantage, completing with average run time of 41 ± 17 s compared to an average of 60 ± 26 s for the variance optimization. Averaged over both strategies we find that we require 1200 ± 500 experimental shots to reach our target thresholds. A strict quantitative comparison to all other possible optimization strategies is difficult to define. Using our Bayesian algorithm we achieve a significant speedup compared to manual iteration over 1D parameter scans as defined in Akerman et al. [136]. Simulations of 1D parameter scans achieve worse residual infidelities, while requiring significantly more measurements. This comparison is fully discussed in Appendix A.

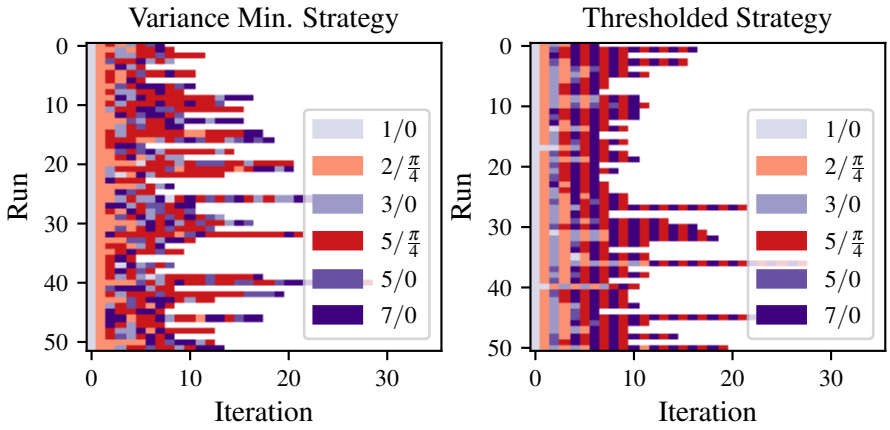

Figure 5.13: MEASUREMENT SETTINGS USED DURING THE CALIBRATION RUNS FOR THE TWO STRATEGIES. The y axis corresponds to independent runs and the x axis to iterations of the algorithm during a calibration run, at each iteration 100 measurements were performed with the chosen setting. The colors indicate the measurement setting used at a given iteration of a run, characterized by the number of gates N_g (first number in the legend) and the selected phase difference $\Delta\varphi_{target}$ (second number) used for the gate sequence.

5.6 CAPTURE RANGE & PARTICLE NUMBER

Any Bayesian procedure requires a choice of an initial prior, where in our case we consider normal distributions. It is reasonable that if the true values are unlikely given our initial prior, that is, if the true values are too far away from the center of our initial prior, then the routine will fail to converge to them. In this section we will study the dependence of the failure rate of our algorithm on this initial distance in parameter space. We will also study the dependence of the success rate of the algorithm on the number of particles in the particle filter, since a larger number of particles allows for a more accurate sampling and, therefore, a better approximation of the probability distributions under study. This increase in the number of particles comes with the cost of a linear growth in the classical computing time required by the algorithm.

To be able to compare parameters with different units we study these effects by first obtaining a normalized distance, D_{start}, of the initial values of the parameters from their target values using the widths of the prior

$$D^2_{start} = \sum_{\Theta} \frac{(\Theta_{start} - \Theta_{opt})^2}{\sigma^2_\Theta} \tag{5.22}$$

with σ^2_Θ being the initial variance of the prior projected onto parameter Θ, with the starting value Θ_{start} and Θ_{opt} the optimal value for that parameter.

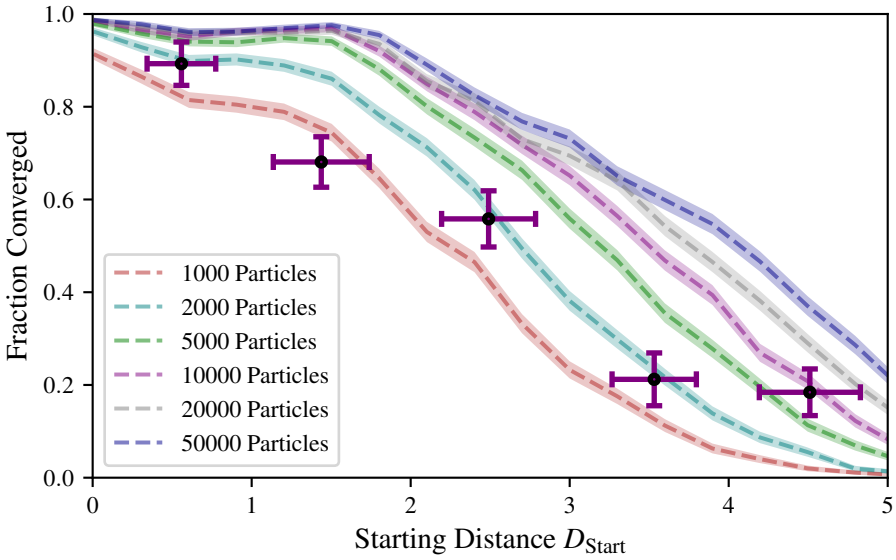

Figure 5.14: CAPTURE RANGE OF THE ALGORITHM. The width of the initial Gaussian prior has been held constant at $\sigma_\Omega = 0.2 \cdot \Omega_{opt}$ Rabi frequency uncertainty, $\sigma_\delta = 1 \cdot 2\pi$kHz sideband uncertainty, $\sigma_{\omega_{cl}} = 1 \cdot 2\pi$kHz center line uncertainty and $\sigma_{\Delta\varphi} = 0.33\pi$ phase uncertainty. The starting distance has been calculated using Eq. (5.22). The fraction captured represents the number of runs that terminate within two times the target thresholds of the optimal parameter values. For each distance, 2000 tuneups were run. The shaded area corresponds to one standard deviation. For 10000 particles we additionally measured the capture range experimentally, where the results are represented with purple squares. The error bars correspond to the statistical deviation of the data points.

We generate random combinations of initial gate time, center line frequency and sideband frequency with the chosen starting distance and then run simulated calibration runs. The phase was not varied as the space is periodic, and thus limits how far the phase values can be from the optimal value. The fraction of calibration runs that converged is shown in Fig. 5.14, where we consider any run that ends up closer than twice the termination thresholds of the stopping criterion (Section 5.3) in all parameters a success. Since for each parameter the estimated error is below the threshold, for a Gaussian distribution at least 95% of results should be between these thresholds. Due to the statistical nature we do not expect a perfect success rate even if the particle filter were to perfectly approximate the continuous probability function.

We find that for 2000 particles and less in the particle filter the capture range is reduced as compared to the higher particle numbers, and performance is decreased even at starting distance of 1 compared to the higher particle numbers. This is expected as a particle filter with too few particles will lead to an undersampling of the probability

distribution, which in turn results in a poor approximation of this probability distribution. As a consequence, discretisation artifacts will appear, such as the particle filtering not being able to track the peaks of the distribution well enough.

We choose 10000 particles as our default value to work with since in simulation the gains for using more than 5000 particles decrease significantly.

Experimentally, we find a reduction of 10-25% of the success rate compared to the simulations using the same sample size for starting distances < 2 due to effects not included in the model affecting the algorithm. For larger distances, the success rate is comparable between experiment and simulation. While we are unable to pin down the exact cause of failures, we hypothesize that these events may be due to transients in the control fields.

These effects may lead to a difference between our estimated likelihoods and the true ones, which then suppress the posterior probability distribution around the true values. This can then shift the parameter estimates away from the true values, but also lead to underestimating the variances compared to the true error. The algorithm might then use unsuitable measurement settings, or prematurely terminate if the variances are small enough to fulfill the stopping criterion. These effects can then lead to a final parameter estimates of the algorithm far from the ideal values.

5.7 CONFIRMATION MEASUREMENTS

To use the calibration algorithm even with less than perfect success rate, we insert confirmation measurements after completing the procedure to detect and then reject outliers in the final gate parameters predicted by the algorithm. For rejected calibration runs the algorithm can then be repeated.

To detect outliers, we employ check sequences. We choose a sequence of 8 consecutive $\mathrm{MS}_0(\frac{\pi}{2})$ gates and a sequence of 6 gates with $\Delta\varphi_{target} = \pm\frac{\pi}{4}$ which both ideally return all populations to the ground state. The sequences are chosen because they are sensitive to Rabi frequency or phase difference miscalibrations, respectively. We choose an acceptance threshold of at least 85 out of 100 measurements being in the target state. This threshold was chosen as a compromise between acceptance rate and the fidelity of the accepted runs, as more stringent thresholds start decreasing acceptance rate without significant improvements of either maximum or median infidelity of accepted runs. We run repeated calibration runs including confirmation measurements and record the final parameter estimates produced by the calibration runs. These values are plotted in Fig. 5.15, with the runs that fail the confirmation tests marked in red. 95(2)% of runs pass the confirmation test. The distribution of accepted runs has

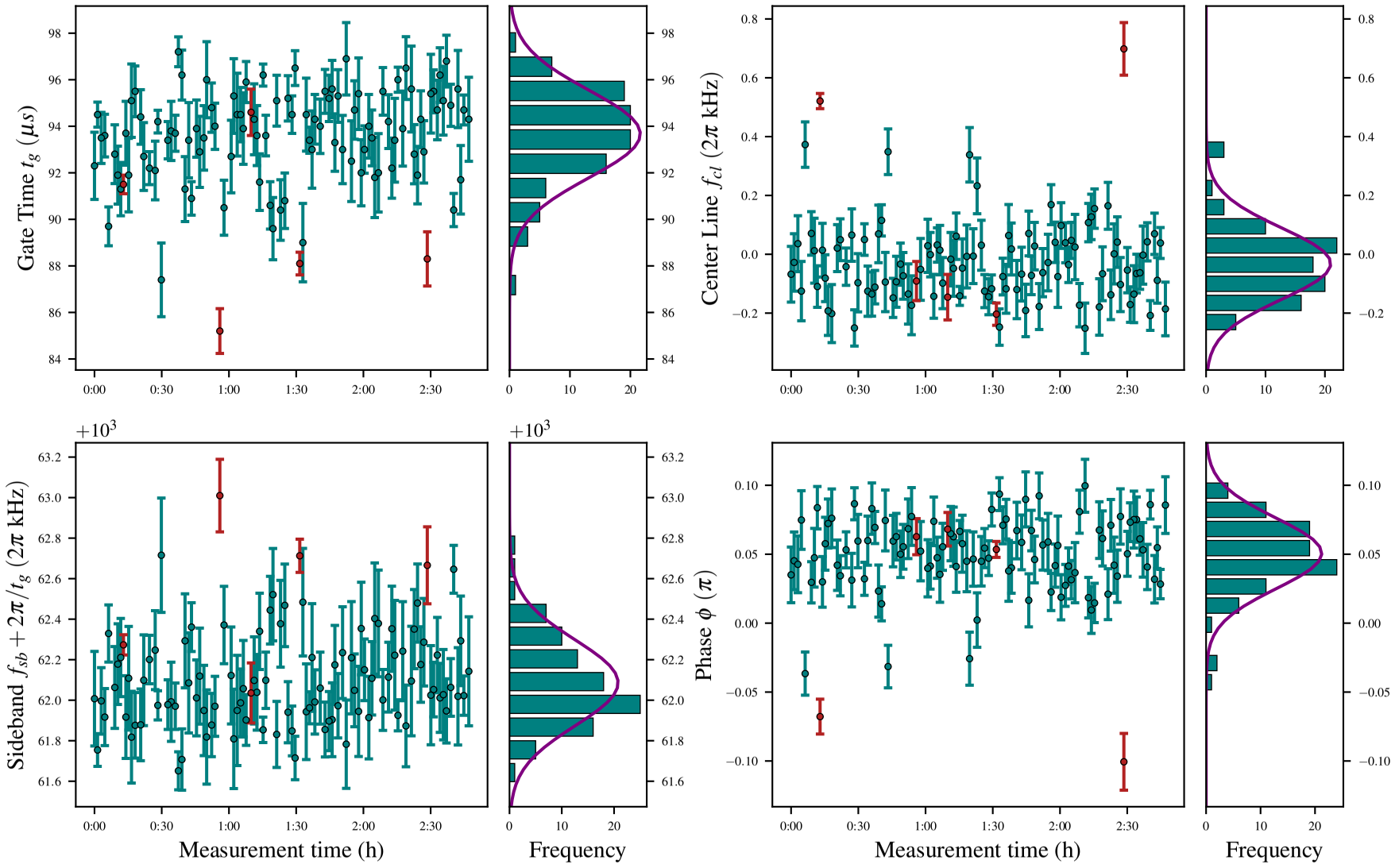

Figure 5.15: Final parameter estimates and uncertainties. 103 independent iterations of tuning up the Mølmer-Sørensen gate are shown versus time elapsed. The red points are runs rejected by the confirmation criterion described in Section 5.7, corresponding to 5(2)% of all runs. Removing the rejected points reduces the standard deviation of the distributions of final parameter estimates between 13-20%. Purple curves show a Gaussian distribution fitted to a histogram the distribution of final parameter values.

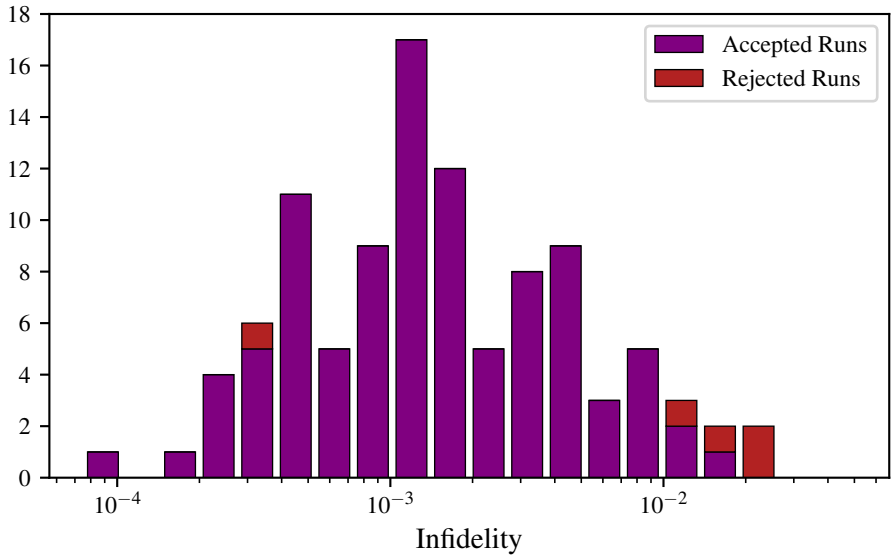

Figure 5.16: HISTOGRAM OF GATE INFIDELITIES DUE TO IMPERFECT CALIBRATION. Randomized benchmarking is used to compute a per-gate infidelity from the difference of the final parameter estimates of independent calibration runs compared to their mean value (Fig. 5.15). We calculate a median infidelity of $1.3(1) \cdot 10^{-3}$ caused by imperfect calibration and a 95 percentile of $7.4 \cdot 10^{-3}$.

standard deviations of $\sigma_{t_g} = 1.9(1)\mu s$, $\sigma_{f_{cl}} = 0.12(1) \cdot 2\pi kHz$, $\sigma_{f_{sb}} = 0.21(2) \cdot 2\pi kHz$, $\sigma_\phi = 0.025(3) \cdot \pi$. Translating these deviations to the gate parameters $\boldsymbol{\Theta}$ we find they are in agreement or below the thresholds set in Section 5.3.

We evaluate the estimated infidelity due to imperfect calibration of the accepted runs of the algorithm by simulating randomized cycle benchmarking using the difference between the final parameter estimates and the mean of all accepted calibration runs as miscalibration, and calculate the expected infidelity due to calibration error. The distribution of these expected infidelities is shown in Fig. 5.16. We achieve´ a median calibration infidelity of $1.3(1) \cdot 10^{-3}$. This value is lower than what was calculated for independent errors in Section 5.3, which we attribute to the correlations between the parameters partially compensating each other. We can compare this to the fidelity of Bell states [32, 137] generated by repeated application of the MS gate on the same system, and find that the infidelity per gate is measured to be $4(1) \cdot 10^{-3}$. While this state fidelity is not suited to characterize the effects of coherent errors, it does pose a limit on the achievable fidelity due to incoherent errors present in the system. We expect laser phase noise and dephasing of the motional mode as the leading sources of decoherence. From this infidelity we conclude that our calibration routine can produce parameter estimates such that our entangling gates are not limited by calibration errors, but limited by the performance of the machine.

In conclusion, the algorithm can be used to calibrate a gate to a median residual infidelity due to parameter miscalibration of $1.3(1) \cdot 10^{-3}$ (Fig. 5.16) in 1200 ± 500 experimental shots, achieving a significant speedup over manually iterating over 1D parameter scans (See Appendix A for an estimate on the capabilities of the 1D parameter scan method). These results demonstrate the suitability of the described approach to reliably and consistently calibrate a set of control parameters to achieve a gate fidelity that is limited by incoherent processes in the quantum system. Our approach considerably eases the operational burden and can produce valuable time savings for the operating experimentalist. Furthermore, periodic re-calibration can be included within long experimental data-taking sequences, protecting against slow parameter drifts, and thus guaranteeing high quality output over considerably longer time.

6

LIGHT-SHIFT GATES

In this chapter we present the results of our entangling gate operations using light-shift gates on ions where the quantum information is encoded in states separated by optical transitions as proposed by Sawyer and Brown [138].

We investigate two different applications of this gate scheme in this chapter. The first application is generating entanglement between different species of ions, which is of interest for quantum communications, to use a species as quantum memory, or for a partial readout of a quantum register while protecting the other qubits.

The second application is the extension of the gate scheme to operate on a qudit which encodes information in more than two levels per ions instead of a two-level qubit. These higher-dimensional quantum systems hold promise as a powerful resource for quantum computation and simulation [139] (Section 2.3). We demonstrate how the gate is utilized to generate entanglement between two qudits state, and we discuss the results of the experimental implementation.

6.0.1 *Gate Mechanism*

The light-shift gate utilizes the coupling of electronic states to a mode of motion via a Raman type interaction to create entanglement, where the Hamiltonian of this interaction has been previously discussed in Section 3.5.5. This interaction requires two laser beams with a relative detuning, which create a standing wave.

The coupling strength of the light fields to the motion is governed by the Lamb-Dicke factor, which in turn depends on the geometry of the beams, in particular on the overlap of the wave vector of the light field with the mode of motion.

For the standing wave the effective wave vector is given by the difference of the k-vectors of the individual light fields of the two beams. The beam geometry is illustrated in Fig. 6.1: We use a pair of beams at a 90° angle to each other to generate the standing wave pattern, with the two beams at 45° to the trap axis. The wave vector is then aligned with the axial modes of motion. The polarization of the two beams influences the kind of standing wave that is created. For a choice of polarizations such as $\sigma^{\mp}$, $\sigma^{\pm}$ with two opposite cir-

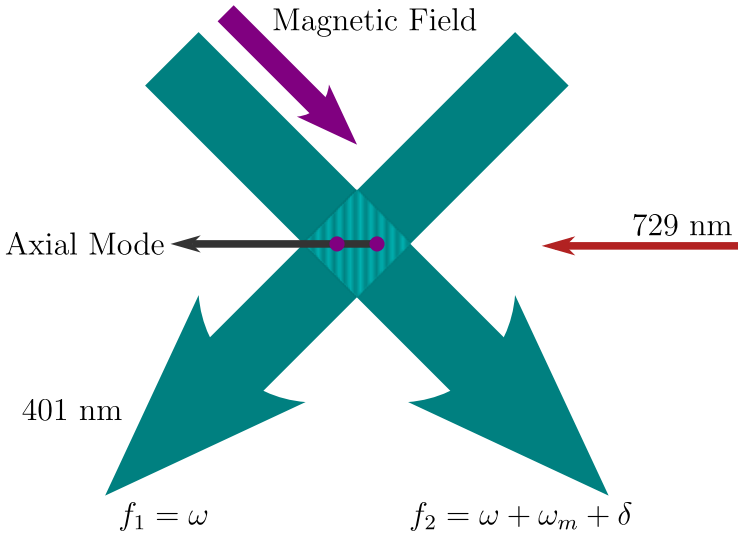

Figure 6.1: BEAM GEOMETRY USED FOR LIGHT-SHIFT GATES. Two beams at a wavelength of $\lambda = 401$nm are intersecting at a 90° angle to generate a standing wave pattern that drives a spin-dependent force.

cularly polarized beams a standing wave with spatially-modulated polarization is generated. In contrast if the polarizations align such as for a pair of parallel linearly (π) polarized beams, the amplitude is modulated. These two kinds of standing wave are depicted in Fig. 6.2. We utilize an intensity-modulated field to generate the optical dipole forces, the strength of the gate interaction is maximized for a pair of beams linearly polarized orthogonal to the k-vector [138].

6.0.2 *Calibration of the Beam Alignment*

The Raman beams are aligned with the ions by means of a Stark shift measurement. For this purpose a Ramsey type experiment with a spin-echo pulse is set up using the quadrupole laser with a duration for which the visibility is still high, typically 1 ms. Then, a pulse from one of the Raman beams is applied during one half of the spin-echo experiment, introducing a phase shift. We measure periodic oscillations as a function of the pulse duration. On this signal the alignment of the beam to the ions can be optimized with the goal of maximizing the oscillation frequency. Once a phase shift close to π is achieved, the probe duration is reduced to remove any disambiguity if the frequency is increasing or decreasing. This procedure is then iterated until the coupling can no longer be improved. As we are measuring the combined signal of both ions, a small difference in coupling strength manifests in a reduction of the contrast of the mean excitation of both ions. To remove this difference the coupling to the two ions is further balanced by choosing a probe time corresponding

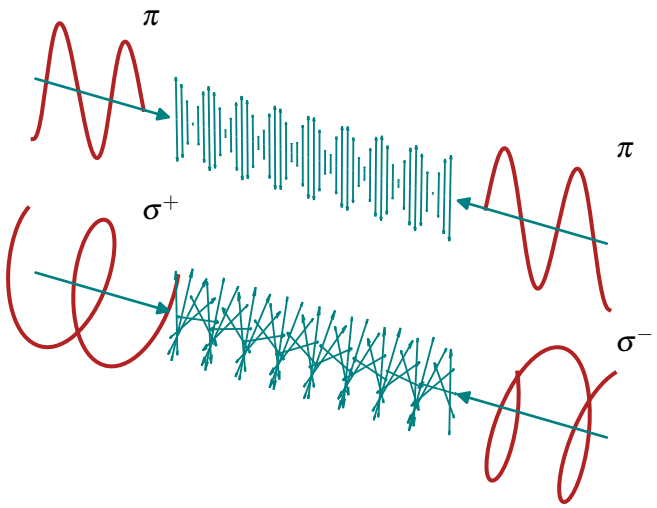

Figure 6.2: STANDING WAVE FOR DIFFERENT POLARIZATION CONFIGURATIONS. The top case shows a wave with spatially modulated amplitude generated by a pair of linearly polarized beams, the bottom case shows a wave with spatially modulated polarization generated by a pair of beams with opposite circular polarization.

to a phase shift of an integer multiple of π. As small adjustments here lead to an increase of coupling on one ion while reducing it for the other, minimizing respectively maximizing the excitation balances the strength on both ions. For this we change the beam alignment in the plane of the axial mode only. This procedure is performed for both beams independently.

6.0.3 *Calibration of the Ion Spacing*

The entangling gate relies on different spin states receiving different phases. The phase imparted on the states (Eq. (3.70)) depends on the position of the ions with respect to the standing wave pattern. A gate can be performed for any value of phase difference except for the special case where the shift on the odd states ($|eg\rangle$, $|ge\rangle$) exactly equals the shift on the even states ($|gg\rangle$, $|ee\rangle$) but doing so may not be efficient. To minimize the required laser power for a fixed gate duration or the achievable gate duration for a fixed available power, the spacing of the ions needs to be adjusted to maximize the phase difference when driving the gate on either the center-of-mass (COM) or the out-of-phase (OOP) mode, corresponding to a half-integer or an integer multiple of the wavelength of the standing wave, respectively.

This can be calibrated by minimizing the excitation when resonantly driving the blue sideband transition while in the electronic ground state $|gg\rangle$. Here the detuning between the two Raman beams is set equal to the mode frequency, exciting a coherent motional state. The

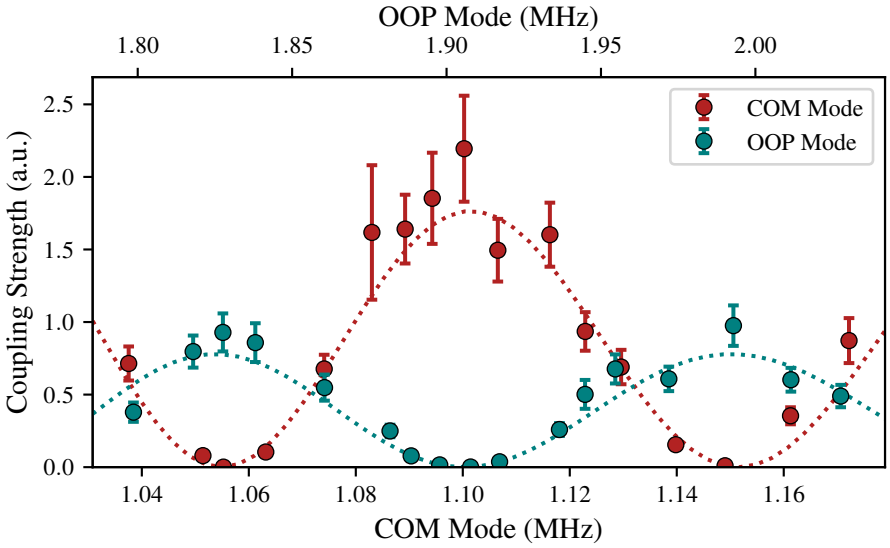

Figure 6.3: Coupling strength as function of the axial modes of a two-ion $^{40}Ca^{+}$ crystal. The two horizontal axes give the mode frequencies for the two axial modes, the center-of-mass (COM) and the out-of-phase (OOP), of the ion crystal at the same axial confinement. The fit corresponds to the expected ion spacing from the trap frequency for a harmonic potential, with an offset of the trap frequency that can be explained through a static quadrupole component on the order of $2 \cdot 10^{16} \mathrm{V/m}^4$.

phonon state is then read out by driving a red sideband transition using the 729nm laser. As the transition is suppressed for the motional ground state we get a signal that depends on the motional state. Minimizing the coupling to the blue sideband transition maximizes the phase difference for applying the gate. Figure 6.3 shows the coupling strength of the Raman laser to the two axial modes of motion of a two-ion crystal. By adjusting the confinement of the ion crystal the spacing of the ions can be controlled to find an optimum that maximizes the phase difference when driving the gate on the chosen mode.

6.1 MIXED SPECIES GATES

Mixed species gates promise to combine the advantages of different atomic species while avoiding their individual shortcomings. One well-explored technique is quantum logic spectroscopy [140], where a secondary species is used to interrogate an atom without a feasible closed cooling transition. Here the secondary species is used not only to sympathetically cool the ion of interest [141, 142], but also to map its state onto the secondary species for readout.

For quantum computation one might also wish to combine two species. A species with long coherence times could act as a memory

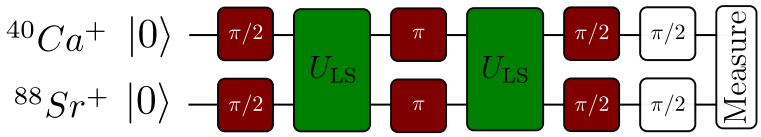

Figure 6.4: Pulse scheme for the mixed species gate. The light-shift interaction U_{LS} pulses are interleaved with a spin-echo sequence. The final $\pi/2$ pulses are used for the parity measurements only.

ion, while a species with high detection fidelity could be used for readout [143].

Another aspect is quantum error correction, which will be essential for large-scale quantum computation. The correction step in an error correction cycle makes critical use of the partial readout of the quantum register, while preserving the information stored in the remaining register. For a single species photons scattered can be reabsorbed by other ions in the part of the register that should remain unperturbed, causing additional errors. Using a secondary species however allows us to detect the state without the readout introducing additional errors caused by absorption, as the transition frequencies of the two species are spectrally well separated [144].

Mixed species gates can also find applications in quantum communication and remote entanglement generation [145]. There it can be advantageous to choose a secondary species to generate photons as flying qubits due to the differences in performance of optics, detectors and optical fibers available at different wavelengths.

6.1.1 *Gate implementation and measurements*

The implementation of the mixed species light-shift gate has been performed on a two-ion ^{40}Ca$^+$-^{88}Sr$^+$crystal, where we implement a $\sigma_z\sigma_z$ light-shift gate on the qubits encoded between the respective $S_{1/2}$ and $D_{5/2}$ states.

The required single qubit rotations are performed using the resonant 729nm and the 674nm lasers, while the entangling interaction as described in Eq. (3.65) is generated by the pair of Raman beams that drive the gate on the axial COM mode. The crystal is initially Doppler-cooled by simultaneous illumination from the ^{40}Ca$^+$and ^{88}Sr$^+$cooling beams. This is then followed by sideband cooling of the calcium ion using the 729nm and 854nm laser, preparing the ions in the motional ground state.

The ions do experience unwanted single-qubit phase shifts due to the Raman beams. These shifts can be canceled by performing two loops in the motional phase space, while inserting π pulses on both ions between the two loops to swap the populations between the $|ee\rangle$ and $|gg\rangle$ state, with the pulse sequence being shown in Fig. 6.4. This

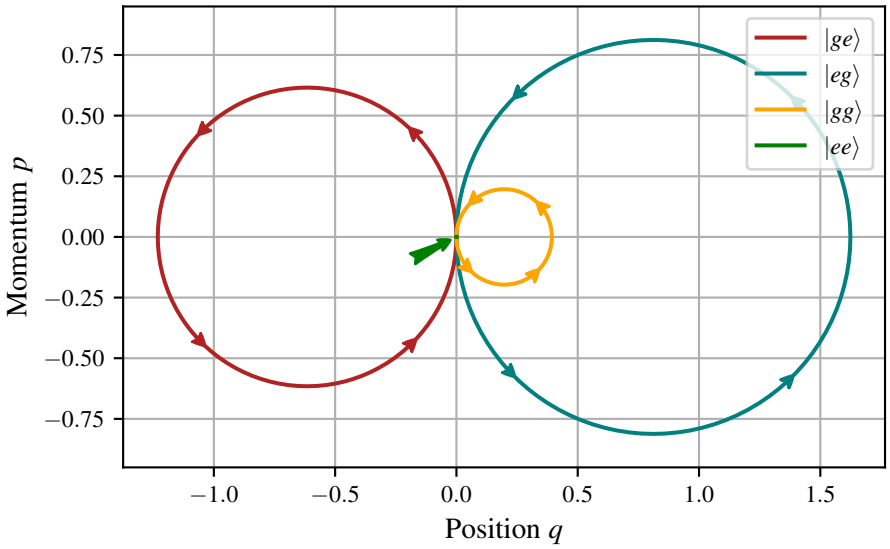

Figure 6.5: Loops in phase space for the mixed-species gate. The excursion for 4 different states are shown, the encoding is referring in order to $^{40}Ca^{+}$-$^{88}Sr^{+}$. For $|ee\rangle$ the enclosed phase is negligible due to the large detuning from the states, while $|gg\rangle$ cannot be perfectly nulled due to the unequal coupling to the two species. This also causes the difference between $|eg\rangle$ and $|ge\rangle$, requiring the use of spin echo pulses for symmetrization.

also symmetrizes the phase shifts experienced by the $|e,g\rangle$ and $|g,e\rangle$ states, without having to tune the wavelength of the Ti:Sa laser system (Section 4.5) to equalize the coupling strength to both species. The trajectories of the states in phase space are plotted in Fig. 6.5, where the phase shift corresponds to the area enclosed by the trajectory.

To limit the laser power required for implementing the gate, the wavelength of 401nm has been selected to get comparable coupling strengths on both $^{40}Ca^{+}$and $^{88}Sr^{+}$, as the difference in coupling strength leads to an excursion of the $|gg\rangle$ state, acquiring a phase that counteracts the gate action as can be seen in the area enclosed by the trajectory of $|gg\rangle$ in Fig. 6.5.

The gate is set up by first individually calibrating the local rotations to perform the appropriate π and $\pi/2$ pulses, respectively. The trap frequency can be measured using sideband spectroscopy with the quadrupole lasers. The frequency of the Raman laser is then set according to the measured trap frequency and the targeted gate length. By varying the pulse duration and observing the evolution of the unwanted odd states $|e,g\rangle$, $|g,e\rangle$, the detuning can be adjusted to match the targeted gate duration. The time evolution of the states displayed in Fig. 6.6 shows an asymmetry between the $|e,g\rangle$ and $|g,e\rangle$ states due to the different coupling strength to the $^{40}Ca^{+}$and the $^{88}Sr^{+}$ion, however the population of these states goes to zero for the targeted gate length. The phase acquired by the target states to get the correct

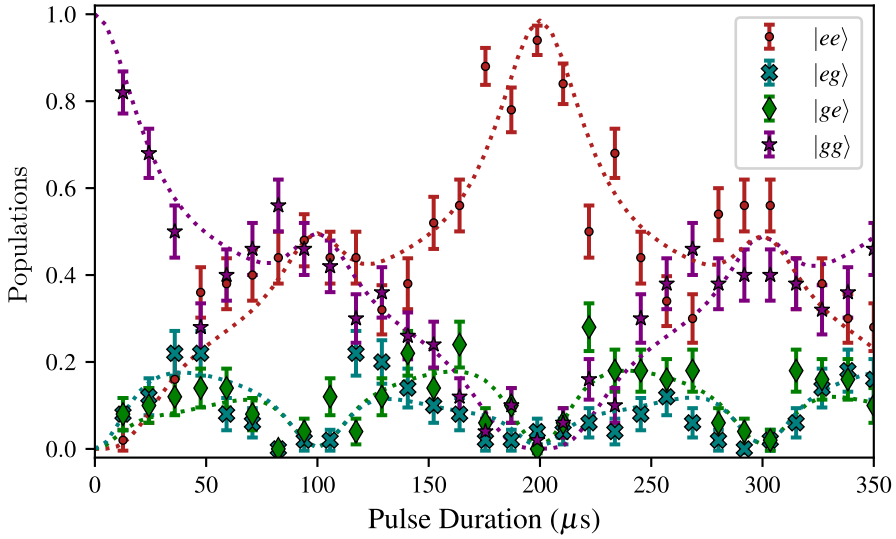

Figure 6.6: POPULATIONS FOR THE MIXED CALCIUM-STRONTIUM ENTANGLING GATE. The evolution is shown as a function of the duration of the interaction. The first state label describes the calcium state and the second refers to the state of the strontium ion. The asymmetry of the $|eg\rangle$, $|ge\rangle$ states when the loop is not closed stems from the different coupling strength to the two species.

gate is calibrated by adjusting the amplitude of the gate pulses, such that the populations in the states $|e,e\rangle$, $|g,g\rangle$ in Fig. 6.6 are balanced at the targeted gate length.

To separate the contributions of state preparation and measurement (SPAM) errors from the gate errors we apply the gate multiple times. Only odd numbers of gates were used, as these gate sequences produce Bell states. For the Bell states, the state fidelity is given by

$$F(\rho, |\psi\rangle\langle\psi|_{\text{Bell}}) = \left((\mathbb{1}\mathbb{1} + \sigma_z\sigma_z)/2 + (\sigma_x\sigma_x + \sigma_y\sigma_y)/2\right)/2, \tag{6.1}$$

where we identify the first two terms as a population component and the last two as a parity component [32, 137]. Even numbers of applications ideally produce either the $|ee\rangle$ or the $|gg\rangle$ state, which does not have a parity component. This allows us to measure the decay of the state fidelity [32] as a function of the number of gates applied. The result is shown in Fig. 6.7, where we extract a fidelity of $0.990(2)$ per gate from the fit.

In contrast applying the same gate scheme on a single species $^{40}Ca^{+}$-$^{40}Ca^{+}$ion crystal we can achieve a fidelity of $0.995(1)$, where we attribute the difference in fidelity primarily to the performance of the 674 nm laser driving the quadrupole transition of $^{88}Sr^{+}$affecting the local gates.

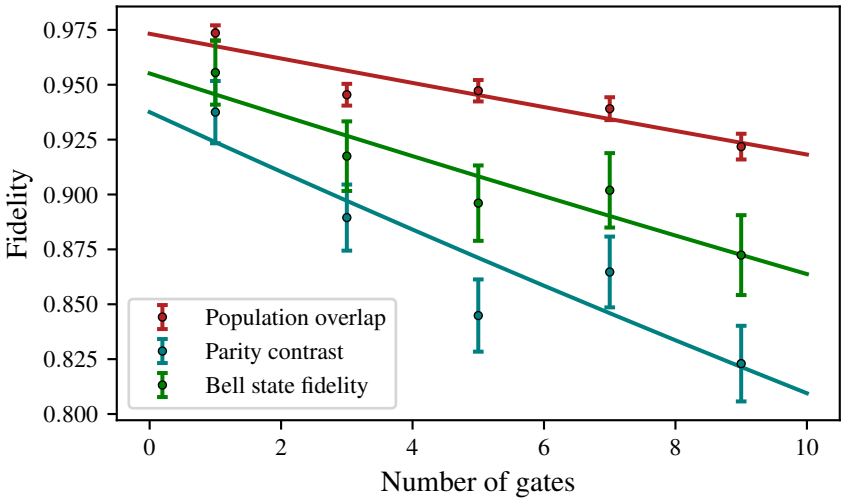

Figure 6.7: FIDELITY FOR MULTIPLE APPLICATIONS OF THE MIXED SPECIES GATE. The population overlap correspond to the first two terms in Eq. (6.1) while the parity contrast corresponds to the latter two. The average between the population overlap and the parity contrast gives the fidelity of the produced Bells states.

6.2 NATIVE QUDIT GATES

The work presented in this section has been published in:

P. Hrmo, B. Wilhelm, L. Gerster, M. van Mourik, M. Huber, R. Blatt, P. Schindler, T. Monz, and M. Ringbauer
"Native qudit entanglement in a trapped ion quantum processor"
Nature Communications 14, 2242 (2023)[1]

In the following section we describe how the light-shift gate can be generalized to qudit systems and how it can be utilized to generate genuine qudit entanglement. Here a single state of the $S_{1/2}$ manifold is used together with multiple states in the $D_{5/2}$ manifold to encode the qudit.

An advantageous feature of the demonstrated gate is the independence of the gate mechanism to the dimension of the qudit, which keeps the experimental calibration overhead constant with increasing qudit dimension. The gate mechanism is based on spin-dependent light-shifts as detailed in Section 3.5.5. The interaction between two ions can be generalized to qudits where it takes the form described in Eq. (3.72). To turn this interaction into a logical gate it is symmetrized by local cyclic permutation gates of the form

$$X_d = \sum_{j=0}^{d-1} |j+1 \pmod d\rangle \langle j| \qquad \text{(3.74 revisited)}$$

1 The author of the present thesis measured and analyzed the data.

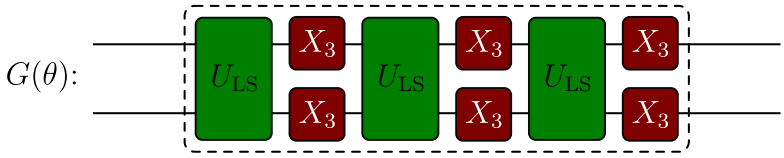

Figure 6.8: PULSE SEQUENCE FOR IMPLEMENTING THE QUTRIT GATE. The entangling light-shift interaction U_{LS} is interleaved with the permutation pulses X_3.

generalizing a spin-echo. These can be implemented by a succession of $d-1$ π-pulses between the 0th and each successive level $j>0$, and can be written as

$$X_d = \prod_{j=1}^{d-1} R^{0,j}(\pi, 0), \tag{6.2}$$

where $R^{0,j}(\theta,\varphi)$ is a rotation between levels 0 and j with angle θ and phase φ.

By applying these permutations each logical state spends the same amount of time in each physical state during the entire gate operation.

A series of d Raman interaction pulses, each forming a closed loop in phase space, and d local cyclic permutations is used to implement the gate operator in dimension d.

The gate sequence is illustrated for the qutrit case ($d=3$) in Fig. 6.8, consisting of entangling light-shift interactions U_{LS} and local X_3 cyclic permutations.

Each light-shift interaction U_{LS} Eq. (3.71) imprints a phase $\widetilde{\Phi}_{ij}$ depending on the electronic state,

$$\widetilde{\Phi}_{ij} = \begin{cases} \Phi_{00} & \text{if } i=j=0 \\ \Phi_{\mathrm{odd}} & \text{if } i=0 \text{ or } j=0 \\ \approx 0 & \text{if } i>0, j>0 \end{cases}, \tag{6.3}$$

the time evolution of which is illustrated in Fig. 6.9. We recall from Section 3.5.5 that due to the symmetrization after the entire sequence we are left with a relative phase between the symmetric $|jj\rangle$ and the non-symmetric $|jk\rangle, j\neq k$ states given by

$$G(\theta) = \begin{cases} |jj\rangle \to |jj\rangle & \\ |jk\rangle \to \exp(i\theta)\,|jk\rangle & \text{if } j\neq k \end{cases}. \tag{3.75 revisited}$$

To investigate the action of the gate we require an appropriate initial state. Analogous to the qubit case we want to prepare an equal superposition as the initial state:

$$|\psi\rangle_{\mathrm{init}} = \frac{1}{d}\left(\sum_{j=1}^{d-1}|j\rangle\right)\otimes\left(\sum_{k=1}^{d-1}|k\rangle\right). \tag{6.4}$$

The equal superposition is chosen since the gate operator changes only the phases, and not the populations, and the equal superposition already has the populations expected of a d-partite fully entangled state.

To accomplish this, we first prepare the ions in the electronic $|00\rangle$ state and motional ground state using sideband cooling and optical pumping. The superposition is then prepared by applying the following operator

$$P = \prod_{j=1}^{d-1} R^{0,j}(\vartheta_j, 0), \tag{6.5}$$

using rotations $R^{0,j}$ between the levels 0 and j, where the angles ϑ_j are chosen as $\vartheta_j = 2\arcsin\left(1/\sqrt{j+1}\right)$. Here each pulse transfers $1/d$-th of the population to the respective sublevel, generating the state in Eq. (6.4).

This can be reversed by the conjugate sequence $P^\dagger$ which applies the pulses in reversed order. That sequence is used after the gate has been applied to create the target states which we further investigate.

6.2.1 *Performance of the gate*

To analyse the gate we can directly estimate the state fidelity and the amount of entanglement of the generated states after applying the gate sequence from the relative amplitudes of the components $|ii\rangle$, as well as their pairwise coherences. Experimentally, the population of the $|00\rangle$ state can be measured by driving the $S_{1/2} \leftrightarrow P_{1/2}$ transition with a 397 nm laser and collecting the fluorescence photons on a photo-multiplier tube. Using additional π-pulses $T_0^j = R^{0,j}(\pi, 0)$, the same procedure gives access to all components $|jj\rangle$ by swapping the population with the $|00\rangle$ state, allowing them to be measured. Using Bayesian parameter estimation we can extract the combined population fidelity $\sum_{j=0}^{D} P(|jj\rangle)$ from the separate measurements, as well as the populations of the individual states $P(|jj\rangle)$ and confidence intervals for these estimates [146]. The Bayesian technique delivers estimates within the uncertainty of the naive technique of fitting the components individually, but importantly delivers much tighter estimates for the error bars, and constrains the total summed population over all states to the physical maximum of 1.

The coherence terms between the states $|00\rangle$ and $|jj\rangle$ are estimated by applying a $\pi/2$-pulse $A_{0,\phi}^j = R^{0,j}(\pi/2, \phi)$ with variable phase ϕ to both ions before performing the fluorescence readout. Depending on the phase ϕ this pulse will transfer populations in the $|00\rangle$, $|jj\rangle$ states to either the $|0j\rangle$, $|j0\rangle$ states or leave them in the $|00\rangle$, $|jj\rangle$ states, causing sinusoidal oscillations as function of ϕ. Applying T_0^k before $A_{0,\phi}^j$ allows us to measure the coherence between the states $|kk\rangle$ and $|jj\rangle$. We then extract the coherence between the two terms from the parity

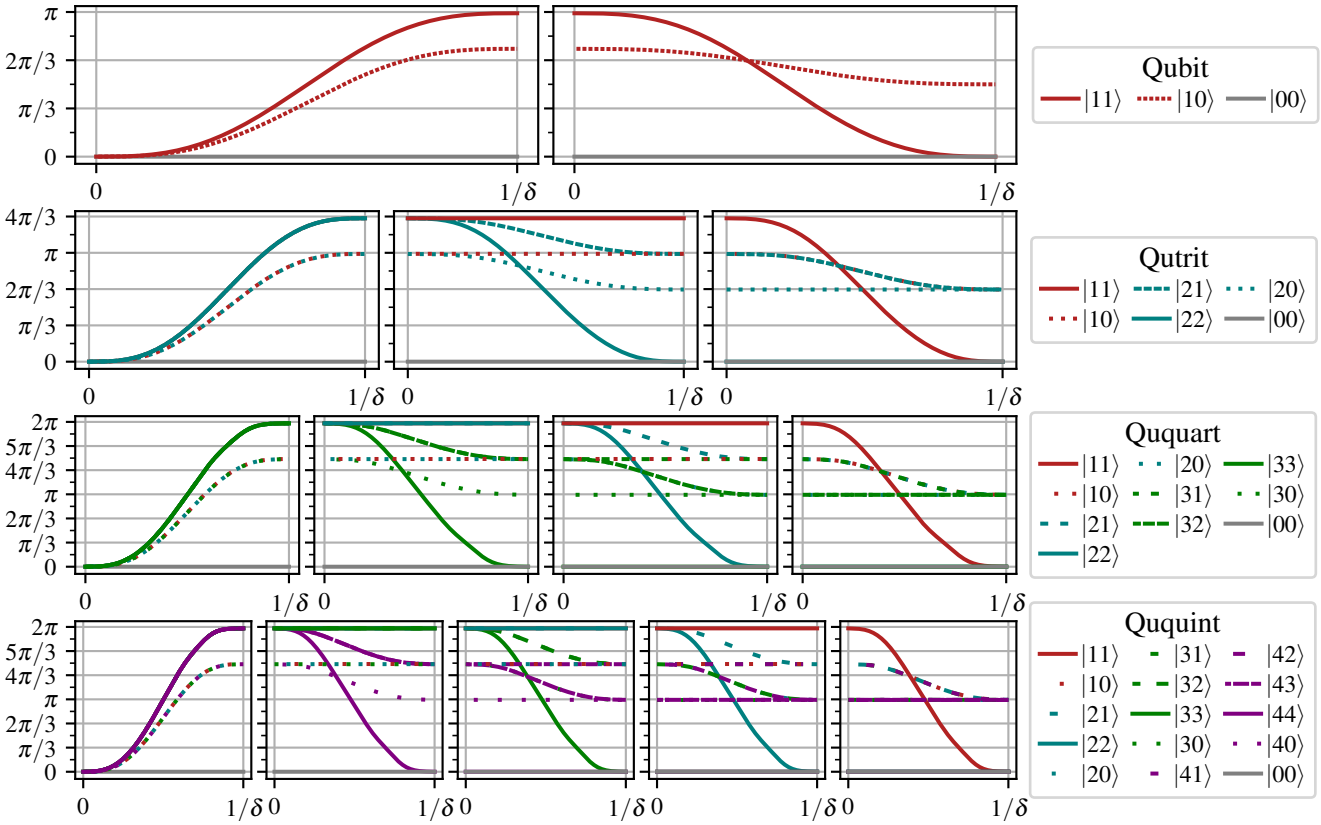

Figure 6.9: PHASE EVOLUTION OF THE TWO-QUDIT STATE FOR DIMENSIONS $d = 2, 3, 4, 5$. The phases of the components are shown relative to the $|00\rangle$ ground state during the application of the d LS gate pulses. Each plot shows the evolution during a closed loop of the motional mode. Notable is the difference of the phase of the symmetric states which returns to zero after the full sequence, while phase shifts are imparted on the asymetric states. The interaction is symmetric with respect to the ions, the trajectory of the $|jk\rangle$ states are equivalent to the $|kj\rangle$ states.

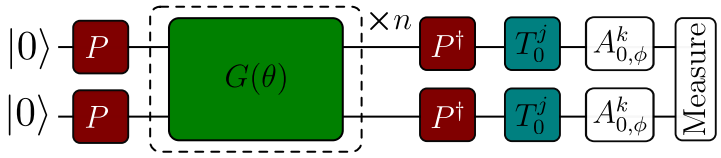

Figure 6.10: Pulse Sequence for analyzing the Qudit gate fidelity. The gate operator $G(\theta)$ is applied n times. The pulses T_0^j select state j for being detected, while the pulses A_0^k are only used for coherence measurements, probing the pairwise coherence between states j and k.

oscillations by Bayesian inference (see Section 5.2), which accounts for measurement statistics and guarantees that the extracted amplitudes of the oscillations stay physically possible.

The observed fidelity is affected by state preparation and measurement (SPAM) errors, which includes the inital pulses P, their inverse $P^\dagger$, the transfer pulse T_0^j and analysis pulse $A_{0,\phi}^j$. In order to separate the errors due to SPAM from errors due to the gate $G(\theta)$ itself for each dimension d, we insert up to n applications[2] of $G(\theta)$ between the preparation operators P and $P^\dagger$. The pulse sequence is shown in Fig. 6.10. We then compute the state fidelity for each n that results in an entangled state and fit an exponential decay to estimate the fidelity per gate. Such repeated gate applications are sensitive to any source of non-Markovian noise present in our system, leading to deviations from a purely exponential decay expected if all noise exhibited Markovian behaviour. The extracted fidelities should thus be interpreted as an estimate for the SPAM corrected average gate performance over a sequence of length n.

We apply this procedure for all the investigated qudit dimensions $d = 2, 3, 4, 5$ and obtain fidelities of 99.4(1)%, 99.0(1)%, 97.5(2)%, 95.0(3)% respectively. While the intrinsic limits on gate fidelity due to finite state lifetime and Raman beam scattering depend only weakly on d (see Appendix B), the measured gate performance degrades quadratically with dimension as seen in Fig. 6.11. This can be understood if the total gate error is dominated by the errors of the local pulses, since their number increases quadratically with qudit dimension, whereas the number of entangling pulses increases linearly.

Indeed this is confirmed by a numeric error model that computes the expected decay data using all independently measured error sources as inputs (see Appendix B), reproducing the observed data with very good agreement (blue bars in Fig. 6.11). This model suggests in particular that, for $d = 2$ the gate fidelity is limited by the motional coherence time of the ion, but for $d = 4, 5$ the dominant error source becomes slow frequency noise that causes dephasing of the local operations. From this we can conclude that the gate fidelity in higher

2 For the different qudit dimensions: $n_{d=2} = 11$, $n_{d=3} = 14$, $n_{d=4} = 9$ and $n_{d=5} = 9$

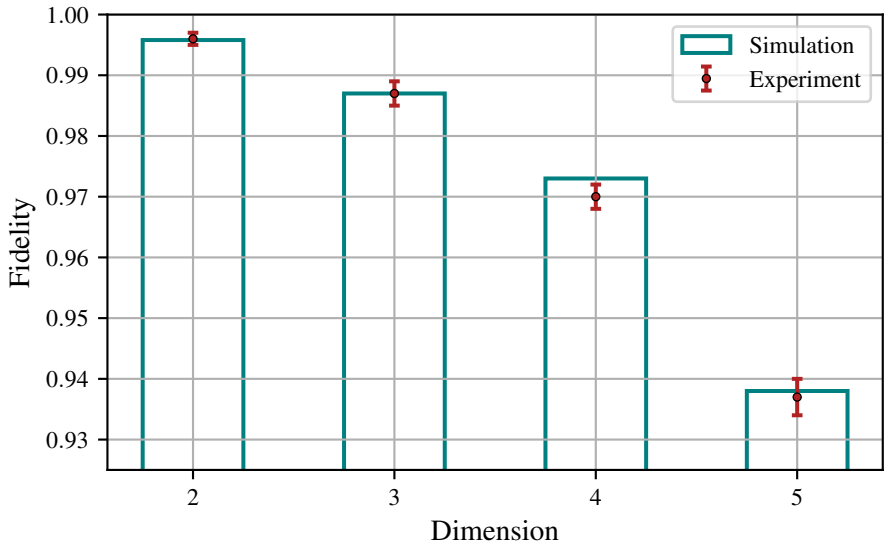

Figure 6.11: FIDELITY OF THE QUDIT GATE. The average gate fidelities, shown in red, are extracted from fits to the fidelity decay when applying multiple gates between encoding and decoding pulses. The error bars correspond to 1 standard deviation in the fit parameters. The simulated fidelities from a detailed noise model are shown in blue

dimensions can be significantly improved if technical noise sources such as magnetic field noise contributing to the aforementioned local operation dephasing or Rabi frequency fluctuations can be suppressed.

6.2.2 *Qudit entanglement of the resulting state*

Another point of interest are the entanglement properties of the state prepared by the application of a single gate. We can quantify that entanglement by measures such as Concurrence and the Schmidt number, comparing the properties of the experimentally produced states to the expected outcomes for a perfect gate.

We are interested in states of the form $|\psi\rangle = \sqrt{1/d}\sum_{j=0}^{d}|jj\rangle$ as a generalization of Bell states. For $d \leq 4$ we can generate these states by applying the gate to the initial state (Eq. (6.4)), however for $d = 5$ we cannot produce a state of this form with a single application of the gate, instead we expect as the target state $|\psi_T\rangle = (3|00\rangle + 2\sum_{j=1}^{4}|jj\rangle)/5$ with a single gate operation. The difference between the target state for $d = 5$ and $d \leq 4$ can be explained by the choice of initial state and the structure of the entangling interaction. For a maximally entangled state the partial trace over one of the qudits must be diagonal, with entries $\mathrm{Tr}_B(|\psi_T\rangle\langle\psi_T|)_{jj} = 1/d$. The equal superposition matches this distributions of populations, but for the relative phases we need to ensure all the off-diagonal elements of the reduced density matrix are set to zero. These are given by $\mathrm{Tr}_B(|\psi_T\rangle\langle\psi_T|)_{ij} = 1/d\sum_k \langle ik|\rho|jk\rangle$,

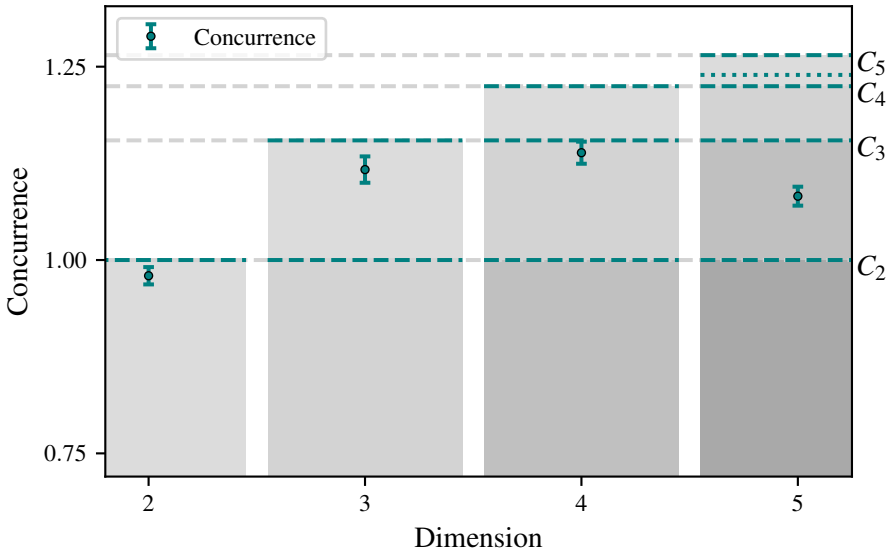

Figure 6.12: CONCURRENCE VS DIMENSION OF THE QUDIT GATE. The blue points display the measured concurrence, with the dashed lines displaying the maximal achievable values for each dimension, the dotted line shows the maximum for the target state.

however the entangling interaction only affects the symmetric states, thus only the terms involving $|jj\rangle, |ii\rangle$ can be controlled. Only up to $d = 4$ it is possible to choose the phases so the sum becomes zero for all off-diagonals, explaining the different structure of the state for $d = 5$.

The first entanglement quantifier we want to study is the concurrence. It is a continuous quantifier of entanglement that can be defined as the convex roof extension [147] of the square-root of the linear entropy.

$$C := \inf_{\mathcal{D}[\rho]} \sum_i p_i \sqrt{2(1 - \mathrm{Tr}[\mathrm{Tr}_B(|\psi_i^{AB}\rangle\langle\psi_i^{AB}|)^2]}\,, \tag{6.6}$$

where $\mathcal{D}[\rho]$ is the space of all possible decompositions into tuples of probabilities and pure state vectors, and can be written as $\mathcal{D}[\rho] = \{(p_i, |\psi_i\rangle) : \sum_i p_i |\psi_i\rangle\langle\psi_i| = \rho\}$. While it is NP-hard to determine the concurrence in high-dimensional systems exactly, even if the density matrix is completely known, it can be lower-bounded by easily accessible measurements. In particular, the lower bound from Ref. [148] is given by

$$C \geq \frac{1}{\sqrt{d(d-1)}} \sum_{i \neq j} \langle ii|\rho|jj\rangle - \sqrt{\langle ij|\rho|ij\rangle \langle ji|\rho|ji\rangle}, \tag{6.7}$$

where the individual density matrix elements $\langle ij|\,\rho\,|ij\rangle$ can be estimated from measurements in the computational basis and the remaining off-diagonal elements through pairwise interference measurements as described in Section 6.2.1.

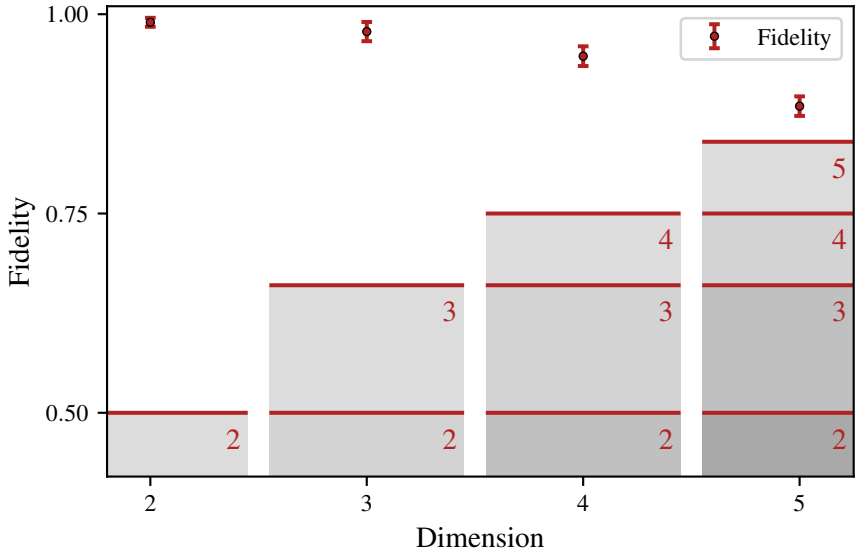

Figure 6.13: FIDELITY VS DIMENSION OF THE QUDIT GATE. The measured state fidelities after a single application of the gate is shown for dimensions $d = 2 - 5$ in red. The shaded bars represent the lower bound of fidelity required to certify maximal Schmidt number entanglement. The fidelity exceeds the threshold for all considered dimensions, certifying d-partite entanglement.

This measure is bounded for a bipartite state[149, 150], where the bound for a d-dimensional state $|\varphi\rangle$ is given by:

$$C(|\varphi\rangle) \leq \sqrt{2(1-\frac{1}{d})} \tag{6.8}$$

For all dimensions $d > 2$ our final state exceeds the $d = 2$ bound of the concurrence (Fig. 6.12), which demonstrates genuine high-dimensional entanglement. However for $d = 4, 5$ the bounds for $d = 3$ are not reached due to experimental imperfections.

Table 6.1: Fidelities and Schmidt numbers for the states produced by a single entangling gate for qudit dimensions $d = 2, 3, 4, 5$. The fidelity threshold corresponds to the minimum fidelity to achieve maximal Schmidt number, while the maximum concurrence gives the value for a pure maximally entangled state of a given dimension.

	fidelity	fidelity threshold	concurrence $\geq$	maximum concurrence	Schmidt number
$d = 2$	0.990 ± 0.006	0.5	0.99 ± 0.03	1	2
$d = 3$	0.978 ± 0.012	0.66	1.14 ± 0.03	1.154	3
$d = 4$	0.947 ± 0.012	0.75	1.16 ± 0.03	1.224	4
$d = 5$	0.885 ± 0.012	0.84	1.08 ± 0.02	1.264	5

Another figure of merit we consider here to evaluate the entangling properties of the gate is the Schmidt number, also referred to as dimensionality of entanglement [151]. It is a discrete measure of how many distinct product states are required to describe the state (Eq. (2.6)). The metric is indicative of the gates usefulness for quantum computation as producing states with a large Schmidt number is a necessary ingredient for achieving a quantum speedup [152], suggesting that it plays a crucial role in the computational complexity of a quantum system [153].

The Schmidt number generalizes to mixed states from the version for pure states (Eq. (2.6)) by minimizing over all possible decompositions $\mathcal{D}(\rho)$.

$$r(\rho) := \inf_{\mathcal{D}(\rho)} \max_{|\psi_i\rangle \in \mathcal{D}(\rho)} \operatorname{rank}(\mathrm{Tr}_B |\psi_i\rangle\langle\psi_i|)\,. \tag{6.9}$$

Computing the Schmidt number is a challenging problem that is at least as hard as deciding whether a given density matrix is separable (NP-hard), however there are easily computable lower bounds. In particular, the fidelity overlap of an experimental state ρ_{exp}, with an entangled target state of the form

$$|\psi_T\rangle = \sum_{i=0}^{d-1} \lambda_i |ii\rangle, \tag{6.10}$$

has an upper bound depending on Schmidt rank r of the state ρ_{exp}. This bound is given by $F(\rho_{exp}, |\psi_T\rangle\langle\psi_T|) \leq \sum_{i=0}^{r-1} \lambda_i^2$, where the coefficients λ_i are in decreasing order. As target state we designate the maximally entangled state in $d = 2, 3, 4$, while for $d = 5$ the expected state $|\psi_T\rangle = (3|00\rangle + 2\sum_{j=1}^{4} |jj\rangle)/5$ was chosen. We get resulting fidelities of $99.0(0.6)\%, 97.8(1.2)\%, 94.7(1.2)\%, 88.5(1.2)\%$, which each exceed the fidelity thresholds for Schmidt numbers $r = d - 1$ using the target states (see Fig. 6.13 and Table 6.1). The case for $d = 5$ is the closest to its corresponding threshold, but assuming a Gaussian distribution of the uncertainty the state fidelity is $\sigma = 3.7$ away above the threshold. Thus the Schmidt number must be indeed maximal in all experimentally implemented dimensions, confirming genuine d-dimensional entanglement for these states.

In conclusion both metrics considered here, the concurrence and the Schmidt number, demonstrate genuine high-dimensional entanglement for $d > 2$. While the concurrence growth slows asymptotically with dimension and thus the bounds are not exceeded for $d > 3$, the Schmidt rank is maximal, which confirms genuine qudit entanglement.

7

CONCLUSION & OUTLOOK

The goal of this thesis was to investigate the scalability of ion trap technology for the purpose of building quantum computers.

To this purpose, an existing setup for dual species operation based on $^{40}Ca^{+}$and $^{88}Sr^{+}$with a segmented surface trap was modified to accept traps with higher electrode counts and integrate high-NA collection optics as described in Chapter 4. We characterized the trap, finding an axial heating rate of $27(2)\,s^{-1}$ at a trap frequency of 1.08 MHz and can achieve of a coherence time of $T_2 = 19.2(13)$ms in $^{40}Ca^{+}$. The detection optics allows in a 50µs window for sub-10^{-4} detection error for a single $^{40}Ca^{+}$ion.

During the course of this thesis, an algorithm using Bayesian parameter estimation to calibrate all the necessary control parameters of the entangling two-qubit Mølmer-Sørensen gate was developed and implemented, which is described in Chapter 5 in detail. We tested two different strategies for choosing the gate sequences used in the algorithm, where we demonstrated that a simple heuristic can match the performance of the more complex and computationally intensive method that chooses a gate sequence that minimize the predicted variance of the parameters.

We evaluated the performance of this algorithm with regard to the estimated parameters and found a resulting median residual infidelity of $1.3(1) \times 10^{-3}$ due to parameter miscalibration, requiring 1200 ± 500 experimental shots. This is a significant speedup over manually iterating 1D scans of the individual parameters.

These results demonstrate that this approach is suitable for reliable and consistent calibration of a system, where the performance is limited by the incoherent noise processes present in the system rather than calibration errors.

The Bayesian algorithm will benefit the quantum CCD ion trap architecture, enabling the calibration of entangling gates in multiple interaction zones where it is no longer plausible to perform this manually. The method is also suitable for addressed gates in a linear ion crystal, where 2 ions are individually addressed, the interaction mediated by a shared radial mode of motion.

A possible extension of this approach is to consider N-qubit entangling gates, to which the Mølmer-Sørensen gate scales naturally using the same set of control parameters [137]. The Bayesian algorithm will work as long as the classical simulation remains traceable, and imperfections such as non-uniform Rabi frequencies and magnetic field gradients are either negligible or sufficiently well modeled in the simulation.

The model underlying the calibration only included a depolarizing noise term. To further refine the model deviations from the ideal, unitary gate action due to independently measured noise sources could be included, which may help to improve the capture range of the algorithm.

The Bayesian algorithm is also extensible to other gates, not limited to the trapped-ion platform, with the requirements being a model of the experimental outcomes of the gate action as function of the parameters of interest. The largest limitation here is the number of control parameters that can be considered, as the amount of information stored in the interpolator will grow exponentially.

The scheme can further be extended to perform track the control parameters, where instead of running the full calibration routine with an unbiased prior, the starting prior is chosen depending on the outcome of the last calibration run and then updated with as few measurements as necessary. By reducing the number of shots required, the routine can be run more often for the same allocated calibration overhead, making the system even more robust against parameter drifts.

We demonstrated in Chapter 6 a mixed-species two-qubit entangling gate, using one $^{40}Ca^{+}$and one $^{88}Sr^{+}$ion. We utilized a single laser to realize a light-shift gate on the pair of qubits. Mixed species entanglement is a beneficial resource for in-sequence readout and for integrating quantum computing techniques with ion-photon entanglement generation schemes, that can connect separate trap modules to scale a quantum computer.

We generated native qudit entanglement between two trapped ions up to dimension $d \leq 5$ with the same gate scheme used for the mixed-species gate. We analyzed the entanglement properties of the produced states [151] and find that in all probed dimensions the Schmidt number is maximal, certifying d-partite entanglement. Using a simulation with a numeric model using independently measured noise parameters, we can reproduce the observed data. The numerical model suggests that the performance for higher dimensions is currently primarily limited by amplitude noise affecting the single qudit operations.

The scheme directly couples all states of the qudit, creating entanglement between multiple qudit levels. The gate is scalable to different dimensions, requiring only adjustment of the power of the gate laser by an analytic ratio. This is a major advantage for calibrating the gate

compared to previous schemes using entangling gates that couple to individual transitions[154], which each require their own set of optimized parameters. This is required to compensate for light shifts, as the embedded qubit gates introduce undesirable phase shifts on the levels that are not being targeted.

The scheme can be investigated using different combinations of ground and excited states for encoding qudits, interleaved with local operations to allow for a wider range of possible gate unitaries. Such an expanded set of unitaries would benefit the compilation of qudit circuits by expanding the building blocks available.

During the work with this experimental apparatus described in this thesis several points have been identified that can be improved, some of which will be included in the next generation experimental apparatus that is currently being assembled. Several lessons have been learned during the operation of our cryostat which will be elaborated on in the following: Closed-cycle cryostats with low vibrations [155, 156] are offered commercially, and promise continuous operation with no swapping of storage Dewars while requiring less maintenance compared to running a Helium liquefaction plant.

The assembly and disassembly method for the cryostat proved itself very inflexible, where each step required needs to be performed in a specific order. Crucially, exchanging the trap is last point in this chain of steps, requiring an almost full tear-down of the system to be accessed. Being able to access the trap instead without dismantling a significant part of the cryostat will decrease wear on the mechanical components due to disassembly and minimize the chance of damage to threads, screws and wiring in the process. It also may allow for easier inspection and troubleshooting of the apparatus. Relocating the DC filters directly on the outside of the copper shield limits the pickup of noise between filter and the trap due to reduced trace lengths as well as blocking Johnson noise caused by finite wire resistance. The resistance of the ground path can be further reduced as heat transfer over the wires between filter and trap is no longer a concern, which reduces distortions of waveforms by the filters.

The thick copper enclosure has proved itself as an effective shield against fast noise magnetic field noise. However the copper shield cannot suppress slow noise, and we were unable to remove the slow drifts in magnetic field strength which we attributed to the stability of the current running through the bias coils. Superconducting coils could be used instead, or sets of permanent magnets.

The high NA lens used was chosen for maximizing collection efficiency. While it could also be used to focus light for single ion addressing, it was not designed to accommodate a steerable addressing setup that can drive pair-wise entangling gates [59] due to aberrations. Such an addressing unit offers full connectivity inside a crystal, and

can limit the amount of splitting and merging operations required in an algorithm. This can be especially advantageous in the context of error corrections, where the majority of operations is applied within a logical qubit. By using a fully connected subregister to encode a logical qubit, the splitting and merging operations would only be required for performing entangling gates between different logical qubits.

One necessary ingredient to be investigated for scalable ion traps with many interaction zones is integrating the light delivery into the trap itself. This reduces or even eliminates the need for optical access, and the optics require no alignment, with the geometry fixed by the design of the trap [157, 158]. In the longer term one also wants to integrate the photo-detection electronics directly into the trap [159], removing all needs for external optics.

Such integration does require more complex trap designs than have been used here, with the fabrication technique limited to a single layer. Future traps will require more complex routing using multiple layers to deliver all the required voltages. While there exists a variety of micro-fabrication technologies to produce such structures, preserving low noise and correspondingly low heating rates is crucial for the performance of the trap [65].

Solving these challenges can pave the way for scaling ion-based quantum computers. Combined with improved gate fidelities, algorithmic advances and improvements in quantum error correction codes could drastically increase the size of problems that can be solved on future quantum computers.

A

MANUAL GATE TUNEUP

One of the desiderata of an optimisation routine is having a fast convergence rate to the desired parameter accuracy. In other words we would like to minimize the number of times the experiment has to be queried since each measurement incurs by far the largest operational time overhead. Since we do not claim to have the optimal strategy, we want to confirm the claim that our Bayesian optimisation is fast relative to what might be considered a traditional or manual optimisation.

In practice, each experimentalist might have their own slightly idiosyncratic way of optimising the gate parameters and will also have different amounts of prior knowledge about the parameter values. There is no set prescription that is followed by a majority consensus in the ion trap literature. However, reference [136] provides an algorithmic approach that iteratively performs one dimensional parameter scans to optimize the gate performance. We find this method closely mirrors what we would perform in our lab in the absence of the Bayesian optimisation routine and hence we will use it as a benchmark. In summary, the algorithm can be reduced to the following:

1. Roughly find the sideband detuning for desired gate time
2. Scan the center line detuning at 2x gate time and maximize the population in p_{ee}
3. Scan the sideband detuning at the presumed gate time and balance the populations p_{ee} and p_{gg}, so that $p_{ee} \approx p_{gg}$
4. Scan the gate time and minimize the populations of $p_{eg} + p_{ge}$
5. Repeat steps 3 and 4
6. Final repeat of step 3
7. Repeat step 2
8. Scan the Phase after two gates
9. Repeat steps 7 and 8

To estimate the parameters from the 1D scans we employ standard least square fitting. For the center line scan a Gaussian fit function is

used on the p_{ee} population, the sideband detuning scan the difference $p_{ee} - p_{gg}$ is fitted with a linear slope to balance the populations. For the gate time scan the dip in the unwanted populations $p_{eg} + p_{ge}$ is fitted with an offset Gaussian. Lastly in the phase scan the population difference $p_{ee} - p_{gg}$ is fitted with a fixed-frequency cosine function.

For each scan, both the number of points and the range of the scan are free parameters that can be altered. To find reasonable combinations of scan width and points we numerically simulate scans with only a single mis-set parameter for combinations of ranges and points, and fit the simulated data. We then choose the range with the smallest distance between 13th and 87th percentile of the distribution of fitted parameter values.

To estimate the performance of the entire routine, we simulate 100 executions of the algorithm described previously for different numbers of points per scan (see Tab. A.1), for a gate with ideal values of $t_g = 100\mu s$, $\omega_{cl} = 0kHz$, $\Delta\varphi = 0$. Each data point consists of 50 measurements. Results with extreme parameter values are discarded ($t_g < 0\mu s$, $t_g > 200\mu s$, $|2\pi\omega_{cl}| > 10kHz$, $2\pi\delta > 20kHz$, $2\pi\delta < 0kHz$), which occurs in 21(2)% of times in all cases considered here. For the remainder we determine the fidelity of the gate given the parameter estimates in the same manner the Bayesian parameter estimates were evaluated (see Fig. 5.16), except that the true value set in the simulation can be substituted for the mean. The results for the different settings can be seen in Fig. A.1.

It should be noted that the robustness of this algorithm could be increased by introducing sanity checks to discard poor fits and adaptively choosing if a parameter should be remeasured. However, doing so will increase the number of measurements further.

We find that for all settings considered here the experimental results obtained using the Bayesian algorithm outperform the simulations of iterative parameter scans both in terms of median infidelity achieved and measurements required even in the ideal case of a noise-free system. Possible reasons for this include that the fit functions are only approximations to the true shape and only part of the measurement data is used for the fit. Furthermore corrections are always applied to

Table A.1: Number of points used in the scans for the different cases for a 1D parameter scan tuneup being considered here.

	Case 1	Case 2	Case 3	Case 4
Points t_g	4	8	16	16
Points δ	4	8	8	10
Points ω_{cl}	4	6	8	12
Points $\Delta\varphi$	4	6	8	10
Total Measurements	2000	3500	4800	5900

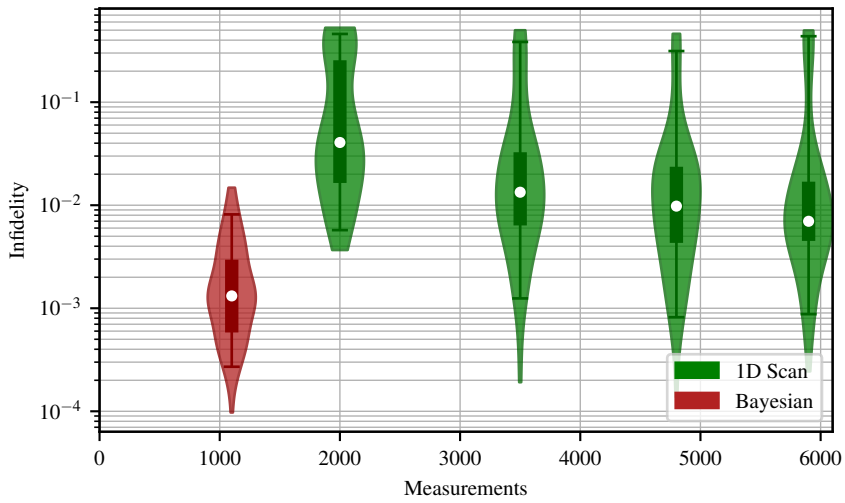

Figure A.1: Simulation of manual tuneups using 1D scans for four different measurement budgets compared to the data obtained using the Bayesian method. The distribution of infidelities is shown as a violine plot (shaded area), with median, quartiles and 5-95 percentiles indicated. For all four settings under consideration, the method has a 21(2)% rate of failure. For all settings the median simulated parameter infidelities are larger than the infidelities obtained from the Bayesian method.

a single variable per scan, leading to correlated effects needing to be corrected by a successive approximation.

In conclusion, the Bayesian algorithm outperforms a 1D manual parameter scan even granting for the most optimistic outcome, and in typical operation it is several times more efficient in the number of required experimental shots.

B

QUDIT GATE NOISE MODEL

To better understand the limitations on the performance of the qudit light-shift gate, we preform a simulation of the experiment to extract the expected gate error given the known sources of noise in the system.

The gate error analysis is based on numerically integrating the Lindblad master equation with collapse operators that describe motional heating and motional dephasing. All other noise sources (with the exception of the local gate laser) are assumed to be slow on the time scale of one experimental shot and thus are treated as static offsets sampled from a normal distribution with standard deviations listed in Table B.1 and averaged over 100 runs of the numerical integration. All input values are measured independently using the ions as probes with appropriate techniques (e.g. sideband thermometry, Ramsey spectroscopy, Rabi spectroscopy, Stark shift measurements etc.). When analysing the 729 laser intensity noise, we discovered further pulse area variations between subsequent π pulses on timescales comparable to those presented during the gate operation. We thus include an additional *fast* noise parameter that samples a new Rabi frequency for each subsequent local pulse during a single gate simulation run. The frequency noise for the local operations contains a contribution from both the finite 729 nm laser linewidth and magnetic field noise. Since each level in our qudit has a different magnetic field sensitivity, we scale the value in Table B.1 by empirically measured coherence times on the different transitions.

Since the action of these slow noise components is non-Markovian we will observe a different error per gate depending on how many gates we apply in succession as errors may build up coherently. To be consistent with the decay fit method that we use to correct for SPAM and extract the fidelity from the experimental data, all simulation fidelities are extracted using an exponential fit to an 11 gate fidelity decay curve.

The intrinsic two-qubit gate fidelity due to scattering and state decay can be calculated analytically following the analysis in [138]. We additionally extend the $D_{5/2}$ state error to be determined not just by the gate length, but also the total time spent applying our generalised spin echo local operations. Extending this analysis to higher dimensions can be significantly simplified since the contributions to the scattering

Error source	Error	Infidelity			
		$d = 2$	$d = 3$	$d = 4$	$d = 5$
Motional heating rate	15 ph/s	1.3×10^{-4}	2.3×10^{-4}	4×10^{-4}	7×10^{-4}
Motional coherence	16 ms	1.2×10^{-3}	2.2×10^{-3}	4×10^{-3}	5×10^{-3}
Motional mode occupation	0.1 ph	3×10^{-4}	2×10^{-4}	3×10^{-4}	1.2×10^{-3}
Gate Rabi frequency	1 %	3×10^{-4}	2×10^{-3}	5×10^{-3}	5×10^{-3}
Slow local Rabi frequency	0.6 %	6×10^{-4}	3×10^{-4}	8×10^{-4}	2×10^{-3}
Fast local Rabi frequency	0.7 %	3×10^{-4}	1×10^{-3}	1.3×10^{-3}	1.6×10^{-3}
Local Rabi imbalance	1 %	7×10^{-4}	5×10^{-4}	1.7×10^{-3}	7×10^{-3}
Gate laser freq. noise	$2\pi \times 200$ rad/s	7×10^{-4}	9×10^{-4}	2×10^{-3}	3×10^{-3}
Local operation freq. noise	$2\pi \times 20$ rad/s	1.5×10^{-6}	2×10^{-3}	6×10^{-3}	2×10^{-2}
Elastic & inelastic scattering		1.6×10^{-4}	2×10^{-4}	3×10^{-4}	3×10^{-4}
$D_{5/2}$ state decay	1 s	8×10^{-5}	2×10^{-4}	5×10^{-4}	9×10^{-4}
Total		4.5×10^{-3}	1×10^{-2}	2.2×10^{-2}	4.7×10^{-2}

Table B.1: Error sources and the corresponding simulated infidelity for the gate in qudit dimension $d = 2, 3, 4, 5$ based on measured noise parameters.

error arising from scattering (both elastic and inelastic) from the $D_{5/2}$ states are negligible. We thus obtain the $d > 2$ errors by scaling the qubit error linearly by the appropriate gate time and laser intensity and correct for the fraction of the initial superposition state present in the S state for $d > 2$ relative to the qubit.

C

ZERO CROSSING TEMPERATURE

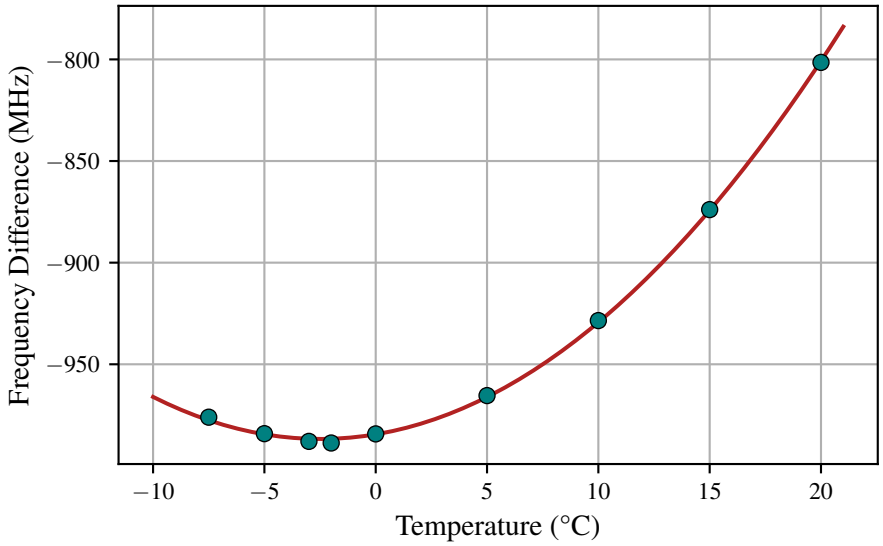

Figure C.1: Temperature dependence of the frequency difference between the TEM_{00} mode of the 674nm high-finesse cavity and the $S_{1/2} \leftrightarrow D_{5/2}$ transition in $^{88}Sr^{+}$. The error bars are smaller than the marker size. The fit indicates a minimum of the frequency at a temperature of -2.49 ± 0.16°C.

The high-finesse cavities used for stabilizing the frequency of the lasers driving the quadrupole transitions are constructed out of two mirrors separated by a spacer made of ultra low expansion glass (ULE). As the resonance frequency depends on the length of the cavity, it is important to keep the length stable. The glass used is especially designed to have a low coefficient of thermal expansion compared to regular glass. Additionally, the spacer has a specific temperature called the zero-crossing temperature (ZCT) where the density is maximal, and the cavity thus shortest. This ZCT is targeted as the operating temperature for the cavity, as at this point the cavity length becomes first-order insensitive to temperature fluctuations, increasing the stability of the system.

The manufacturing process is aimed to produce a ZCT matching room temperature to keep the requirements on the temperature stabilization equipment simple, but it cannot be predicted exactly due

to slight differences created during production of the glass, and the mirrors and their coatings introducing an additional temperature dependence, leading to differences between cavities.

For the 729nm cavity the ZCT was already known from previous measurements[114], but the cavity for the 674nm laser had not been evaluated. The frequency difference between ion and a TEM_{00} cavity mode was recorded as a function of temperature (see Fig. C.1). The measurements are then fitted with a quadratic curve, from which an optimal value of $-2.49 \pm 0.16°C$ was determined.

D

SOFTWARE

For controlling and managing the experiment, we utilize several pieces of custom software. More information about the control software TrICS and the sequencer can be found on the UIBK git repository and the thesis of Daniel Heinrich[100] We also employ small programs to control individual subsystems, which are described for reference in the following:

D.1 CRYOLOGGER

The cryologger software is used to combine all the electronic instruments related to the cryostat system, allowing us to display their status and control them with a single GUI (Appendix D.1). The peripherals are connected via COM-ports to the PC. The monitoring function includes combining the temperature readings, pressure gauge reading, and the data of the floor scale, and sending them to the InfluxDB time-series database. The two heaters can be programmed, and their status is displayed.

The dewar pressure controller regulates the set voltage of the electronic pressure valve on the exhaust of the storage dewar. A slow PID adjusts the pressure depending on the measured temperature of the coldfinger. As the possible output range is limited to $0 - 150$mbar, the integrator value stops increasing/decreasing if it would move the control out of range to prevent integrator windup. When changing the set point an experimentally determined offset value is applied as a feed-forward to increase the responsiveness.

The pressure controller allows scheduling events in advance, where the set point is changed at predetermined times to initiate a cool down.

D.2 BERTHA SERVER

For interfacing the voltage generation hardware with our control software we developed BerthaServer. This python-based software communicates over ethernet with the voltage generation hardware provided by our collaborators from Mainz.

It offers a user interface for setting parameters corresponding to the position and shape of the desired potential, which are the translated to

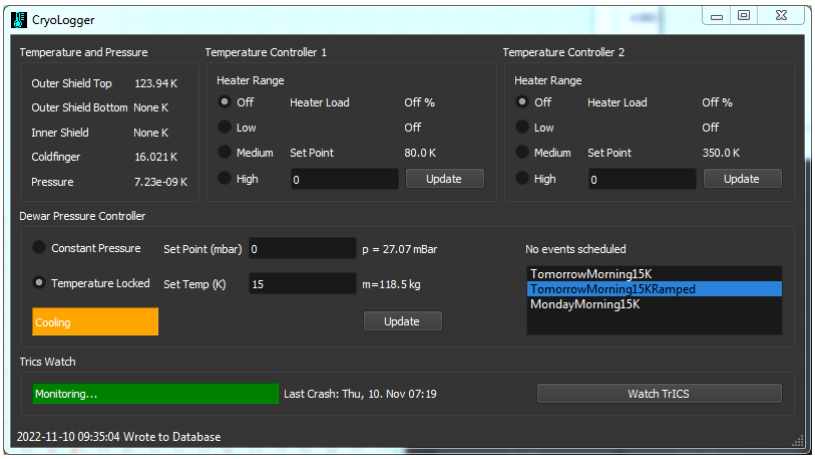

Figure D.1: User Interface of the Cryologger software for controlling the cryostat.

voltage sets to be applied to the individual electrodes. For debugging purposes, voltage offsets can be applied to arbitrary electrodes.

It also offers to define voltage ramps, which can either be precomputed lists of voltage sets, or alternatively the voltage sequences can be defined in code as parametrized functions. These sequences are then parsed to a sequence of voltage sets to be applied, which are then sent to the hardware.

The software can receive remote instructions from trics to update its parameters, making it possible to take measurements as function of these parameters.

D.3 WAVEMETER LOCK

The wavemeter lock consists of 3 parts. The wavemeter itself[1] is linked to a computer on which the manufacturer-provided control software is running. To accept external commands, we run a small server on this computer that accepts incoming commands, and executes them via the exposed functions of the library *wlmData.dll* on that machine (Appendix D.3). It can also connect to an additional 4-channel fiber switch[2] we use to expand the number of ports available, as the switch

1 High Finesse Wavemeter WS-8
2 Leoni Fiber Optical Switch mol 1x4 - SI50/125

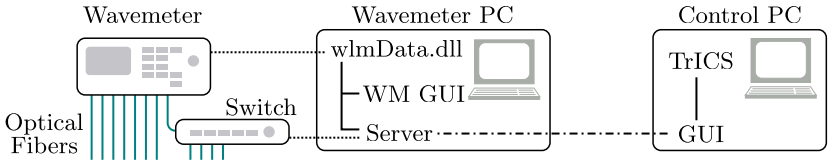

Figure D.2: Schematic of the wavemeter lock.

with the wavemeter has only 8 channels. On the main control computer a GUI is available that can enable measurement channels as well as their associated lock, and the desired target frequency can be set. It can also trigger the calibration of the wavemeter via the stable reference provided by the 729nm laser and switch the channels of the additional fiber switch. With this setup, we can lock 6 lasers (3 per species), monitor the frequencies of the 2 photo-ionization lasers, the Raman laser, and the 674nm laser using the additional switch, with the last port on the wavementer used for the stable reference.

D.4 RASPBUDI

The Raspbudi is a raspberry-pi based controller for the parallel bus system[101] that is used to control DDS frequency and DAC voltage sources. These devices are mounted in a 3HE high subrack that can be installed in a 19" rack.

The raspberry-pi is mounted on a Eurocard format PCB to interface it with the back plane of the 3HE subrack. The GPIO pins are used to drive the bus, controlled by the server running on the raspberry-pi that accepts commands from clients via ethernet. The raspberry-pi is powered directly from the 5V rail of the bus.

As clients it can be either integrated into TrICS by extending it via the UserAPI interface, or a standalone Flask web app can be used. Other clients can easily be implemented, with only a socket connection being required.

E

ATOMIC PROPERTIES

In the table E.1 the relevant transition frequencies for the ion trapping experiments with $^{40}Ca^{+}$and $^{88}Sr^{+}$are shown. Table E.2 shows the state lifetimes and their decay channels. This data has been taken from the NIST Atomic Spectra Database[160].

	Transition	wavelength in air (nm)
$^{40}Ca^{+}$	$4S_{1/2} \leftrightarrow 4P_{1/2}$	396.8469 [161]
	$4S_{1/2} \leftrightarrow 4P_{3/2}$	393.3663 [161]
	$4S_{1/2} \leftrightarrow 3D_{3/2}$	732.389 [161]
	$4S_{1/2} \leftrightarrow 3D_{5/2}$	729.147 [161]*
	$4P_{1/2} \leftrightarrow 3D_{3/2}$	866.214 [161]
	$4P_{3/2} \leftrightarrow 3D_{3/2}$	849.802 [161]
	$4P_{3/2} \leftrightarrow 3D_{5/2}$	854.209 [161]
^{40}Ca	$4s^1S_0 \leftrightarrow 4p^1P_1$	422.6728 [162]
$^{88}Sr^{+}$	$5S_{1/2} \leftrightarrow 5P_{1/2}$	421.55193 [163]
	$5S_{1/2} \leftrightarrow 5P_{3/2}$	407.77094 [163]
	$5S_{1/2} \leftrightarrow 4D_{3/2}$	686.8171 [164]†
	$5S_{1/2} \leftrightarrow 4D_{5/2}$	673.8392 [165]‡†
	$5P_{1/2} \leftrightarrow 4D_{3/2}$	1091.4874 [163, 166]
	$5P_{3/2} \leftrightarrow 4D_{3/2}$	1003.6654 [163, 166]
	$5P_{3/2} \leftrightarrow 4D_{5/2}$	1032.7309 [163, 166]
^{88}Sr	$5s^1S_0 \leftrightarrow 5p^1P_1$	460.7331 [163]

Table E.1: Transition frequencies of the relevant optical transitions in $^{40}Ca^{+}$and $^{88}Sr^{+}$for this work.

* The transition frequency has been measured as 411042129776401.7(1.1)Hz[167]
† Calculated Ritz wavelength from upper and lower state
‡ The transition frequency has been measured as 444779044095484.6(1.5)Hz[168]

	State	Lifetime	Decay channel	
$^{40}Ca^{+}$	$4P_{1/2}$	7.10(2)ns [169]	$4S_{1/2}$	0.93565(7) [170]
			$3D_{3/2}$	0.06435(7) [170]
	$4P_{3/2}$	6.92(2)ns [169]	$4S_{1/2}$	0.9347(3) [171]
			$3D_{3/2}$	0.00661(4) [171]
			$3D_{5/2}$	0.0587(2) [171]
	$3D_{3/2}$	1.20(1)s [172]		
	$3D_{5/2}$	1.168(7)s [172]		
$^{88}Sr^{+}$	$5P_{1/2}$	7.90(10)ns [173]	$5S_{1/2}$	0.9449(5) [174]
			$4D_{3/2}$	0.0551(5) [174]
	$5P_{3/2}$	6.32(10)ns [173]	$5S_{1/2}$	0.9406(2) [175]
			$4D_{3/2}$	0.0063(3) [175]
			$4D_{5/2}$	0.0531(2) [175]
	$4D_{3/2}$	0.435(4)s [176]		
	$4D_{5/2}$	0.3908(16)s [165]		

Table E.2: State Lifetimes and branching ratios for different decay channels for the states utilized in $^{40}Ca^{+}$and $^{88}Sr^{+}$.

PUBLICATIONS

During my work as a PhD student I contributed to the following publications:

[1] M. W. van Mourik, P. Hrmo, L. Gerster, B. Wilhelm, R. Blatt, P. Schindler, and T. Monz, *"RF-induced heating dynamics of non-crystallized trapped ions"*, Physical Review A **105**, 33101 (2022).

[2] F. Martínez-García, L. Gerster, D. Vodola, P. Hrmo, T. Monz, P. Schindler, and M. Müller, *"Analytical and experimental study of center-line miscalibrations in Mølmer-Sørensen gates"*, Physical Review A **105**, 32437 (2022).

[3] L. Gerster, F. Martínez-García, P. Hrmo, M. van Mourik, B. Wilhelm, D. Vodola, M. Müller, R. Blatt, P. Schindler, and T. Monz, *"Experimental Bayesian calibration of trapped ion entangling operations"*, PRX Quantum **3**, 020350 (2022).

[4] M. W. van Mourik, E. A. Martinez, L. Gerster, P. Hrmo, T. Monz, P. Schindler, and R. Blatt, *"Coherent rotations of qubits within a surface ion-trap quantum computer"*, Physical Review A **102**, 022611 (2020).

[5] P. Hrmo, B. Wilhelm, L. Gerster, M. W. van Mourik, M. Huber, R. Blatt, P. Schindler, T. Monz, and M. Ringbauer, *"Native qudit entanglement in a trapped ion quantum processor"*, Nature Communications **14**, arXiv:2206.04104 [quant-ph] type: article, 2242 (2022).

[6] M. W. van Mourik, E. Zapusek, P. Hrmo, L. Gerster, R. Blatt, T. Monz, P. Schindler, and F. Reiter, *"Experimental realization of nonunitary multiqubit operations"*, Physical Review Letters **132**, arXiv:2303.06098 [physics, physics:quant-ph] type: article, 040602 (2024).

BIBLIOGRAPHY

[1] *"Computer"*, in *The Oxford English Dictionary*, Vol. II C, 1st ed. (Oxford University Press, Walton Street, Oxford OX26DP, 1913), p. 750.

[2] W. Thomson, *"Mechanical integration of the linear differential equations of the second order with variable coefficients"*, Proceedings of the Royal Society of London **24**, 269–271 (1876).

[3] P. A. Freiberger and M. R. Swaine, *"Analytical Engine"*, edited by The Editors of Encyclopaedia Britannica, (February 2023) https://www.britannica.com/technology/Analytical-Engine (Accessed: 24 February 2023).

[4] M. Castells, *"The information age: economy, society and culture volume 1: the rise of the network society."* 2nd ed. (Oxford: Wiley Blackwell., 2010).

[5] M. R. Swaine and P. A. Freiberger, *"ENIAC"*, edited by The Editors of Encyclopaedia Britannica, Encyclopedia Britannica, https://www.britannica.com/technology/ENIAC (Accessed: 12 July 2023).

[6] TOP500.org, *"Cray-2/4-256 ecole polytechnique federale de lausanne"*, https://www.top500.org/system/167091/ (Accessed: 10 January 2023).

[7] D. Deutsch and R. Jozsa, *"Rapid solution of problems by quantum computation"*, Proceedings of the Royal Society of London. Series A: Mathematical and Physical Sciences **439**, 553–558 (1992).

[8] L. K. Grover, *"A fast quantum mechanical algorithm for database search"*, in Proceedings of the twenty-eighth annual acm symposium on theory of computing (ACM, 1996), pp. 212–219.

[9] P. W. Shor, *"Algorithms for quantum computation: discrete logarithms and factoring"*, in Proceedings 35th annual symposium on foundations of computer science (December 1994), pp. 124–134.

[10] M. Reiher, N. Wiebe, K. M. Svore, D. Wecker, and M. Troyer, *"Elucidating reaction mechanisms on quantum computers"*, Proceedings of the National Academy of Sciences **114**, 7555–7560 (2017).

[11] I. M. Georgescu, S. Ashhab, and F. Nori, *"Quantum simulation"*, Reviews of Modern Physics **86**, 153–185 (2014).

[12] X.-M. Hu, Y. Guo, B.-H. Liu, Y.-F. Huang, C.-F. Li, and G.-C. Guo, *"Beating the channel capacity limit for superdense coding with entangled ququarts"*, Science Advances **4**, eaat9304 (2018).

[13] Y. Chi et al., *"A programmable qudit-based quantum processor"*, Nature Communications **13**, 1166 (2022).

[14] D. Jaksch, H.-J. Briegel, J. I. Cirac, C. W. Gardiner, and P. Zoller, *"Entanglement of Atoms via Cold Controlled Collisions"*, Physical Review Letters **82**, 1975–1978 (1999).

[15] B. E. Anderson, H. Sosa-Martinez, C. A. Riofrío, I. H. Deutsch, and P. S. Jessen, *"Accurate and robust unitary transformations of a high-dimensional quantum system"*, Phys. Rev. Lett. **114**, 240401 (2015).

[16] D. Loss and D. P. DiVincenzo, *"Quantum computation with quantum dots"*, Physical Review A **57**, 120–126 (1998).

[17] K. Takeda et al., *"A fault-tolerant addressable spin qubit in a natural silicon quantum dot"*, Science Advances **2**, e1600694 (2016).

[18] J. T. Muhonen et al., *"Storing quantum information for 30 seconds in a nanoelectronic device"*, Nature Nanotechnology **9**, 986–991 (2014).

[19] R. Barends et al., *"Digital quantum simulation of fermionic models with a superconducting circuit"*, Nature Communications **6**, 7654 (2015).

[20] F. Arute et al., *"Quantum supremacy using a programmable superconducting processor (supplementary material)"*, Nature **574**, 505–510 (2019).

[21] J. I. Cirac and P. Zoller, *"Quantum computations with cold trapped ions"*, Physical Review Letters **74**, 4091 (1995).

[22] L. Postler et al., *"Demonstration of fault-tolerant universal quantum gate operations"*, Nature **605**, 675–680 (2022).

[23] D. Nigg, M. Müller, E. A. Martinez, P. Schindler, M. Hennrich, T. Monz, M. A. Martin-Delgado, and R. Blatt, *"Quantum computations on a topologically encoded qubit"*, Science **345**, 302–305 (2014).

[24] A. Erhard et al., *"Entangling logical qubits with lattice surgery"*, Nature **589**, 220–224 (2021).

[25] C. Ryan-Anderson et al., *"Realization of Real-Time Fault-Tolerant Quantum Error Correction"*, Physical Review X **11**, 041058 (2021).

[26] R. P. Feynman, *"Simulating physics with computers"*, International Journal of Theoretical Physics 1982 21:6 **21**, 467–488 (1982).

[27] A. M. Turing et al., *"On computable numbers, with an application to the Entscheidungsproblem"*, J. of Math **58**, 5 (1936).

[28] A. Chi-Chih Yao, *"Quantum circuit complexity"*, in Proceedings of the 1993 IEEE 34th Annual Foundations of Computer Science, SFCS '93 (November 1993), pp. 352–361.

[29] D. P. DiVincenzo, *"The physical implementation of quantum computation"*, Fortschritte der Physik **48**, 771–783 (2000).

[30] M. A. Nielsen and I. L. Chuang, *"Quantum computation and quantum information: 10th anniversary edition"* (Cambridge University Press, December 2010).

[31] R. Horodecki, P. Horodecki, M. Horodecki, and K. Horodecki, *"Quantum entanglement"*, Reviews of Modern Physics **81**, 865–942 (2009).

[32] R. Jozsa, *"Fidelity for mixed quantum states"*, Journal of Modern Optics **41**, 2315–2323 (1994).

[33] A. Barenco, C. H. Bennett, R. Cleve, D. P. DiVincenzo, N. Margolus, P. Shor, T. Sleator, J. A. Smolin, and H. Weinfurter, *"Elementary gates for quantum computation"*, Physical Review A **52**, 3457–3467 (1995).

[34] C. M. Dawson and M. A. Nielsen, *"The Solovay-Kitaev algorithm"*, Quantum Information & Computation **6**, arXiv:quant-ph/0505030 type: article, 81–95 (2006).

[35] V. Parasa and M. Perkowski, *"Quantum Phase Estimation Using Multivalued Logic"*, in 2011 41st IEEE International Symposium on Multiple-Valued Logic, ISSN: 2378-2226 (May 2011), pp. 224–229.

[36] P. Gokhale, J. M. Baker, C. Duckering, N. C. Brown, K. R. Brown, and F. T. Chong, *"Asymptotic improvements to quantum circuits via qutrits"*, in Proceedings of the 46th International Symposium on Computer Architecture, ISCA '19 (June 2019), pp. 554–566.

[37] E. T. Campbell, *"Enhanced Fault-Tolerant Quantum Computing in d-Level Systems"*, Physical Review Letters **113**, 230501 (2014).

[38] E. T. Campbell, H. Anwar, and D. E. Browne, *"Magic-State Distillation in All Prime Dimensions Using Quantum Reed-Muller Codes"*, Physical Review X **2**, 041021 (2012).

[39] I. Cohen, P. Richerme, Z.-X. Gong, C. Monroe, and A. Retzker, *"Simulating the Haldane phase in trapped-ion spins using optical fields"*, Physical Review A **92**, 012334 (2015).

[40] A. S. Nikolaeva, E. O. Kiktenko, and A. K. Fedorov, *"Efficient realization of quantum algorithms with qudits"*, preprint, arXiv:2111.04384 [quant-ph] type: article.

[41] X. Gao, P. Appel, N. Friis, M. Ringbauer, and M. Huber, *"On the role of entanglement in qudit-based circuit compression"*, preprint, arXiv:2209.14584 [quant-ph] type: article.

[42] P. Rambow and M. Tian, *"Reduction of circuit depth by mapping qubit-based quantum gates to a qudit basis"*, preprint, arXiv:2109.09902 [quant-ph] type: article.

[43] M. Gell-Mann, *"Symmetries of Baryons and Mesons"*, Physical Review **125**, 1067–1084 (1962).

[44] R. A. Bertlmann and P. Krammer, *"Bloch vectors for qudits"*, Journal of Physics A: Mathematical and Theoretical **41**, 235303 (2008).

[45] G. K. Brennen, S. S. Bullock, and D. P. O'Leary, *"Efficient circuits for exact-universal computation with qudits"*, Quantum Information & Computation **6**, 436–454 (2006).

[46] K. Mato, M. Ringbauer, S. Hillmich, and R. Wille, *"Compilation of Entangling Gates for High-Dimensional Quantum Systems"*, preprint, arXiv:2301.04155 [quant-ph].

[47] D. Gottesman, *"Fault-Tolerant Quantum Computation with Higher-Dimensional Systems"*, in Quantum Computing and Quantum Communications, Vol. 10, edited by C. P. Williams, Lecture Notes in Computer Science 10 (1999), pp. 302–313.

[48] T. Ruster, C. T. Schmiegelow, H. Kaufmann, C. Warschburger, F. Schmidt-Kaler, and U. G. Poschinger, *"A long-lived Zeeman trapped-ion qubit"*, Applied Physics B **122**, 254 (2016).

[49] C. R. Clark et al., *"High-fidelity Bell-state preparation with $^{40}Ca^{+}$ optical qubits"*, Physical Review Letters **127**, 130505 (2021).

[50] R. Srinivas et al., *"High-fidelity laser-free universal control of trapped ion qubits"*, Nature **597**, 209–213 (2021).

[51] L. J. Stephenson, D. P. Nadlinger, B. C. Nichol, S. An, P. Drmota, T. G. Ballance, K. Thirumalai, J. F. Goodwin, D. M. Lucas, and C. J. Ballance, *"High-Rate, High-Fidelity Entanglement of Qubits Across an Elementary Quantum Network"*, Physical Review Letters **124**, 110501 (2020).

[52] V. Krutyanskiy, M. Meraner, J. Schupp, V. Krcmarsky, H. Hainzer, and B. P. Lanyon, *"Light-matter entanglement over 50 km of optical fibre"*, npj Quantum Information **5**, 1–5 (2019).

[53] H. G. Dehmelt, "Radiofrequency spectroscopy of stored ions I: Storage," in *Advances in atomic and molecular physics*, Vol. 3, edited by D. R. Bates and I. Estermann (Academic Press, January 1968), pp. 53–72.

[54] W. Paul and H. Steinwedel, *"Ein neues Massenspektrometer ohne Magnetfeld"*, Zeitschrift fur Naturforschung - Section A Journal of Physical Sciences **8**, 448–450 (1953).

[55] G. Werth, V. N. Gheorghe, and F. G. Major, *"Charged particle traps II"* (Springer, 2009), 286 pp.

[56] D. J. Berkeland, J. D. Miller, J. C. Bergquist, W. M. Itano, and D. J. Wineland, *"Minimization of ion micromotion in a Paul trap"*, Journal of Applied Physics **83**, 5025–5033 (1998).

[57] D. Leibfried, R. Blatt, C. Monroe, and D. Wineland, *"Quantum dynamics of single trapped ions"*, Reviews of Modern Physics **75**, 281 (2003).

[58] P. Schindler, D. Nigg, T. Monz, J. T. Barreiro, E. A. Martinez, S. X. Wang, S. Quint, M. F. Brandl, V. Nebendahl, C. F. Roos, et al., *"A quantum information processor with trapped ions"*, New Journal of Physics **15**, 123012 (2013).

[59] I. Pogorelov et al., *"Compact ion-trap quantum computing demonstrator"*, PRX Quantum **2**, 20343 (2021).

[60] D. Kielpinski, C. Monroe, and D. J. Wineland, *"Architecture for a large-scale ion-trap quantum computer"*, Nature **417**, 709–711 (2002).

[61] J. M. Amini, H. Uys, J. H. Wesenberg, S. Seidelin, J. Britton, J. J. Bollinger, D. Leibfried, C. Ospelkaus, A. P. VanDevender, and D. J. Wineland, *"Toward scalable ion traps for quantum information processing"*, New Journal of Physics **12**, 033031 (2010).

[62] D.-I. " Cho, S. Hong, M. Lee, and T. Kim, *"A review of silicon microfabricated ion traps for quantum information processing"*, Micro and Nano Systems Letters **3**, 2 (2015).

[63] A. Bautista-Salvador, G. Zarantonello, H. Hahn, A. Preciado-Grijalva, J. Morgner, M. Wahnschaffe, and C. Ospelkaus, *"Multilayer ion trap technology for scalable quantum computing and quantum simulation"*, New Journal of Physics **21**, 043011 (2019).

[64] J. H. Wesenberg, *"Electrostatics of surface-electrode ion traps"*, Physical Review A **78**, 063410 (2008).

[65] M. Brownnutt, M. Kumph, P. Rabl, and R. Blatt, *"Ion-trap measurements of electric-field noise near surfaces"*, Reviews of Modern Physics **87**, 1419 (2015).

[66] J. P. Home, "Quantum science and metrology with mixed-species ion chains," in *Advances in atomic, molecular, and optical physics*, Vol. 62, edited by E. Arimondo, P. R. Berman, and C. C. Lin (Academic Press, January 2013) Chap. 4, pp. 231–277.

[67] D. J. Wineland, C. Monroe, W. M. Itano, D. Leibfried, B. E. King, and D. M. Meekhof, *"Experimental issues in coherent quantum-state manipulation of trapped atomic ions."* Journal of Research of the National Institute of Standards and Technology **103**, 259–328 (1998).

[68] D. J. Wineland and W. M. Itano, *"Laser cooling of atoms"*, Physical Review A **20**, 1521–1540 (1979).

[69] C. Cohen-Tannoudji, J. Dupont-Roc, and G. Grynberg, *"Atom-Photon Interactions: Basic Processes and Applications"* (Wiley, New York, NY, 1998), 678 pp.

[70] R. Loudon, *"The quantum theory of light"*, 3rd ed. (OUP Oxford, 2000).

[71] T. W. Hänsch and A. L. Schawlow, *"Cooling of gases by laser radiation"*, Optics Communications **13**, 68–69 (1975).

[72] R. Lechner, C. Maier, C. Hempel, P. Jurcevic, B. P. Lanyon, T. Monz, M. Brownnutt, R. Blatt, and C. F. Roos, *"Electromagnetically-induced-transparency ground-state cooling of long ion strings"*, Physical Review A **93**, 053401 (2016).

[73] M. K. Joshi, A. Fabre, C. Maier, T. Brydges, D. Kiesenhofer, H. Hainzer, R. Blatt, and C. F. Roos, *"Polarization-gradient cooling of 1D and 2D ion Coulomb crystals"*, New Journal of Physics **22**, 103013 (2020).

[74] S. Stenholm, *"The semiclassical theory of laser cooling"*, Reviews of Modern Physics **58**, 699–739 (1986).

[75] M. W. van Mourik, P. Hrmo, L. Gerster, B. Wilhelm, R. Blatt, P. Schindler, and T. Monz, *"RF-induced heating dynamics of non-crystallized trapped ions"*, Physical Review A **105**, 33101 (2022).

[76] J. I. Cirac, L. J. Garay, R. Blatt, A. S. Parkins, and P. Zoller, *"Laser cooling of trapped ions: The influence of micromotion"*, Physical Review A **49**, 421–432 (1994).

[77] I. Marzoli, J. I. Cirac, R. Blatt, and P. Zoller, *"Laser cooling of trapped three-level ions: Designing two-level systems for sideband cooling"*, Physical Review A **49**, 2771–2779 (1994).

[78] D. F. James and J. Jerke, *"Effective Hamiltonian theory and its applications in quantum information"*, Canadian Journal of Physics **85**, 625–632 (2007).

[79] N. F. Ramsey, *"A molecular beam resonance method with separated oscillating fields"*, Physical Review **78**, 695 (1950).

[80] M. Chwalla et al., *"Absolute frequency measurement of the* $^{40}Ca^{+}$ $4s^2S_{1/2} - 3d^2D_{5/2}$ *clock transition"*, Physical Review Letters **102**, 023002 (2009).

[81] M. G. Bussjäger, *"Automated frequency locking via spectroscopy on trapped* $^{40}Ca^{+}$ *ions"*, Master's thesis (University of Innsbruck, 2020).

[82] R. Stricker, *"Gatteroperationen hoher Güte in einem optischen Quantenbit"*, Master's thesis (University of Innsbruck, 2017).

[83] E. L. Hahn, *"Spin Echoes"*, Physical Review **80**, 580–594 (1950).

[84] M. V. Berry, *"Quantal phase factors accompanying adiabatic changes"*, Proceedings of the Royal Society of London. A. Mathematical and Physical Sciences **392**, 45–57 (1984).

[85] A. Sørensen and K. Mølmer, *"Quantum computation with ions in thermal motion"*, Physical Review Letters **82**, 1971–1974 (1999).

[86] A. Sørensen and K. Mølmer, *"Entanglement and quantum computation with ions in thermal motion"*, Physical Review A - Atomic, Molecular, and Optical Physics **62**, 11 (2000).

[87] D. Leibfried et al., *"Experimental demonstration of a robust, high-fidelity geometric two ion-qubit phase gate"*, Nature 2003 422:6930 **422**, 412–415 (2003).

[88] C. F. Roos, *"Ion trap quantum gates with amplitude-modulated laser beams"*, New Journal of Physics **10**, 13002 (2008).

[89] C. J. Ballance, *"High-fidelity quantum logic in* Ca^+*"*, PhD thesis (University of Oxford, 2014).

[90] M. F. Brandl, *"Towards cryogenic scalable quantum computing with trapped ions"*, PhD thesis (University of Innsbruck, 2016).

[91] M. F. Brandl, M. W. V. Mourik, L. Postler, A. Nolf, K. Lakhmanskiy, R. R. Paiva, S. Möller, N. Daniilidis, H. Häffner, V. Kaushal, et al., *"Cryogenic setup for trapped ion quantum computing"*, Review of Scientific Instruments **87**, 113103 (2016).

[92] J. Ekin, *"Experimental Techniques for Low-Temperature Measurements: Cryostat Design, Material Properties and Superconductor Critical-Current Testing"* (Oxford University Press, October 2006), pp. 1–704.

[93] Lakeshore, *"Cryogenic wire"*, https://www.lakeshore.com/products/categories/specification/temperature-products/cryogenic-accessories/cryogenic-wire (Accessed: 1 October 2022).

[94] D. Gandolfi, M. Niedermayr, M. Kumph, M. Brownnutt, and R. Blatt, *"Compact radio-frequency resonator for cryogenic ion traps"*, Review of Scientific Instruments **83**, 084705 (2012).

[95] M. F. Brandl, P. Schindler, T. Monz, and R. Blatt, *"Cryogenic resonator design for trapped ion experiments in Paul traps"*, Applied Physics B **122**, 157 (2016).

[96] F. Teyssandier and D. Prele, *"Commercially available capacitors at cryogenic temperatures"*, in Ninth international workshop on low temperature electronics-wolte9 (June 2010).

[97] M. van Mourik, *"Control of multi-species trapped ions in a scalable quantum computer"*, PhD thesis (University of Innsbruck, 2023).

[98] A. Franzen, *"Component library"*, (2006) http://www.gwoptics.org/component_library/.

[99] P. Schindler, *"Frequency synthesis and pulse shaping for quantum information processing with trapped ions"*, Master's thesis (University of Innsbruck, 2008), pp. 1–105.

[100] D. Heinrich, *"Ultrafast coherent excitation of a $^{40}Ca^{+}$ ion"*, PhD thesis (University of Innsbruck, 2020).

[101] F. Schreck, *"Control system"*, http://www.strontiumbec.com/indexControl.html (Accessed: 12 December 2022).

[102] V. Kaushal, *"A shuttling-based trapped-ion quantum processing node"*, PhD thesis (Johannes Gutenberg-Universität Mainz, 2019).

[103] A. Walther, F. Ziesel, T. Ruster, S. T. Dawkins, K. Ott, M. Hettrich, K. Singer, F. Schmidt-Kaler, and U. Poschinger, *"Controlling fast transport of cold trapped ions"*, Physical Review Letters **109**, 080501 (2012).

[104] F. Schmidt-Kaler, S. Gulde, M. Riebe, T. Deuschle, A. Kreuter, G. Lancaster, C. Becher, J. Eschner, H. Häffner, and R. Blatt, *"The coherence of qubits based on single Ca+ ions"*, Journal of Physics B: Atomic, Molecular and Optical Physics **36**, 623 (2003).

[105] F. M. Gardner, *"Phaselock techniques"* (John Wiley & Sons, 2005).

[106] K. J. Åström and R. M. Murray, *"Feedback systems : an introduction for scientists and engineers"* (Princeton University Press, 2009).

[107] R. W. P. Drever, J. L. Hall, F. V. Kowalski, J. Hough, G. M. Ford, A. J. Munley, and H. Ward, *"Laser phase and frequency stabilization using an optical resonator"*, Applied Physics B **31**, 97–105 (1983).

[108] R. W. Fox, C. W. Oates, and L. W. Hollberg, *"Stabilizing diode lasers to high-finesse cavities"*, Experimental Methods in the Physical Sciences **40**, 1–46 (2003).

[109] R. W. Fox, *"Temperature analysis of low-expansion fabry-perot cavities"*, Optics Express **17**, 15023–15031 (2009).

[110] L. Postler, Á. Rivas, P. Schindler, A. Erhard, R. Stricker, D. Nigg, T. Monz, R. Blatt, and M. Müller, *"Experimental quantification of spatial correlations in quantum dynamics"*, Quantum **2**, 90 (2018).

[111] M. Guggemos, *"Precision spectroscopy with trapped $^{40}Ca^{+}$ and $^{27}Al^{+}$ ions"*, PhD thesis (University of Innsbruck, 2017).

[112] E. A. Whittaker, M. Gehrtz, and G. C. Bjorklund, *"Residual amplitude modulation in laser electro-optic phase modulation"*, JOSA B **2**, 1320–1326 (1985).

[113] E. D. Black, *"An introduction to Pound–Drever–Hall laser frequency stabilization"*, American Journal of Physics **69**, 79–87 (2001).

[114] L. Postler, *"Ein schmalbandiges Halbleiter-Lasersystem für Quanteninformationsverarbeitung und Spektroskopie"*, Master's thesis (University of Innsbruck, 2015).

[115] L.-S. Ma, P. Jungner, J. Ye, and J. L. Hall, *"Delivering the same optical frequency at two places: accurate cancellation of phase noise introduced by an optical fiber or other time-varyingpath"*, Optics Letters **19**, 1777–1779 (1994).

[116] B. Wilhelm, *"Coherent control of a $^{40}Ca^{+}$ ground state qubit"*, Master's thesis (University of Innsbruck, 2021).

[117] L. A. Zhukas, P. Svihra, A. Nomerotski, and B. B. Blinov, *"High-fidelity simultaneous detection of trapped ion qubit register"*, Physical Review A **103**, 10.1103/PhysRevA.103.062614 (2020).

[118] P. Maunz, *"High optical access trap 2.0"*, SAND2016-0796R, Technical Report, 618951 (2016).

[119] Q. A. Turchette et al., *"Heating of trapped ions from the quantum ground state"*, Physical Review A **61**, 063418 (2000).

[120] J. R. Johansson, P. D. Nation, and F. Nori, *"Qutip 2: a python framework for the dynamics of open quantum systems"*, Computer Physics Communications **184**, 1234–1240 (2013).

[121] F. Martínez-García, L. Gerster, D. Vodola, P. Hrmo, T. Monz, P. Schindler, and M. Müller, *"Analytical and experimental study of center-line miscalibrations in Mølmer-Sørensen gates"*, Physical Review A **105**, 32437 (2022).

[122] G. Kirchmair, J. Benhelm, F. Zähringer, R. Gerritsma, C. F. Roos, and R. Blatt, *"Deterministic entanglement of ions in thermal states of motion"*, New Journal of Physics **11**, 23002 (2009).

[123] P. Lee, *"Bayesian statistics: an introduction"*, 4th ed. (Wiley, 2012).

[124] Y.-C. Ho and R. C. K. Lee, *"A bayesian approach to problems in stochastic estimation and control"*, IEEE Transactions on Automatic Control **9**, 382–387 (1964).

[125] D. Q. Mayne, *"A solution of the smoothing problem for linear dynamic systems"*, Automatica **4**, 73–92 (1966).

[126] J. E. Handschin and D. Q. Mayne, *"Monte carlo techniques to estimate the conditional expectation in multi-stage non-linear filtering"*, International Journal of Control **9**, 547–559 (1969).

[127] J. S. Liu and R. Chen, *"Sequential Monte Carlo methods for dynamic systems"*, Journal of the American statistical association **93**, 1032–1044 (1998).

[128] P. A. Walker, *"Quadcubic interpolation: a four-dimensional spline method"*, preprint, arXiv:1904.09869 [math] type: article.

[129] N. J. Gordon, D. J. Salmond, and A. F. M. Smith, *"Novel approach to nonlinear/non-gaussian bayesian state estimation"*, in IEE proceedings F (Radar and Signal Processing), Vol. 140 (IET, 1993), pp. 107–113.

[130] D. B. Rubin, *"Comment : a noniterative sampling/importance resampling alternative to the data augmentation algorithm for creating a few imputations when fractions of missing information are modest : the sir algorithm"*, Journal of the American Statistical Association **82**, 543–546 (1987).

[131] J. Liu and M. West, *"Combined parameter and state estimation in simulation-based filtering"*, in *Sequential monte carlo methods in practice* (Springer, 2001), pp. 197–223.

[132] J. P. Gaebler et al., *"Randomized benchmarking of multiqubit gates"*, Physical Review Letters **108**, 260503 (2012).

[133] J. Emerson, R. Alicki, and K. Życzkowski, *"Scalable noise estimation with random unitary operators"*, Journal of Optics B: Quantum and Semiclassical Optics **7**, S347–S352 (2005).

[134] E. Magesan, J. M. Gambetta, and J. Emerson, *"Scalable and robust randomized benchmarking of quantum processes"*, Physical Review Letters **106**, 8–11 (2011).

[135] A. Erhard, J. J. Wallman, L. Postler, M. Meth, R. Stricker, E. A. Martinez, P. Schindler, T. Monz, J. Emerson, and R. Blatt, *"Characterizing large-scale quantum computers via cycle benchmarking"*, Nature Communications **10**, 5347 (2019).

[136] N. Akerman, N. Navon, S. Kotler, Y. Glickman, and R. Ozeri, *"Universal gate-set for trapped-ion qubits using a narrow linewidth diode laser"*, New Journal of Physics **17**, 113060 (2015).

[137] T. Monz, P. Schindler, J. T. Barreiro, M. Chwalla, D. Nigg, W. A. Coish, M. Harlander, W. Hänsel, M. Hennrich, and R. Blatt, *"14-Qubit Entanglement: Creation and Coherence"*, Physical Review Letters **106**, 130506 (2011).

[138] B. C. Sawyer and K. R. Brown, *"Wavelength-insensitive, multispecies entangling gate for group-2 atomic ions"*, Physical Review A **103**, 022427 (2021).

[139] Y. Wang, Z. Hu, B. C. Sanders, and S. Kais, *"Qudits and high-dimensional quantum computing"*, Front. Phys. **8** (2020).

[140] P. O. Schmidt, T. Rosenband, C. Langer, W. M. Itano, J. C. Bergquist, and D. J. Wineland, *"Spectroscopy Using Quantum Logic"*, Science **309**, 749–752 (2005).

[141] M. D. Barrett et al., *"Sympathetic cooling of ${}^{9}{\mathrm{Be}}^{+}$ and ${}^{24}{\mathrm{Mg}}^{+}$ for quantum logic"*, Physical Review A **68**, 042302 (2003).

[142] J. P. Home, D. Hanneke, J. D. Jost, J. M. Amini, D. Leibfried, and D. J. Wineland, *"Complete methods set for scalable ion trap quantum information processing"*, Science **325**, 1227–1230 (2009).

[143] P. Drmota et al., *"Robust Quantum Memory in a Trapped-Ion Quantum Network Node"*, Physical Review Letters **130**, 090803 (2023).

[144] V. Negnevitsky, M. Marinelli, K. K. Mehta, H.-Y. Lo, C. Flühmann, and J. P. Home, *"Repeated multi-qubit readout and feedback with a mixed-species trapped-ion register"*, Nature **563**, 527–531 (2018).

[145] C. Monroe, R. Raussendorf, A. Ruthven, K. R. Brown, P. Maunz, L.-M. Duan, and J. Kim, *"Large-scale modular quantum-computer architecture with atomic memory and photonic interconnects"*, Physical Review A **89**, 022317 (2014).

[146] B. P. Carlin and T. A. Louis, *"Bayes and Empirical Bayes Methods for Data Analysis, Second Edition"* (Taylor & Francis, December 2010).

[147] A. Uhlmann, *"Roofs and Convexity"*, Entropy **12**, arXiv:1108.3218 [math-ph, physics:quant-ph], 1799–1832 (2010).

[148] M. Huber, M. Perarnau-Llobet, and J. I. D. Vicente, *"Entropy vector formalism and the structure of multidimensional entanglement in multipartite systems"*, Physical Review A **88**, 042328 (2013).

[149] P. Rungta, V. Buzek, C. M. Caves, M. Hillery, and G. J. Milburn, *"Universal state inversion and concurrence in arbitrary dimensions"*, Physical Review A **64**, 042315 (2001).

[150] S. Rai and J. R. Luthra, *"Negativity and Concurrence as complete entanglement measures for two arbitrary qudits"*, preprint, arXiv:quant-ph/0508045 type: article.

[151] N. Friis, G. Vitagliano, M. Malik, and M. Huber, *"Entanglement certification from theory to experiment"*, Nature Reviews Physics **1**, 72–87 (2019).

[152] G. Vidal, *"Efficient Classical Simulation of Slightly Entangled Quantum Computations"*, Physical Review Letters **91**, 147902 (2003).

[153] M. V. d. Nest, *"Universal quantum computation with little entanglement"*, Physical Review Letters **110**, 060504 (2013).

[154] M. Ringbauer, M. Meth, L. Postler, R. Stricker, R. Blatt, P. Schindler, and T. Monz, *"A universal qudit quantum processor with trapped ions"*, Nature Physics **18**, 1053–1057 (2022).

[155] P. Micke, J. Stark, S. A. King, T. Leopold, T. Pfeifer, L. Schmöger, M. Schwarz, L. J. Spieß, P. O. Schmidt, and J. R. C. López-Urrutia, *"Closed-cycle, low-vibration 4 k cryostat for ion traps and other applications"*, Review of Scientific Instruments **90**, 10.1063/1.5088593 (2019).

[156] T. Dubielzig, S. Halama, H. Hahn, G. Zarantonello, M. Niemann, A. Bautista-Salvador, and C. Ospelkaus, *"Ultra-low vibration closed-cycle cryogenic surface-electrode ion trap apparatus"*, Review of Scientific Instruments **92**, 10.1063/5.0024423 (2021).

[157] K. K. Mehta, C. Zhang, M. Malinowski, T.-L. Nguyen, M. Stadler, and J. P. Home, *"Integrated optical multi-ion quantum logic"*, Nature **586**, 533–537 (2020).

[158] R. J. Niffenegger et al., *"Integrated multi-wavelength control of an ion qubit"*, Nature **586**, 538–542 (2020).

[159] S. L. Todaro, V. B. Verma, K. C. McCormick, D. T. C. Allcock, R. P. Mirin, D. J. Wineland, S. W. Nam, A. C. Wilson, D. Leibfried, and D. H. Slichter, *"State Readout of a Trapped Ion Qubit Using a Trap-Integrated Superconducting Photon Detector"*, Physical Review Letters **126**, 010501 (2021).

[160] A. Kramida, Yu. Ralchenko, J. Reader, and and NIST ASD Team, *"Nist atomic spectra database (ver. 5.9)"*, (2021) https://www.nist.gov/pml/atomic-spectra-database.

[161] B. Edlén and P. Risberg, *"The spectrum of singly-ionized calcium, Ca II"*, Ark. Fys. (Stockholm), 553–566 (1956).

[162] G. Risberg, *"The spectrum of atomic calcium, Ca I, and extensions to the analysis of Ca II"*, Ark. Fys. (Stockholm), 231 (1968).

[163] F. J. Sullivan, *"Strontium lines in arc and solar spectra"*, PhD thesis (University of Pittsburgh, 1938).

[164] E. Biémont, J. Lidberg, S. Mannervik, L.-O. Norlin, P. Royen, A. Schmitt, W. Shi, and X. Tordoir, *"Lifetimes of metastable states in Sr II"*, The European Physical Journal D - Atomic, Molecular, Optical and Plasma Physics **11**, 355–365 (2000).

[165] V. Letchumanan, M. A. Wilson, P. Gill, and A. G. Sinclair, *"Lifetime measurement of the metastable state in using a single trapped ion"*, Physical Review A - Atomic, Molecular, and Optical Physics **72**, 012509 (2005).

[166] G. H. Newsom, S. O'Connor, and R. C. M. Learner, *"Re-examination of the spectrum of strontium: autoionization in the spectrum of neutral strontium"*, Journal of Physics B: Atomic and Molecular Physics **6**, 2162–2176 (1973).

[167] Y. Huang, H. Guan, P. Liu, W. Bian, L. Ma, K. Liang, T. Li, and K. Gao, *"Frequency comparison of two $^{40}Ca^{+}$ optical clocks with an uncertainty at the 10^{-17} level"*, Physical Review Letters **116**, 013001 (2016).

[168] H. S. Margolis, G. P. Barwood, G. Huang, H. A. Klein, S. N. Lea, K. Szymaniec, and P. Gill, *"Hertz-level measurement of the optical clock frequency in a single $^{88}Sr^{+}$ ion"*, Science **306**, 1355–1358 (2004).

[169] J. Jin and D. A. Church, *"Precision lifetimes for the* Ca^+ $4p^2P$ *levels: experiment challenges theory at the 1% level"*, Physical Review Letters **70**, 3213 (1993).

[170] M. Ramm, T. Pruttivarasin, M. Kokish, I. Talukdar, and H. Häffner, *"Precision measurement method for branching fractions of excited P 1/2 states applied to* $^{40}Ca^+$*"*, Physical Review Letters **111**, 023004 (2013).

[171] R. Gerritsma, G. Kirchmair, F. Zähringer, J. Benhelm, R. Blatt, and C. F. Roos, *"Precision measurement of the branching fractions of the 4p 2P3/2 decay of Ca II"*, The European Physical Journal D 2008 50:1 **50**, 13–19 (2008).

[172] P. A. Barton, C. J. S. Donald, D. M. Lucas, D. A. Stevens, A. M. Steane, and D. N. Stacey, *"Measurement of the lifetime of the* $3d^2D_{5/2}$ *state in* $^{40}Ca^+$*"*, Physical Review A **62**, 032503 (2000).

[173] E. H. Pinnington, R. W. Berendsî, and M. Lumsden, *"Studies of laser-induced fluorescence in fast beams of* Sr^+ *and* Ba^+ *ions"*, Journal of Physics B: Atomic, Molecular and Optical Physics **28**, 2095 (1995).

[174] J. P. Likforman, V. Tugayé, S. Guibal, and L. Guidoni, *"Precision measurement of the branching fractions of the* $5p^2P_{1/2}$ *state in* $^{88}Sr^+$ *with a single ion in a microfabricated surface trap"*, Physical Review A **93**, 052507 (2016).

[175] H. Zhang, M. Gutierrez, G. H. Low, R. Rines, J. Stuart, T. Wu, and I. Chuang, *"Iterative precision measurement of branching ratios applied to 5P states in* $^{88}Sr^+$*"*, New Journal of Physics **18**, 123021 (2016).

[176] S. Mannervik, J. Lidberg, L. O. Norlin, P. Royen, A. Schmitt, W. Shi, and X. Tordoir, *"Lifetime measurement of the metastable* $4d^2D_{3/2}$ *level in* Sr^+ *by optical pumping of a stored ion beam"*, Physical Review Letters **83**, 698 (1999).

COLOPHON

This document was typeset using the typographical look-and-feel `classicthesis` developed by André Miede. The style was inspired by Robert Bringhurst's seminal book on typography "*The Elements of Typographic Style*". `classicthesis` is available for both LaTeX and LyX:

https://bitbucket.org/amiede/classicthesis/

Happy users of `classicthesis` usually send a real postcard to the author, a collection of postcards received so far is featured here:

http://postcards.miede.de/

Final Version as of July 10, 2024 (version 1.0).